University of Cape Town
Department of Physics

Measurement of neutron fluence at $E_n = 20$ - 100 MeV using a stacked scintillator spectrometer.

Siphiwo Aquinas Makupula

A thesis submitted to the Faculty of Science at the University of Cape Town in fulfilment of the requirements for the degree of Master of Science in Physics

February 2003

I declare that, except where acknowledged, the work contained in this thesis to be my own original work, carried out with the guidance and advice from my supervisor. I also acknowledge the assistance of my supervisor, colleagues and fellow students during the periods when experimental measurements were made, this not being possible to execute except by way of a team.

S. A. Makupula

Signed by candidate

On the 02 day of June 2003

Abstract

The present work demonstrates a new application of a stacked spectrometer which has been developed in the Physics Department of the University of Cape Town. The spectrometer used in the present work consists of two identical segments of NE213 liquid scintillator, of dimensions 13.0 × 13.0 × 7.0 cm^3, stacked behind one-another, and allows response functions to be measured for neutrons of energy up to 100 MeV, which are minimally affected by charged particle escape. Pulse height spectra were measured for quasi-monoenergetic neutrons of energy 20 to 100 MeV, which facilitated the construction of a pulse-height response matrix for this neutron energy range. Measurements of neutron spectral fluence could then be obtained for a variety of beams from the application of unfolding procedures, thereby illustrating a new use of the spectrometer in situations where pulsed neutron beams are not available.

ACKNOWLEDGEMENTS

I would like to express my sincere appreciation and gratitude to the following people and organizations who directly or indirectly contributed to the success of this project:

Dr Andy Buffler, my supervisor and a friend, for his untiring encouragement and support. This work would never been completed without his care and assistance.

Em. Professor Frank D. Brooks who without his knowledge, ideas and creativity this project would not have been started, continued and completed. The verbal communication also contributed enormously to its completion. May God keep you around for another thousand years.

Assoc. Professor Saalih Allie whose expertise in computer programming and education made the team work smoothly during the runs and writing up.

My colleagues, in particular Dr Rudolph Nchodu and Mark Herbert, for the assistance during the experiments and communication during the write-up of this work.

The always welcoming UCT Physics Technical and Administrative Staff. The use of their facilities and resources made me feel at home.

This work would also never have commenced without the concern and agreement of the iThemba LABS' Technical and Administrative staff.

The UCT Bursary Office. It made life look simpler and targets reachable.

The NRF Grantholders' linked scholarships that made the completion of this work possible.

My family and friends, in particular my grandmother, Bangiwe and my daughters, Ota and Sipokazi who created a target for me and, Gqunu and TaWest who made it possible for me to reach my target and my sister Doreen for being there all the time.

All the people that I've met in my life have contributed in one way or another.

Thanx again!

What a team!! ***Να σας έχει καλά όλους ο Θεός!!***

CONTENTS

LIST OF FIGURES

LIST OF TABLES

1

Introduction

The need for measurements of neutron fluence [1] arises in many areas of pure and applied nuclear physics research. Very often knowledge of the energy distribution of the fluence of a neutron beam is required. If the neutron beam is nanosecond-pulsed, then the well-known time-of-flight method may be used to measure the energy spectrum of the beam. However, in stationary fields, alternative methods, such as those based on unfolding analyses, need to be employed.

Since the neutron is not charged, most neutron detectors rely on detecting charged particles recoiling from neutron-induced nuclear interactions in the detector. There have been a number of recent reviews of the state of the art in neutron detectors (see for example [Pe00, Br02]). Organic scintillation detectors are an important class of detectors, where the neutron is detected indirectly via the secondary protons and other charged particles released in interactions with the hydrogen and carbon in the scintillator medium. Ionisation and excitation produced by the charged particle slowing down in the scintillator lead to a scintillation of light which may be converted to an electronic pulse by a photomultiplier.

[1] The flux of a neutron beam can be understood to be the number of neutrons per unit area per unit time, whereas the fluence is the flux integrated over the entire measurement time.

The amplitude, or height, of this pulse is related to the total light in the scintillator, and is referred to as the response of the scintillator. The dependence of scintillator response on the type and energy the particle responsible for the scintillation is an important characteristic of organic scintillators. The collection and sorting of pulses produced by such a scintillator results in a pulse height spectrum, the form of which is highly characteristic of both the incident radiation and the detector used.

1.1 Liquid organic scintillators

For measurements undertaken in mixed neutron/gamma fields, liquid organic scintillators offer both the ability to discriminate between events induced by neutrons and gamma-rays, and a relatively high detection efficiency. The most widely used liquid scintillator consists predominantly of hydrocarbons and is known by its brand name NE213 [NE] [2]. The primary component of NE213 liquid scintillator is xylene ($C_6H_4(CH_3)_2$) to which naphthalene ($C_{12}H_8$) is added to reduce quenching effects and enhance the slow component of the light output.

The non-linear dependence of the response of organic scintillators on particle energy is well understood and has been applied in many works (see for example, [Bi64, Br79]). The semi-empirical model proposed by Birks in 1951 [Bi64], within a few years of the first publication on organic scintillators, provides a good description of the non-linear response of organic scintillators. Birks proposed that the non-linear response is caused by quenching effects in the scintillator, which are governed by the specific energy loss, d*E*/d*x*, of the ionising particle and suggested a model of the form

$$\frac{dL}{dx} = \frac{S\frac{dE}{dx}}{1 + kB\frac{dE}{dx}} \qquad (1.1)$$

[2] NE213 [NE] was a registered trademark of Nuclear Enterprises Technology Inc. (Edinburgh, Scotland) and is no longer available. Bicron [BIC] offers the equivalent product of BC501A which is claimed to have the same chemical, physical and optical properties as NE213. The relative performance of NE213 and BC501A is compared favourably in [Mo94]. More recently, Eljen Technology [ET] is offering EJ301 which is also a generic of NE213. In the present work, the scintillator used will be referred to as NE213.

where dL/dx is the light output per unit length and $B\ dE/dx$ is the quenching probability with B being the so-called Birks parameter. S is a constant and k is the quenching parameter [Br79]. The parameter kB is usually found by fitting the Birks relation to experimental data. The scintillator response depends on the energy, mass and charge of the ionising particle and becomes more non-linear for more heavily ionising particles. Figure 1.1 shows the light output function $L(E)$ in units of MeV_{ee} for electrons (e), protons (p) and α-particles depositing their entire energy in a cylindrically shaped NE213 scintillator of diameter 5.08 cm and length 5.08 cm [Kl02]. Light output in MeV_{ee} may be regarded as the equivalent energy deposited if the particle were an electron. It can be seen, for example, that a 14 MeV alpha particle will produce about the same light output as a 5 MeV proton and a 2 MeV electron. This shows that the heavier particles will produce less light as compared to the lighter particles of the same energy.

The scintillation time decay of NE213 and some other liquid scintillators can be described as the sum of a "fast" exponential component, and a "slow" non-exponential component (see figure 1.2). For these scintillators both the shape and the relative intensities of these two scintillation components depend on the type of charged particle (e, p, d, α, etc.) that caused the scintillation. This effect forms the basis of the pulse shape discrimination technique.

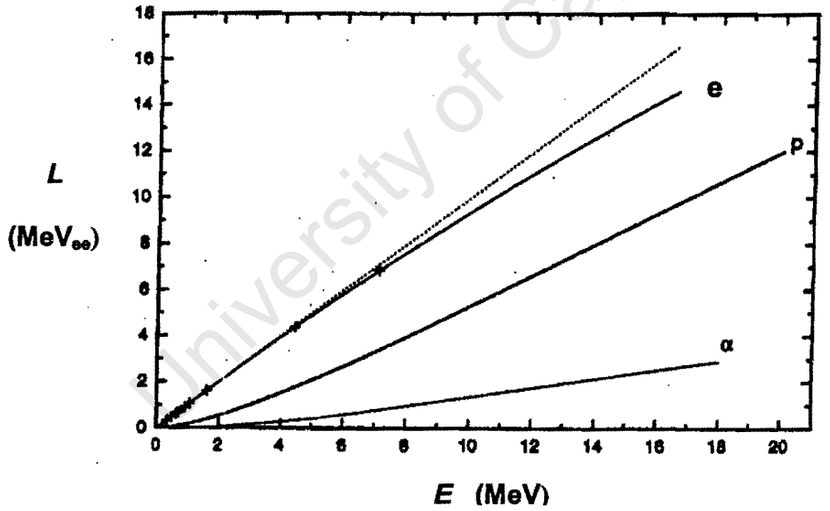

Figure 1.1. Light output functions L(E)in MeV_{ee} (MeV electron equivalent) for electrons (e), protons (p), and α–particles (α) if their entire energy E is deposited in an NE213 scintillator, 5.08 cm in diameter and length [Kl02]. The dotted line indicates a linear response.

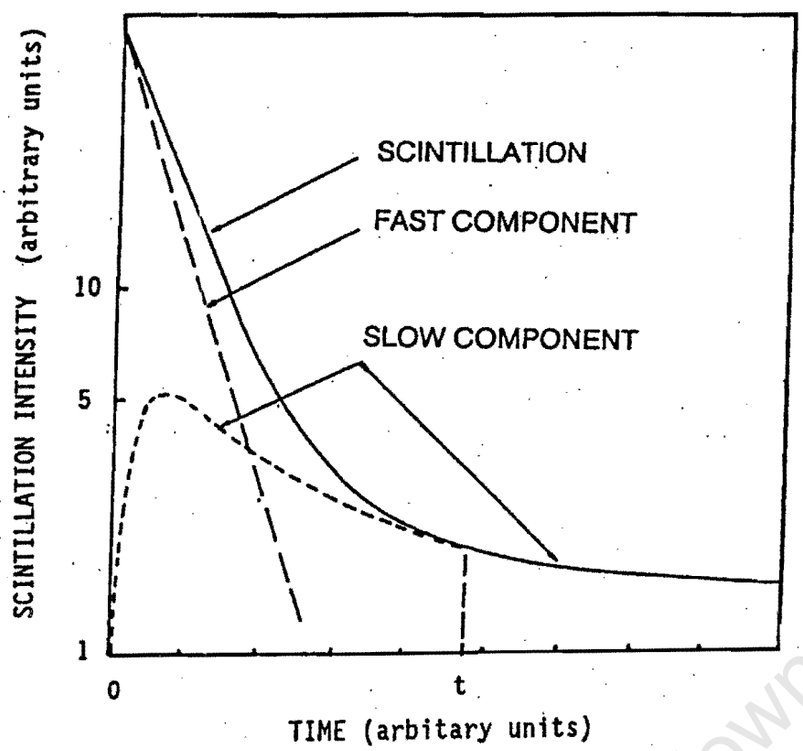

Figure 1.2. Schematic representation of the scintillation decay of an organic scintillator showing the "fast" and "slow" components [Vo68].

Figure 1.3(a) shows measurements by Lynch [Ly75] of the average scintillation decay shapes of NE213 when excited by incident neutrons and gamma rays respectively. The two measurements have been normalized to 10^4 units at the scintillation peaks. Figure 1.3(b) shows the integrals of the measured curves of figure 1.3(a), normalized at t = 500 ns. The "fast" pulse integral, which might be measured from t = 0 to 50 ns, for example, is a smaller fraction of the total integral for neutrons (72%) than for gammas (92%), due to the different shapes of their pulses. A variety of electronic methods have been devised (see for example [Br79]) in order to implement pulse shape discrimination in liquid scintillators.

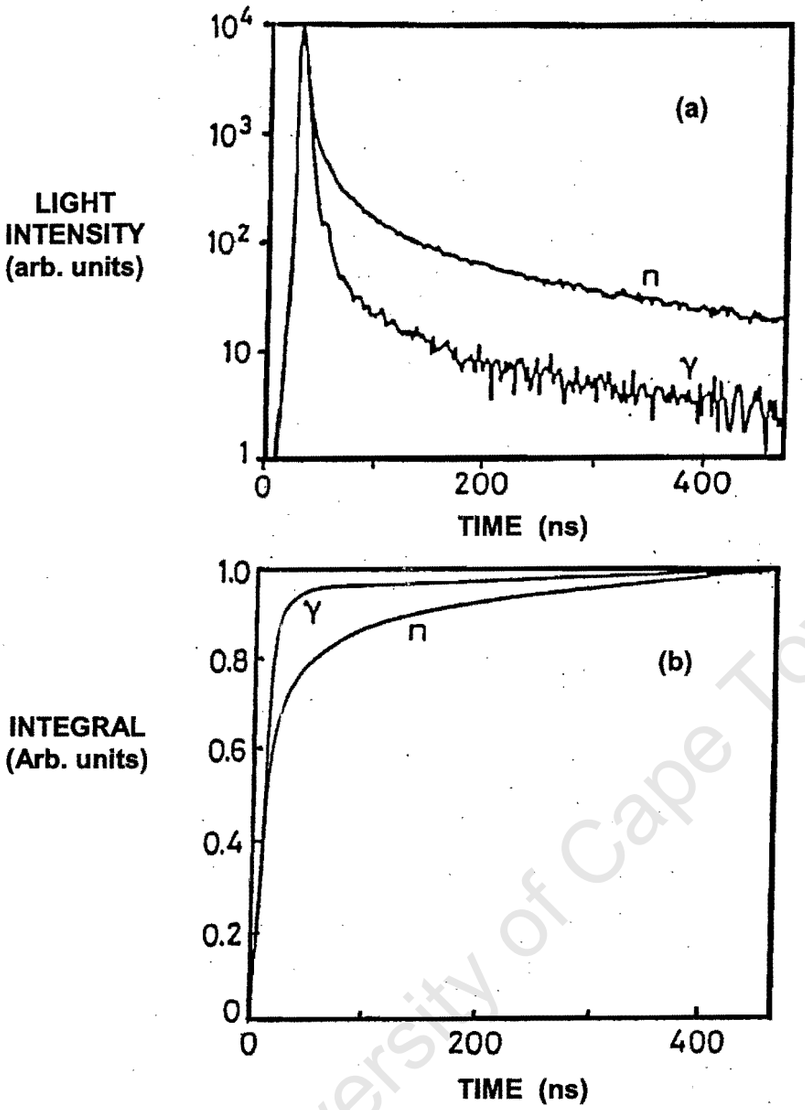

Figure 1.3. (a) Measured light intensity versus time t [Ly75] for scintillations produced by gamma rays and neutrons in an NE213 liquid scintillator. (b) Integrals of measured curves in (a), normalized at t = 500 ns.

1.2 The response function of NE213

A pulse height spectrum measured by an organic scintillator for radiation of a specific energy is known as the response function of the scintillator, and results from the collection and sorting of all pulses resulting from interactions of the particular radiation in the scintillator. A pulse height spectrum will thus depend on: (i) the size, shape and geometry of the detector which includes effects associated with light collection efficiency, photomultiplier response, electronic noise, etc., (ii) the types of interactions induced by the particular radiation incident on the detector, and their cross sections, and (iii) the energy of the incident radiation. The response function for neutrons incident on NE213 may be understood in terms of contributions from two sources, namely (i) recoiling protons from n–p elastic scatterings and (ii) outgoing charged particles produced from neutron-induced interactions with ^{12}C nuclei. These components differ in relative proportion at different incident neutron energies, depending on the cross sections of the competing nuclear interactions. Figure 1.4 shows the total cross sections for (a) n–^{1}H interactions and (b) n–^{12}C interactions [Mc88] for neutron energies between 5 and 200 MeV.

There are many papers describing measurements of NE213 response functions at various incident neutron energies (see for example, [Ve68, Lo76, An79, Ce79, Sc98, Na01, Ta01, Kl02]). The response functions at energies below about 15 MeV are highly dominated by n–p elastic scattering [Kl02]. At these lower energies, the energy spectrum of recoil protons from n–p elastic scattering can be regarded, to a good approximation, as isotropic in the centre-of-mass system. With increasing neutron energy, p-wave and higher order scattering become significant and the energy spectrum becomes increasingly forward-backward peaked. Figure 1.5 shows the measured (histograms) and calculated (smooth lines) response functions of a cylindrical NE213 liquid scintillator (5 cm (diam) × 5 cm (length)) to monoenergetic neutrons of energies (a) 2.52, (b) 7.93, (c) 15.0 and (d) 18.98 MeV [Kl02]. The calculations were made using the Monte-Carlo code NRESP [Di82]. The upper edges of the response functions, broadened by the detector resolution, correspond to protons recoiling forward with maximum energy from n–p elastic scattering interactions. The spectra display a good agreement between the measurements and the simulation for all four response functions over the entire pulse height range.

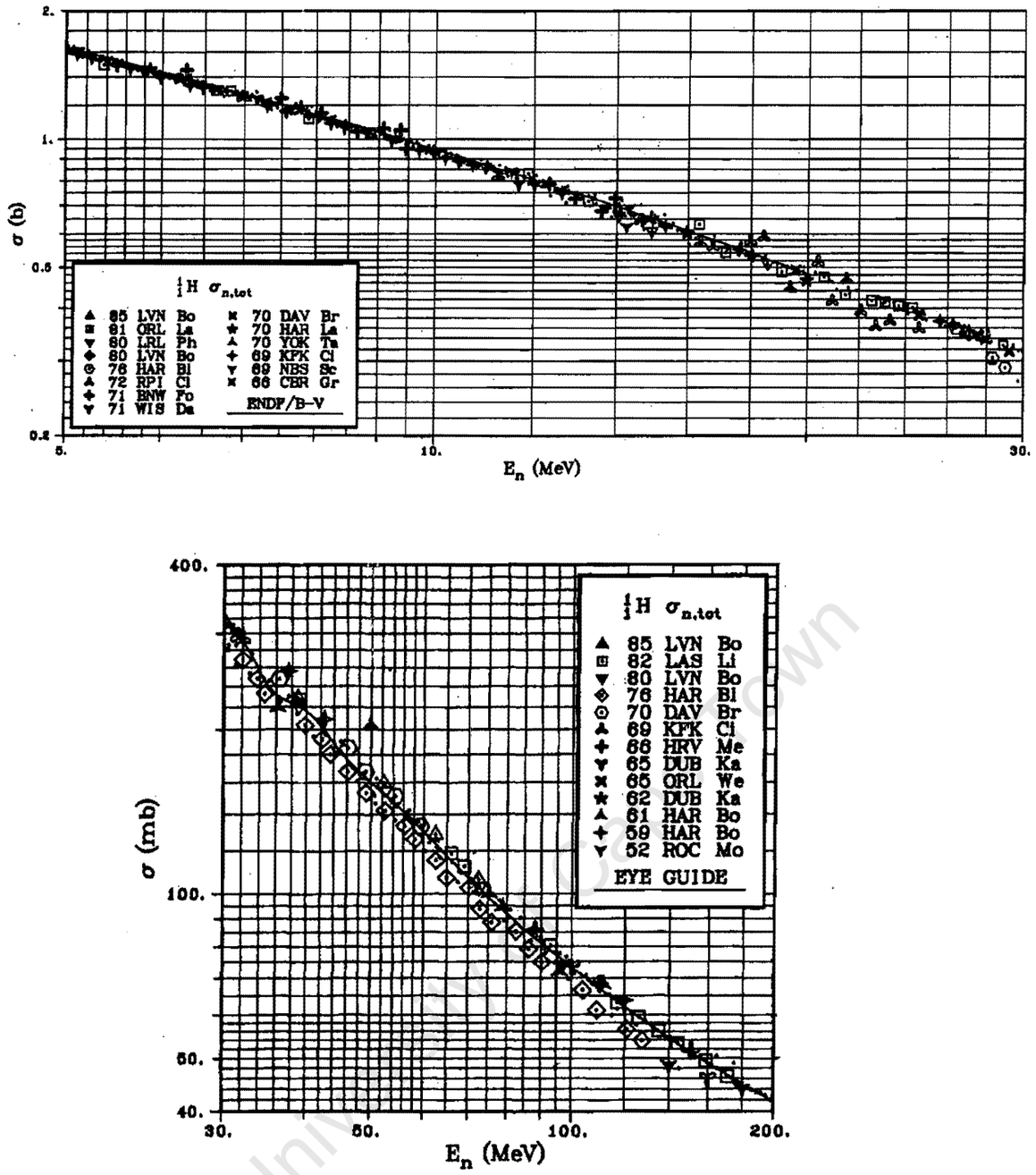

Figure 1.4 (a). Total cross sections for n– ^{1}H interactions [Mc88]. The curve is for guiding the eye.

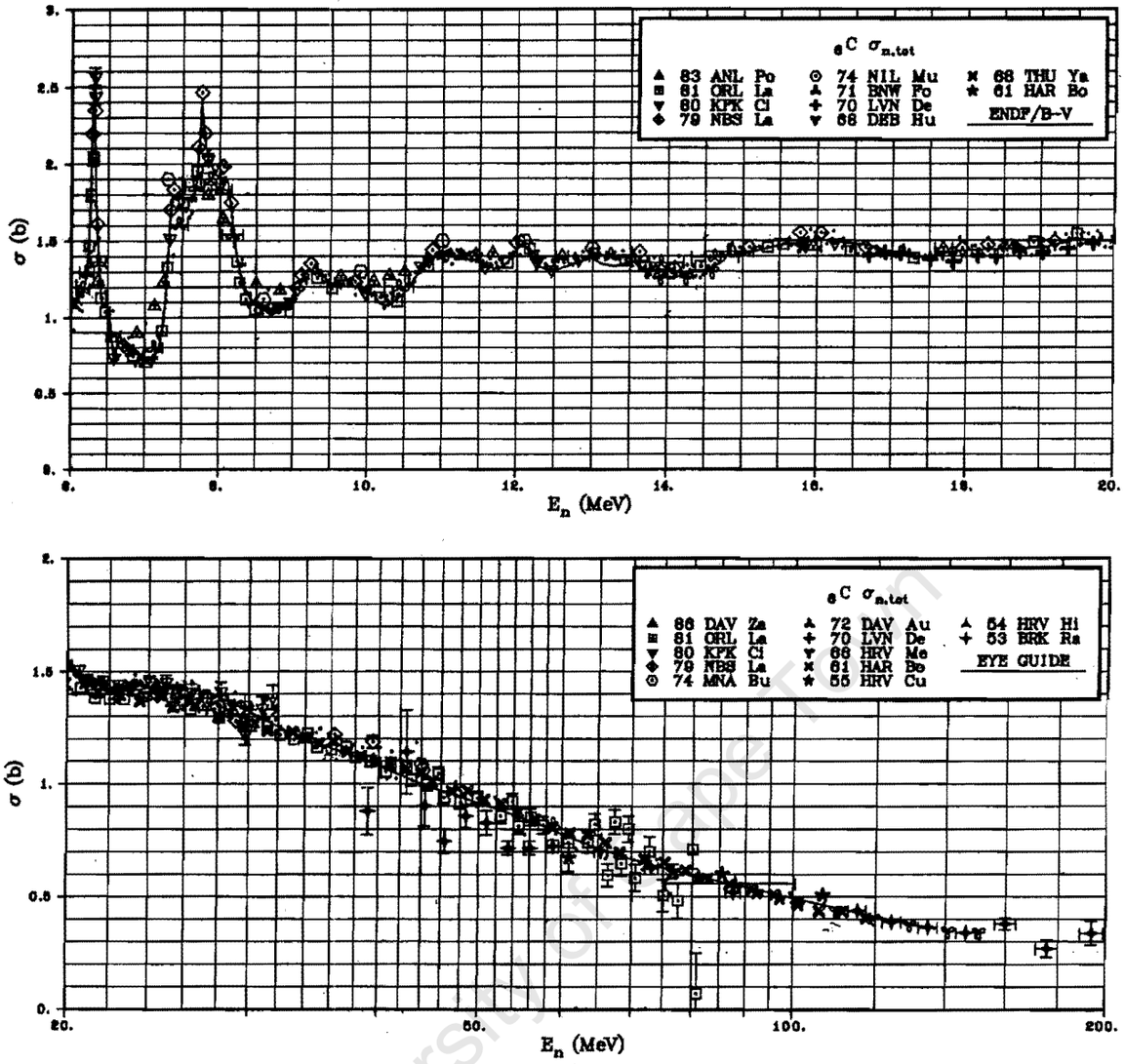

Figure 1.4 (b). Total cross sections for n– ^{12}C interactions [Mc88]. The curve is for guiding the eye.

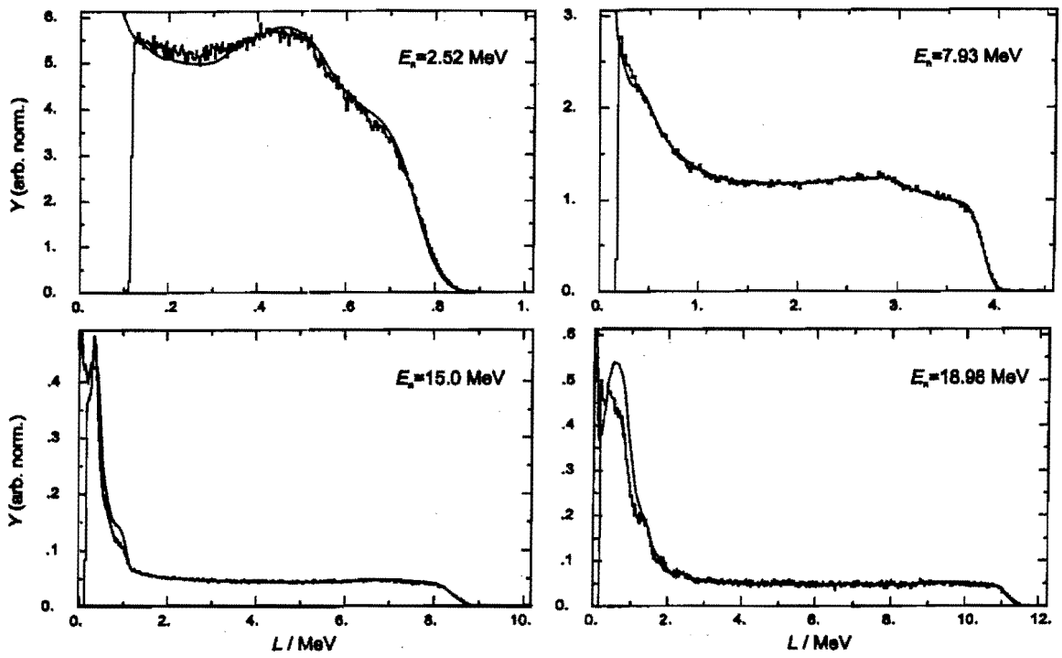

Figure 1.5. Pulse height spectra Y(L) measured (histograms) with a cylindrical NE213 liquid scintillator (5.08 cm in diameter and length) for neutrons of energy (a) 2.52 MeV, (b) 7.93 MeV, (c) 15.0 MeV and (d) 18.98 MeV, compared with response functions calculated (smooth curves) with the NRESP code [Kl02].

At higher neutron energies (> 15 MeV), neutron-induced reactions on ^{12}C increase in prominence as the thresholds for these reactions are exceeded and their cross sections increase. It can be seen from figure 1.4(b) that from incident neutron energies of about 30 MeV there are fewer cross section data available for n–^{12}C interactions. Furthermore, at the higher energy region, the data available from different sources, as labelled, are not in good agreement with each other. More than 60 reaction channels for the neutron-induced break-up of ^{12}C at 90 MeV have been identified [Ke53], each of which includes one or more charged particles in the products, such as protons, deuterons, tritons and alpha particles. Table 1.1 [Uw82] shows a few main reactions of neutrons with hydrogen and carbon, together with their Q-values and threshold energies. Since the cross sections for all these reactions are not well known, the interpretation of a response function measured by NE213 becomes increasingly complex with increasing neutron energy. Lockwood *et al.* [Lo76] stressed the importance of better pulse shape resolution that could give a more accurate determination of cross section measurements for neutron-induced charged particle production from carbon at neutron energies above 20 MeV.

Table 1.1: Some interactions of neutrons with ^{1}H and ^{12}C with their Q-values and threshold energies [Uw82].

Reaction	Q-value (MeV)	Threshold energy (MeV)
$^{1}H(n,n)^{1}H$	0	0
$^{12}C(n,n)^{12}C$	0	0
$^{12}C(n,n')^{12}C$	-4.43	4.80
$^{12}C(n,\alpha)^{9}Be$	-5.71	6.18
$^{12}C(n,n'3\alpha)$	-7.65	8.29
	-9.63	10.42
	-11.10	12.01
	-12.73	13.79
$^{12}C(n,np)^{11}B$	-15.96	17.29
$^{12}C(n,p)^{12}B$	-12.61	13.69
$^{12}C(n,d)^{11}B$	-13.73	14.90
$^{12}C(n,2n)^{11}C$	-18.72	20.13

Figure 1.6 shows a response function measured with a 13 × 13 × 7 cm^3 NE213 scintillator for incident neutrons of energy 62.5 MeV (adapted from [Bu02]). The region $L > L_T$ indicates the contribution to the response function associated with protons recoiling from n–p elastic scattering events only [Wa74]. The position of L_T is approximately 12.6 MeV less than the upper pulse height edge (62.5 MeV) which corresponds to the threshold of the main proton producing reaction ($^{12}C(n,p)^{12}B$) (see Table 1.1). The four Q–values listed for the $^{12}C(n,n'3\alpha)$ reaction are associated with the different channels for this reaction. Since the total cross section for n–p elastic scattering is well known up to about 200 MeV (see figure 1.4(a)), the region $L > L_T$ can be selected and used for calculating the efficiency of the detector and hence the neutron fluence, if the effect of proton escape is included in the analysis. Figure 1.7 shows a pulse height spectrum measured with a NE213 scintillator of dimensions 5.1 cm diameter and 10.2 cm length for 46 MeV neutrons [Sc98]. Also shown is a calculation using the code SCINFUL [Di88] (thin line). The disagreement between the measured and calculated response functions in the region $h < 130$ is evident. However, agreement is good in the upper region of the pulse heights spectrum ($h > 130$) which is due to n–p elastic scattering only.

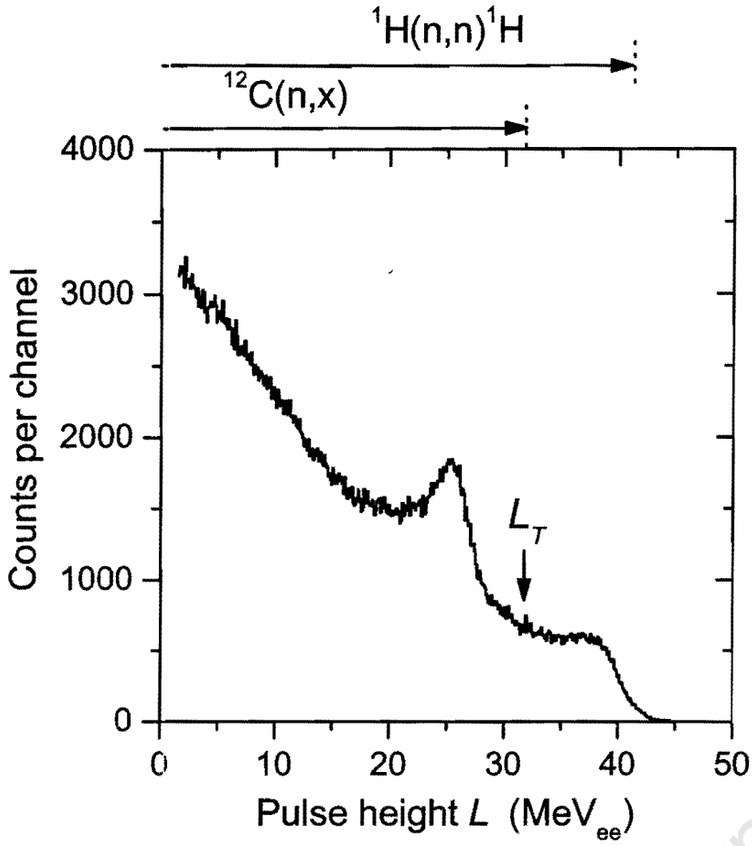

Figure 1.6. A response function measured with a 13.0 × 13.0 × 7.0 cm^3 NE213 liquid scintillator for incident neutrons of energy 62.5 MeV (adapted from [Bu02]). The region $L > L_T$ is associated with the detection of protons recoiling from H(n,n)H interactions only.

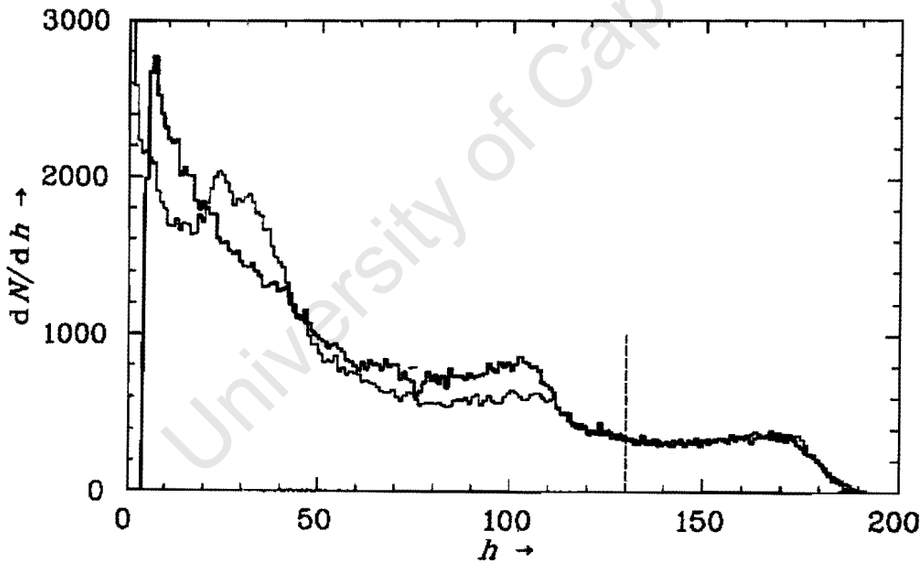

Figure 1.7. Pulse height spectrum dN/dh [Sc98] measured (thick line) with a cylindrical NE213 liquid scintillator (5.1 cm in diameter and length 10.2 cm) for neutrons of 46 MeV, compared with the response function calculated (thin line) with the SCINFUL code [Di88].

1.3 Neutron detection efficiency

The efficiency $\varepsilon(E_n)$ of a neutron detection system may be understood as the probability of the system being able to detect a neutron of energy E_n. In the case of a NE213 detector, for a neutron to be detected it must transfer enough energy to a charged particle (most often a proton) for the scintillation pulse to exceed the electronic detection threshold of the detection system. The efficiency of an NE213 detector will therefore depend on: the energy of the incident neutrons; the total cross sections of the nuclear interactions contributing to the detection of the incident neutrons; the size, shape and geometry of the detector; the electronic detection threshold of the system; and any other electronic selection, if applied.

Accurate knowledge of the efficiency is required if the detector is being used to measure neutron fluence. However, since the cross sections for the many n–^{12}C reaction channels are not well-known, this has become one of the persistent problems in work using organic scintillators. There has therefore been steady development over the years in both experimental techniques and in Monte Carlo codes used to estimate detection efficiencies.

At neutron energies below 20 MeV, techniques for measurement of neutron fluence with NE213 detectors are relatively well established and documented (see for example, [Br91, Sc97, Sd98]). Since the cross sections for both n–p and n–C interactions in this energy region are relatively well known, pulse height spectra can be accurately simulated by Monte Carlo codes such as NRESP [Di82], SCINFUL [Di88] and MCNPX [Wa02]. Nuclear reactions on light nuclei provide a useful variety of monoenergetic (or nearly monoenergetic) neutron sources in this range which may be used to validate simulated response functions. Furthermore, neutron fluence is readily obtained by accurately matching a simulated response function to experimental data over the entire pulse height range (see for example figure 1.5).

At neutron energies above 15 MeV, the situation is less favourable owing to two problems which arise. In this energy region, the contribution of multi-particle break up from neutron reactions on carbon increases, as discussed above. Since the cross sections for these interactions are not well known, Monte Carlo simulations are less reliable. The second

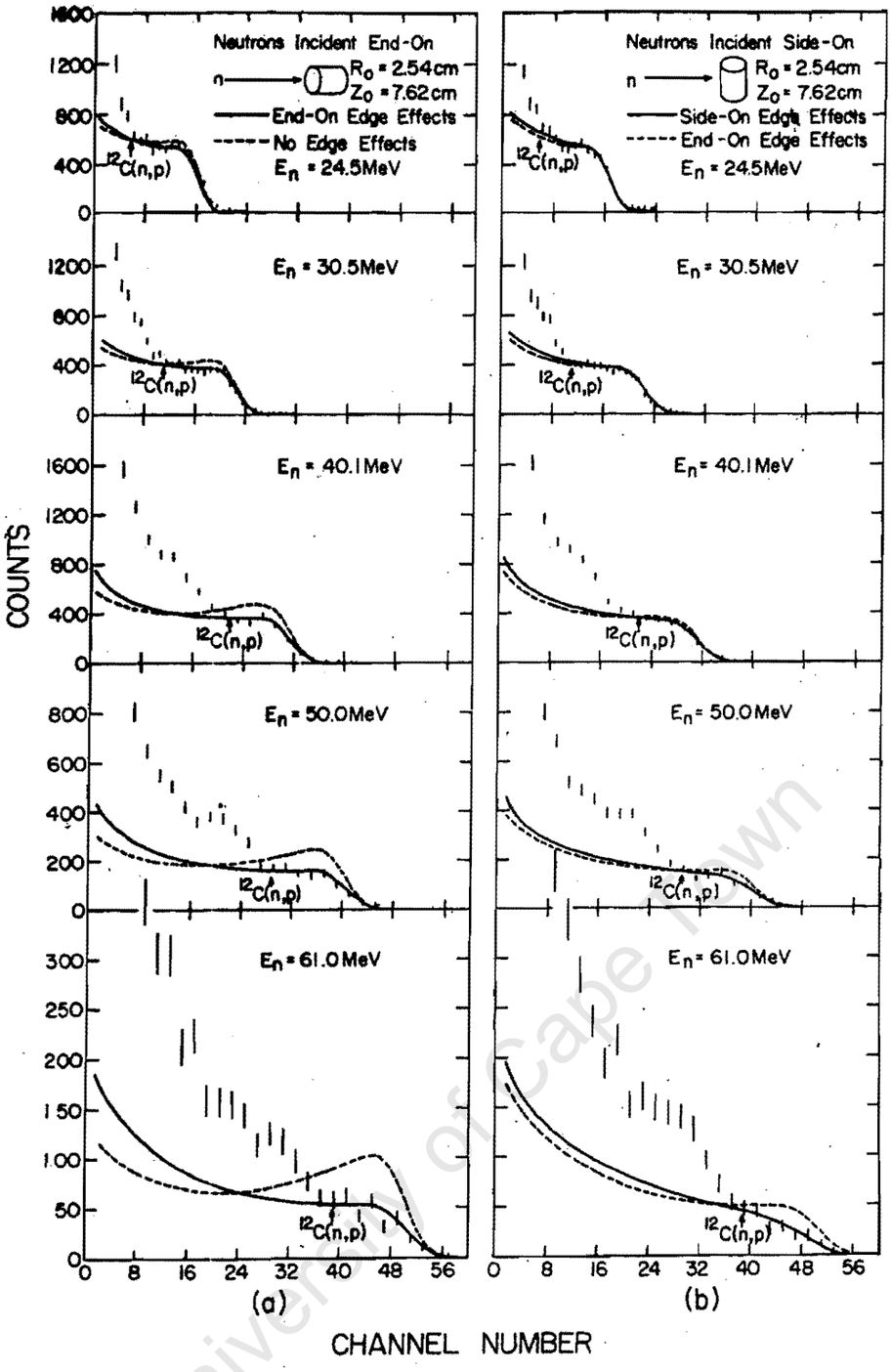

Figure 1.8. Experimental and calculated pulse height spectra for neutrons of five different energies incident on a 2.54 cm radius by 7.62 long cylindrical capsule of NE218 [Wa74]. Column (a) shows results for neutrons incident "end-on" whereas column (b) shows results for neutrons incident "side-on". The threshold below which the $^{12}C(n,p)^{12}B$ reaction can contribute events is indicated in each spectrum. For both orientations, the vertical bars are the measurements, the solid lines are Monte Carlo calculations with proton escape and the dotted lines are Monte Carlo calculations without proton escape.

problem is associated with charged particle recoils which escape from the detector (so-called "edge" or "wall" effects). As the range of recoiling charged particles in the scintillator increases with neutron energy, the proportion of escapes also increases, which distorts the shape of measured response function (e.g. at an incident neutron energy of 100 MeV, the proton range is 8.7 cm). Figure 1.8 [Wa74] shows measurements and calculations of pulse height spectra for incident neutrons between 24.5 and 61.0 MeV using a cylindrical NE218 detector (radius 2.54 cm, length 7.62 cm), orientated both (a) "end-on" and (b) "side-on" to the incident neutron beam. For both orientations, the vertical bars are the measurements, the solid lines are Monte Carlo calculations with proton escape and the dotted lines are Monte Carlo calculations without proton escape, using a custom written Monte Carlo code [Wa74]. It can be seen that with increasing neutron energy the effect of proton escape is more prominent when the detector is oriented "end-on" to the beam.

One solution to this problem would be to use a larger detector. This however, introduces a number of new difficulties. The first problem is associated with increased multiple scattering in the scintillator which affects the shape of the measured spectrum. The second problem is that it is not easy to ensure uniform light collection in large detectors which results in poor pulse height resolution. For example, Klein *et al.* [Kl79] studied the influence of geometrical and optical parameters on the light collection within scintillator assemblies, and were able to improve the light collection by using partially coated light guides. It should also be noted that for any size of detector, the proportion of escaping charged particles will never be zero.

1.4 The stacked scintillator spectrometer

The stacked scintillator spectrometer used in this work was designed [Bu02] to deal with the escape problem at high incident neutron energies, while retaining the simplicity of a standard single-scintillator geometry. The principle of the stacked scintillator is explained with reference to figure 1.9. Neutrons in the beam under study are incident normally on a thin-walled slab of scintillator A of thickness *a.* Behind A is a similar scintillator B of thickness *b,* or stack of scintillator slabs providing a total thickness *b* of

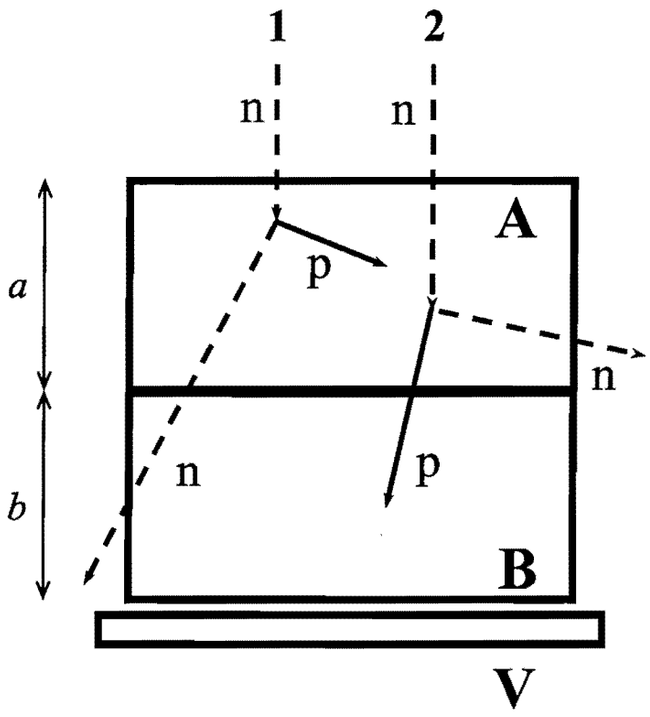

Figure 1.9. Geometry of the stacked scintillator spectrometer (see text).

liquid scintillator. Scintillators A and B are optically separate from each other and are serviced by separate photomultipliers and electronics. Neutron pulse height spectra are measured for both "singles" events (A-only, event type 1 in figure 1.9) and for "coincidence" events (A+B, event type 2 in figure 1.9). Pulse height spectra from detector A alone are determined for the singles events. The spectrum of summed (A+B) pulse heights is determined for the coincidence events. The A-only condition ensures that events with escaping charged particles are excluded from the singles spectrum. By choosing the thickness *b* and the pulse height thresholds applied to A and B, it is ensured that all (A+B) coincidences accepted for analysis correspond to events in which a proton or other charged particle starts in A and comes to rest in B. The veto detector, V, excludes all other event types. The sum of the "singles" (event type 1) and "coincidence" (event type 2) spectra results in the measurement of an "escape free" response function.

A similar technique was applied by Dias *et al.* [Di84, Di92] who designed a detector consisting of dual thin plastic scintillators. Their detector had a total thickness covering the maximum proton range of energy 15 MeV. The work successfully showed the experimental elimination of escaping protons which would otherwise distort the measured pulse height spectrum. Figure 1.10 shows the geometry of the dual thin plastic scintillator

used by Dias *et al.* in their work [Di84]. The detector consisted of two NE110 plastic scintillators to which a light guide and a photomultiplier were connected on each side. Figure 1.11 shows the pulse height spectra measured (dots) by the dual scintillator for neutrons of incident energy 14 MeV [Di84]. Spectrum A is measured by the first scintillator whereas spectrum B is the coincidence spectrum for both scintillators. Spectrum C, which is the sum of spectra A and B, approximates the ideal thin scintillator response function. The solid lines are Monte Carlo calculations using the code CARLO BLACK [Po72].

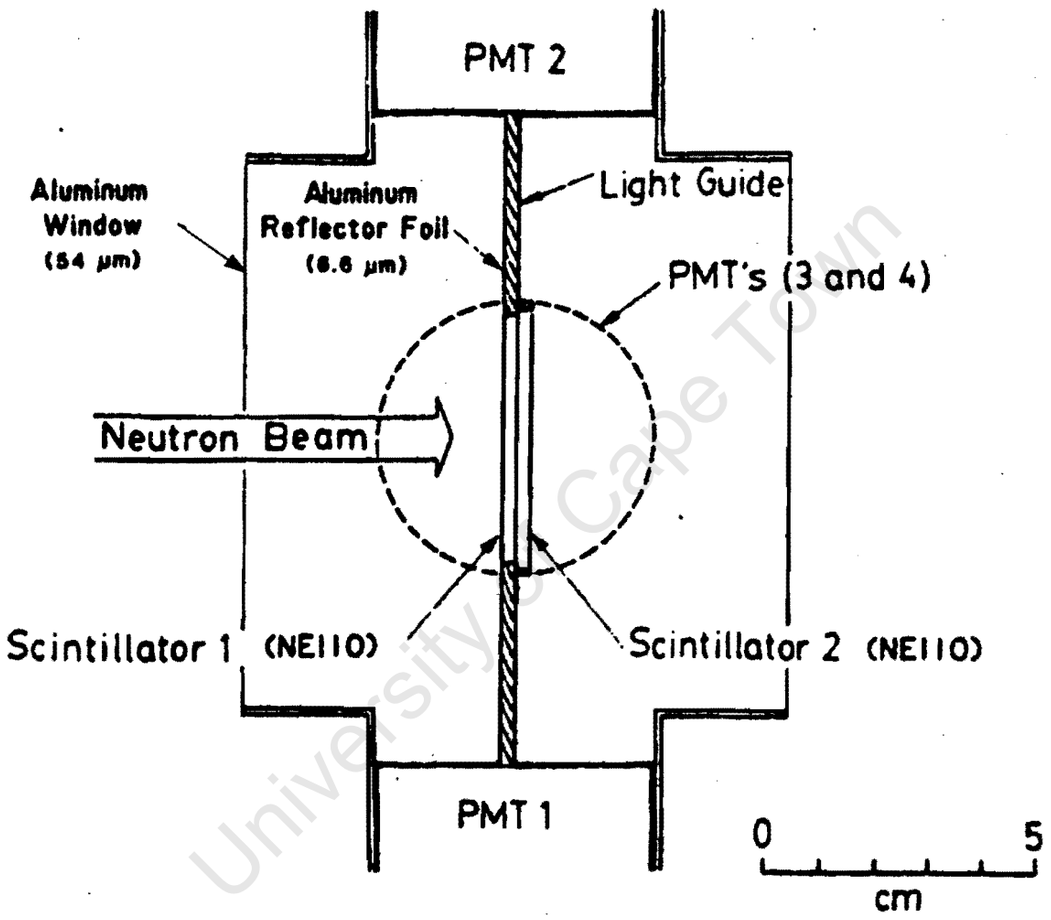

Figure 1.10. Geometry of the dual thin scintillator developed by Dias et al. [Di84].

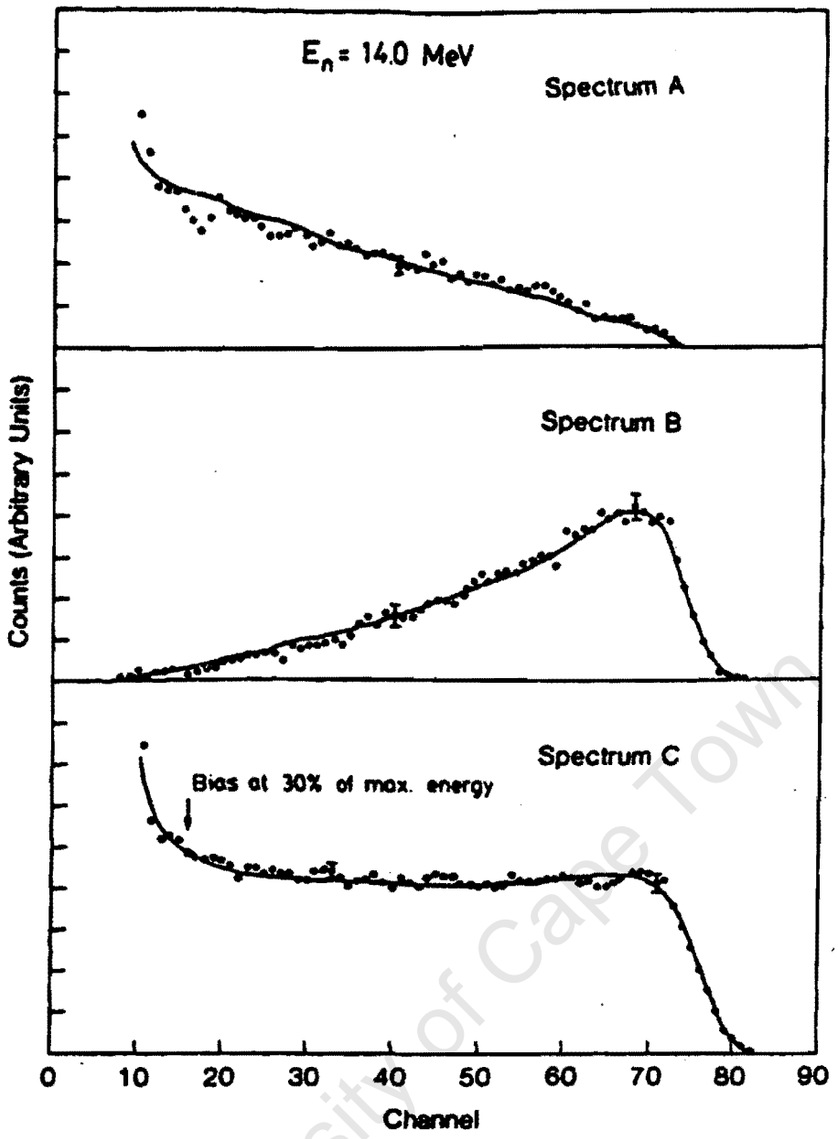

Figure 1.11. Experimental pulse height (dots) spectra obtained in an associated-particle experiment at 14 MeV [Di84]. Spectrum A is from the first scintillator whereas spectrum B is the sum coincidence of both scintillators. Spectrum C, which is the sum of spectra A and B, approximates the ideal thin scintillator response function. The solid lines are Monte Carlo calculation using the code CARLO BLACK [Po72].

1.5 The present work

This project illustrates some new aspects of the use of a stacked spectrometer which has been developed [Bu02] in the Physics Department of the University of Cape Town. The spectrometer used in the present work consists of two identical segments of NE213 liquid scintillator, of dimensions 13.0 × 13.0 × 7.0 cm^3, stacked behind one-another, and allows response functions to be measured for neutrons of energy up to 100 MeV, which are minimally affected by charged particle escape. The main contribution of the present work is a demonstration of the use of the spectrometer to measure neutron spectral fluence using unfolding analyses.

Experiments were conducted at the neutron time-of-flight facility at the iThemba LABS in South Africa. Neutrons were produced by bombarding protons of energy 99.21 MeV onto lithium and graphite targets. The spectrometer was used in conjunction with neutron beams produced at two angles (0° and 16°) for the different targets used. Using the data measured at 0° and for a 3 mm natural lithium target, a set of 16 response functions for quasi-monoenergetic neutron beams covering the neutron energy range 20-100 MeV, were selected by time-of-flight. For each of these 16 response functions, a pulse height threshold was set so as to select only events associated with n–p elastic scattering and exclude contributions from n–^{12}C interactions. This allowed the efficiency of the spectrometer to be measured and hence the neutron fluence for each energy bin. These neutron fluence measurements were used to normalize each response function to one neutron cm^{-2}, which were then collated to form a response matrix for the spectrometer covering the energy range 20 to 100 MeV. Pulse height spectra measured for other neutron beams could then be analysed using unfolding analyses which resulted in measurements of energy spectra for these beams.

2

Experiments

2.1 Neutron production

The experiments [1] were carried out using the $k = 200$ separated sector cyclotron facility at the National Accelerator Centre (NAC), (now called iThemba Laboratories for Accelerator-Based Sciences (LABS)) in Faure, outside Cape Town, South Africa [ITH]. Figure 2.1 shows a schematic diagram of the layout of iThemba LABS. Figure 2.2 schematically shows the configuration for the measurements which were carried out in the D-line vault (figure 2.1). A pulsed proton beam of energy 99.21 MeV and frequency 19664.175 kHz was produced by the cyclotron. Every sixth proton pulse from the cyclotron (period 50.854 ns) was selected by a pulse selector to give the desired period of 305.1 ns between each burst of protons. The beam was transported, via the X, P1 and R beam lines, (see figure 2.1) to the experiment vault (D) where it was directed onto a neutron-producing target.

[1] The work described in this thesis forms part of a larger collaborative project between the Department of Physics at the University of Cape Town, and the Department of Neutron Metrology at the Physikalisch-Technische Bundesanstalt (PTB), Braunschweig, Germany. Part of the work is aimed at the development of different methods of measuring neutron fluence at energies between 70 and 200 MeV. The collaboration has thusfar received 6 weeks of beamtime at the IThemba LABS over the last 3 years.

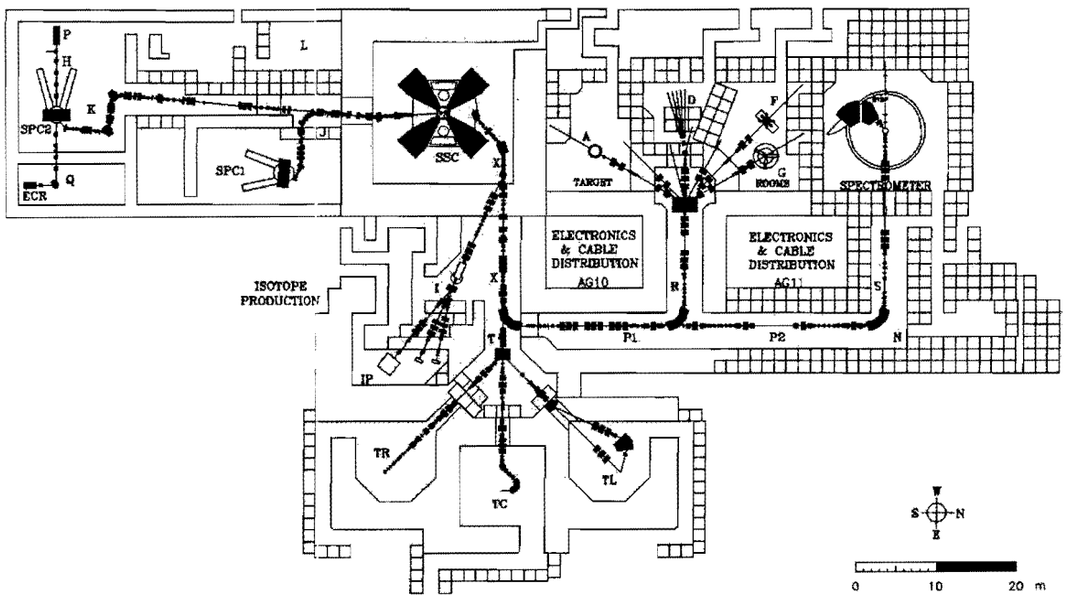

Figure 2.1. Layout of the National Accelerator Centre, showing the proton production area and the different experiment vaults.

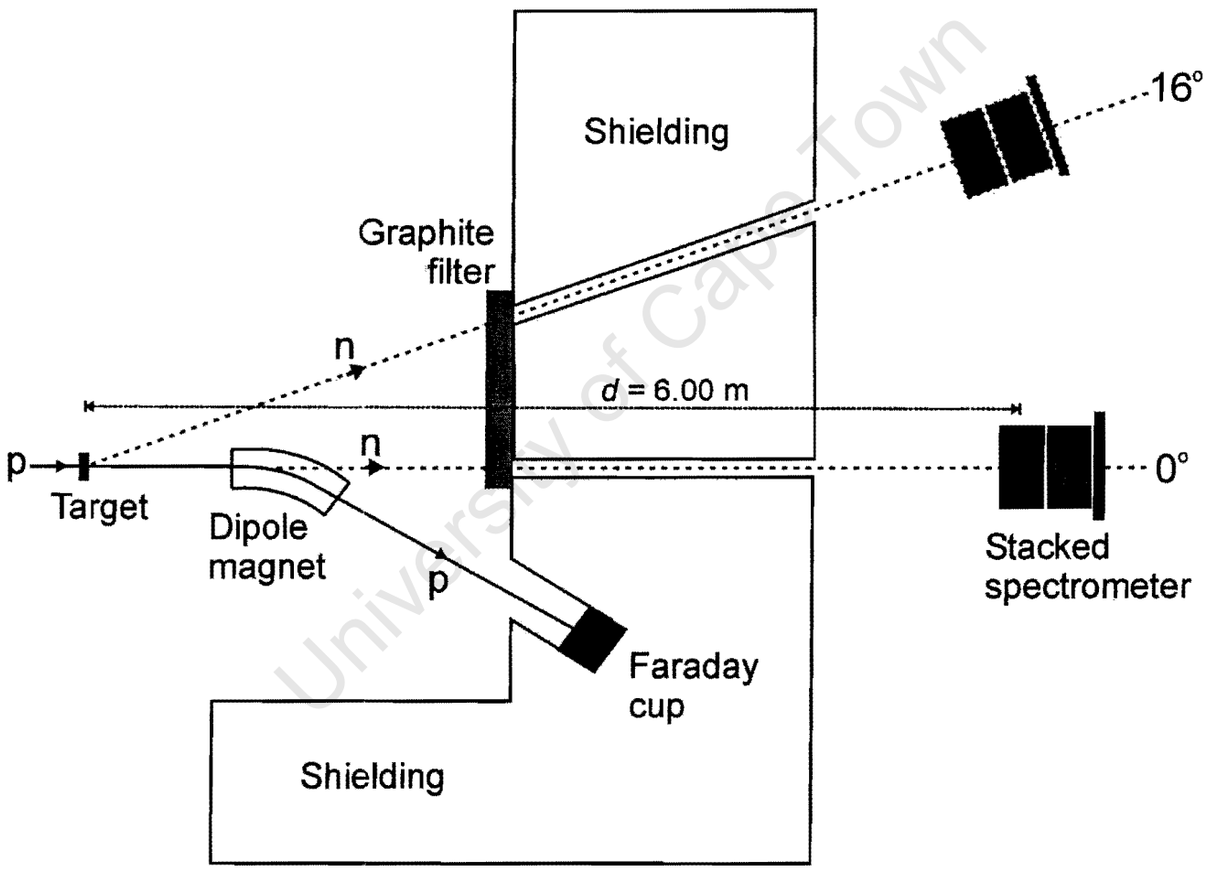

Figure 2.2. Schematic representation of the detector setup and shielding in the vault.

Three different targets were used in this work, viz. 3 mm natural lithium, 5 mm natural lithium and 10 mm graphite. Table 2.1 lists the values of the total energy loss, ΔE of a 99.21 MeV proton beam in each target, calculated using the program ELOSS [Ji84]. The average energy loss of the proton beam in each target was then taken to be $\Delta E/2$. The average energy of the proton beam in the target, $\overline{E}_{\mathrm{p}}$ is given then by

$$\overline{E}_{\mathrm{p}} = E_p \text{ (incident)} - \frac{\Delta E}{2}. \tag{2.1}$$

The FWHM of the proton beam was estimated by the beam operators to be 200 keV.

Table 2.1: Neutron producing targets used in this work together with the calculated total energy loss, ΔE and the resulting average energy, $\overline{E}_p$ from incident protons of energy 99.21 MeV.

Target	Thickness (mm)	ΔE (MeV)	$\overline{E}_{\mathrm{p}}$ (MeV)
Natural Li	3	0.964	98.728
Natural Li	5	1.612	98.404
Graphite	10	15.868	91.276

The maximum neutron energy, E_n(max) at 0° and 16° for the different reactions was calculated using the KINMAT program [Ba61, Mi67] which makes use of standard non-relativistic two-body kinematics, and the results are shown in Table 2.2.

Neutron beams at 0° and 16° were created by 5.0 × 5.0 cm^2 apertures in the shielding wall between the target and experiment areas (see figure 2.2). The collimation wall consists of 4 m iron, 25 cm borated paraffin wax and 4 cm borated polyethylene. The borated polyethylene assists to prevent thermal neutrons from reaching the detectors. For the measurements, the stacked spectrometer system was placed 2.025 m from the exit of the apertures, giving a flight path between the target and the centre of the first detector segment (detector A) of 6.000(21) m. The height from the vault floor to the stacked scintillator system was measured to be 1.492(5) m. Protons that were transmitted through

the target were deflected by a dipole magnet into a beam dump incorporating a Faraday cup. A graphite block of thickness 10 cm was placed at the entrance of the collimator (see figure 2.2) to stop any stray protons, not removed by the dipole magnet, from reaching the stacked spectrometer.

Table 2.2: The KINMAT [Ba61, Mi67] results for the different targets showing the Q-values and maximum neutron energies for different reactions at different angles.

Target (mm)	Angle (^{0})	Nuclear Reaction	Q-value (MeV)	E_n(max) (MeV)
Natural Li (3)	0	^{7}Li(p,n)^{7}Be	-1.644	97.084
Natural Li (3)	16	^{7}Li(p,n)^{7}Be	-1.644	95.945
Natural Li (5)	0	^{7}Li(p,n)^{7}Be	-1.644	95.758
Natural Li (5)	16	^{7}Li(p,n)^{7}Be	-1.644	94.625
Graphite (10)	0	^{12}C(p,n)^{12}N	-13.120	78.156

2.2 The stacked scintillator spectrometer

The stacked spectrometer consisted of two NE213 modules and a plastic veto detector. Each NE213 module comprises a thin-walled (0.3 mm tinplate) cell of dimensions 13.0 × 13.0 × 7.0 cm^3 (see figure 2.3). The two glass faces of each scintillator cell are optically coupled to two RCA8850 photomultipliers [RCA] on each side using silicone jelly. Spring mountings are used to ensure that good light seals are maintained between the photomultiplier tubes and the glass faces of the cell. Each photomultiplier pair runs off a single high voltage (HV) power supply. The anodes and dynodes of the four photomultipliers are linked to form single anode and dynode output signals. These were adjusted as described below (section 2.4). The veto detector used in this work was a square (150 × 150 mm^2), 3 mm thick NE102A "paddle" which was mounted immediately behind detector B (see figure 1.9).

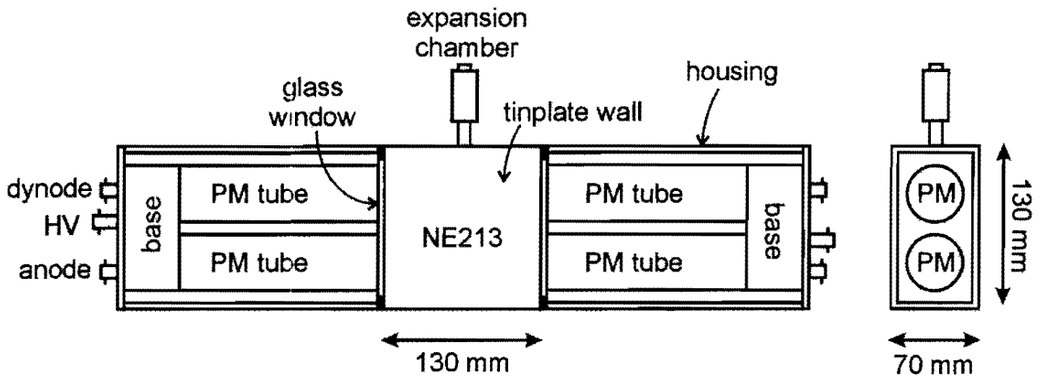

Figure 2.3. A schematic diagram of the NE213 liquid scintillators used in this work.

2.3 Electronics

Figure 2.4 shows a schematic diagram of the pulse processing electronics and data acquisition system used for the measurements. Signals were produced from three sources, namely the NE213 liquid scintillators detectors, A and B, the plastic veto detector (V) and a signal from the pulse selector of the cyclotron.

The eight parameters recorded for each event are summarized in Table 2.3. Similar electronic units were used to process the pulses from the detectors A and B. The fast outputs from the anodes of the four photomultipliers of each detector (A and B) were coupled together and fed directly into a modified [Sm87] Link System Model 5010 Pulse Shape Discriminator (LINK) [Ad78] which provided two outputs, L and F. The pulse height L was generated by integrating the scintillation pulse over a period of approximately 500 ns while the F pulse was obtained by integrating over approximately 30 ns [Ol92]. A pulse from the timing output of the LINK servicing detector A was used to start the time-to-amplitude converter (TAC) which measured the neutron time-of-flight T. The TAC was stopped with a pulse from the cyclotron's pulse selector. The signals from the 4th dynode outputs of the photomultipliers of each detector were coupled together and directed through a pre-amplifier and amplifier chain for an independent pulse height measurement (parameter D).

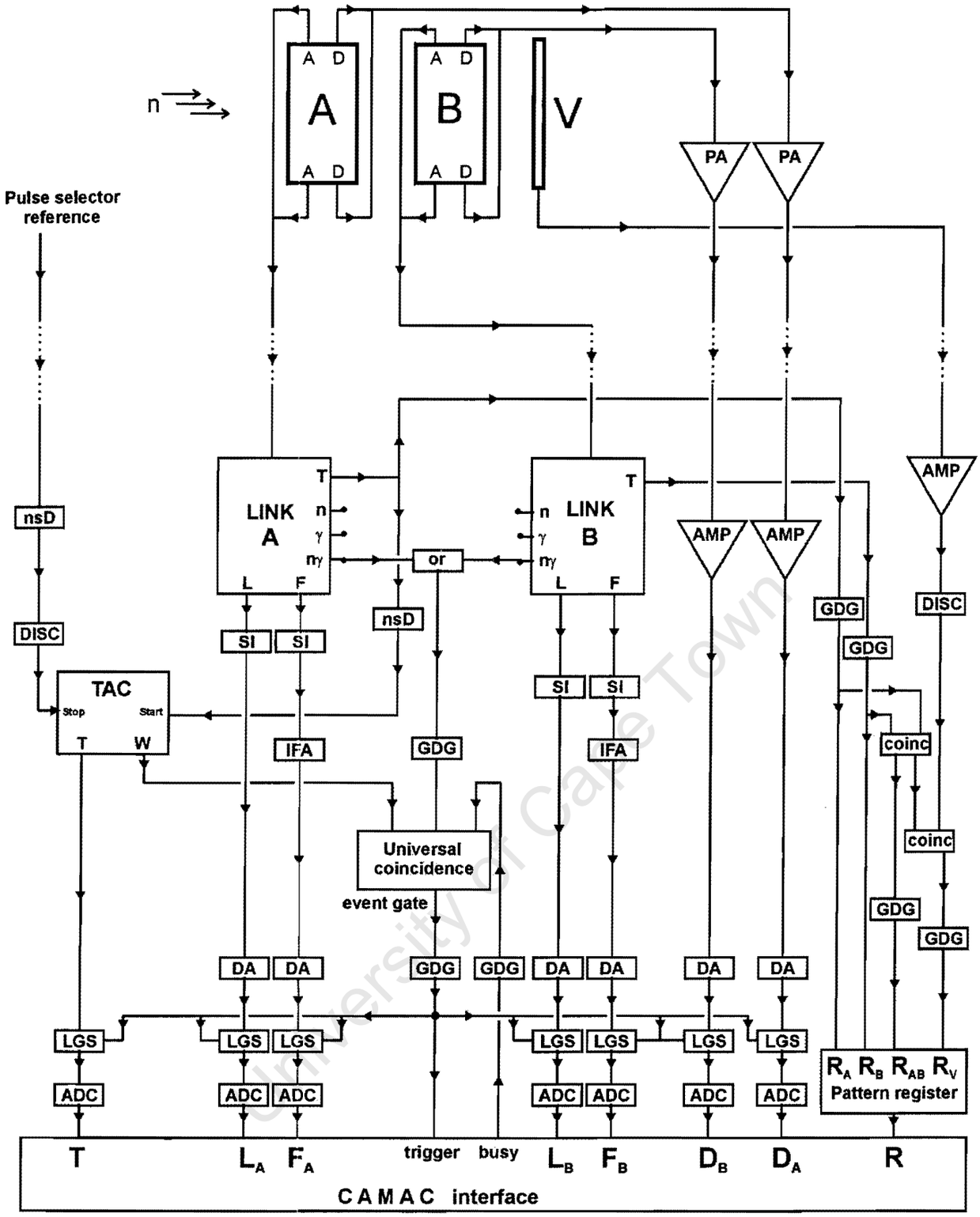

Figure 2.4. A complete circuit diagram of the electronic configuration used for pulse processing (see text for standard NIM definitions used).

Table 2.3: Parameters recorded for each buffered event during the experiments.

Parameter	Description	
L_A	Pulse height (long time integral) of anode pulse processed by LINK A	
F_A	Fast integral of anode pulse processed by LINK A	
D_A	Pulse height derived from 4th dynodes of photomultipliers of detector A	
L_B	Pulse height (long time integral) of anode pulse processed by LINK B	
F_B	Fast integral of anode pulse processed by LINK B	
D_B	Pulse height derived from 4th dynodes of photomultipliers of detector B	
T	Neutron time-of-flight	
R	R_A	Pattern register bit to identify detector A singles event
	R_B	Pattern register bit to identify detector B singles events
	R_{AB}	Pattern register bit to identify AB coincidence events
	R_V	Pattern register bit to veto escaping charged particles from detector B

With the LINK thresholds set at a pulse height corresponding to approximately 8 MeV electron energy, the LINKs were typically processing events at approximately 3 kHz. Timing signals from the two LINKs were also used to generate logic pulses which used to set the pattern register bits R to facilitate off-line separation of the events recorded by each detector. Singles events in detectors A and B were identified by bits R_A and R_B and a fast coincidence unit was used to provide a bit R_{AB}, used to AB-coincidence events. Signals from the veto detector V, in coincidence with signals from both detectors A and B, provided pattern register bit R_V, which was used to veto events associated with charged particles escaping from detector B.

A universal coincidence unit UCO, was used to gate the experiments. Logic pulses from one or both LINKs, and from the TAC SCA output (W) were required in coincidence, together with a busy logic level which was produced when required by the acquisition computer and was included as an anti-coincidence requirement. The output from the UCO was used to gate the linear gate and stretcher (LGS) units allowing the data to be passed to the ADC's for analogue to digital conversion, and also to trigger the acquisition computer.

All phases of the data acquisition were monitored on a system of displays and scalers. After electronic signal processing, the data signals were fed via CAMAC to a VAX acquisition computer running XSYS [IUCF] data acquisition under the VMS operating system. Event by event data were recorded in memory and buffered to disk in 4k blocks. The data were later replayed off-line and analysed event by event in multiparameter mode using custom-written FORTRAN analysis programs.

2.4 Calibrations with radioisotopic sources

Various calibrations were performed using the neutron beam as well as with an $^{241}Am/^{9}Be$ (AmBe) source. These included time and pulse height calibrations as well as measurements of the response functions of each detector for known sources of monoenergetic neutrons and γ-rays in order to inspect their overall performance and energy resolution. An AmBe source was also used to adjust the detector thresholds and gains, as well as the PSD settings on the LINK modules The gains of the two photomultipliers on each side of detectors A and B were set independently while the high voltage for the photomultipliers on the other side were switched off. This allowed the edges of the measured pulse height spectra to be set to the same pulse height channel.

AmBe sources provide a neutron spectrum predominantly below 10 MeV as well as a photon of 4.44 MeV from the decay of the corresponding ^{12}C state populated in the $^{9}Be(\alpha,n)^{12}C$ reaction. Figure 2.5 shows a pulse height calibration spectrum measured for the 4.44 MeV γ-ray from an AmBe source (selected by pulse shape discrimination), using detector A. The principle features of these response functions, labelled in figure 2.5, are the Compton edge (at 4.20 MeV) and double escape peak (at 3.42 MeV) which arises from the pair interaction of the 4.44 MeV γ-ray on the carbon component of the organic scintillator. This peak provides an unambiguous calibration reference, as its mean value is insensitive to both multiple scattering and the detector pulse height resolution. The mean free path of 0.511 MeV photons is approximately 9 cm in liquid scintillator, thus the photons created in positron annihilation events are likely to escape from the volume of these detectors. If the 0.511 MeV photon does interact, the probability that it deposits all its energy is very low, and therefore a single escape peak does not appear.

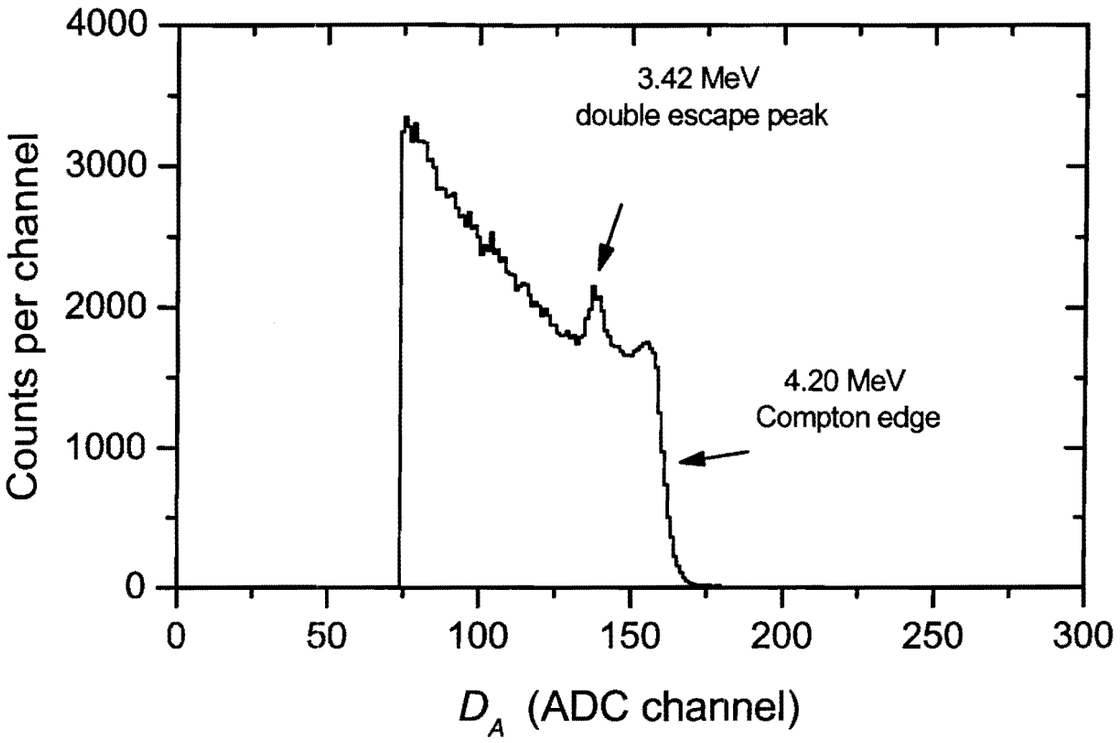

Figure 2.5. Pulse height calibration spectrum measured with detector A for the neutrons from an Am–Be source.

The energy of the Compton edge E_C of the 4.44 MeV γ-ray was calculated to be 4.20 MeV using [Kn89]:

$$E_C = \frac{2E_\gamma^2}{2E_\gamma + m_e c^2} \tag{2.2}$$

where $m_e c^2$ is the electron rest mass energy (0.511 MeV). The features in the response functions are affected by the geometrical dimensions of the sensitive volume of the detector. It is also possible that the electron, after having escaped from the scintillator volume, may be scattered back into the detector by the surrounding material, which will further affect the shape of the response function. These effects have been recently studied [No97] together with the contribution to the response function resulting from photons produced via neutron interactions in the metal casings of liquid scintillators.

The fast coincidence timing for the various components of the stacked spectrometer was set using the annihilation radiation from a ^{22}Na source.

2.5 Calibrations with the neutron beam

The anode pulse height gains of detectors A and B (parameters L_A and L_B) were matched, before any measurements were made with the beam, by adjusting the high voltages of detectors A and B until the upper edges of the pulse height spectra measured using the AmBe source were both at the same ADC channel. The dynode pulse height gains (parameters D_A and D_B) were first approximately matched using the D amplifiers. Two calibration runs were then completed using the neutron beam for careful off-line matching of the D gains. The three components of the stacked spectrometer were arranged as shown in the insert of figure 2.6, which shows the two transmission D-pulse height spectra measured for (a) detector A sandwiched between detectors B and V and (b) detector B sandwiched between detectors A and V.

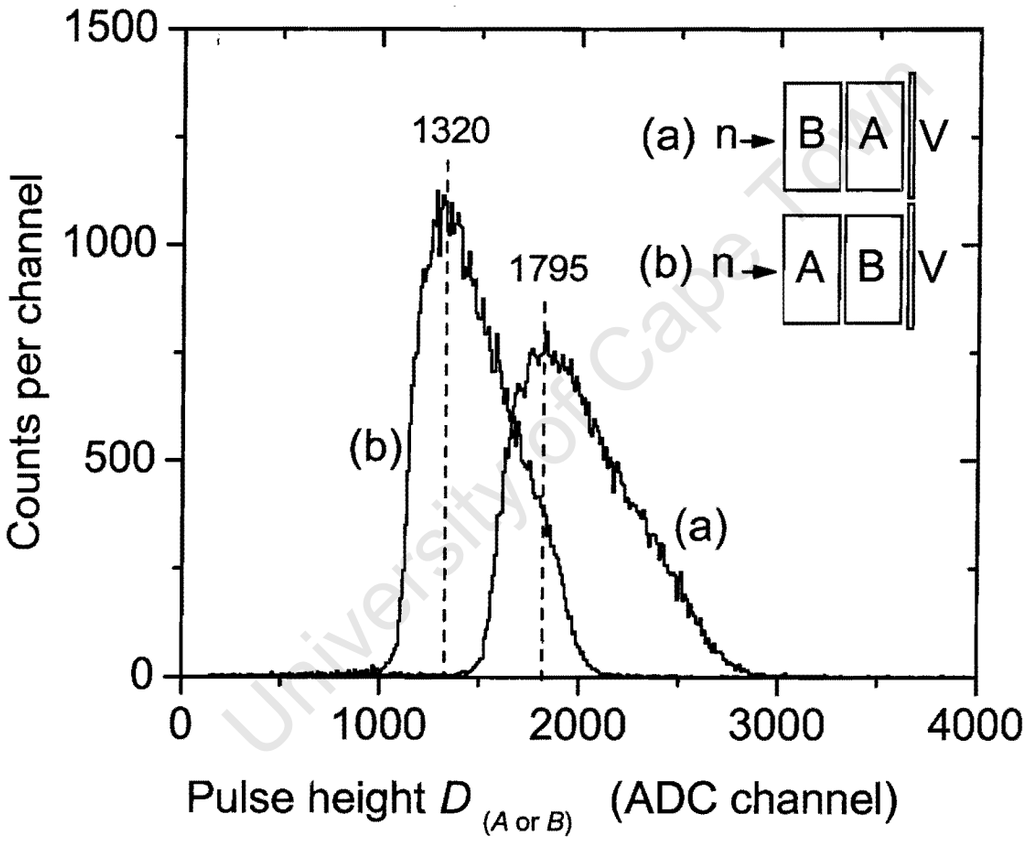

Figure 2.6. Pulse height spectrum measured by (a) detector A and (b) detector B for BAV and ABV triple coincidences, respectively. The positions of the transmission peaks provide a means to match the gains of the D_A and D_B parameters.

For these runs, either a (a) BAV or (b) ABV coincidence was required. The peaks in figure 2.6 are associated with charged particles recoiling from the first detector, completely traversing the middle detector and entering the veto detector V. The centres of the peaks (ADC channels 1795 and 1320 for detectors A and B respectively) provided a means for off-line matching of the gains of the D_A and D_B parameters.

2.6 Runs completed with the stacked neutron spectrometer

Table 2.4 shows the set of runs completed with the spectrometer together with the duration (in seconds) and the total number of events for each run. For the runs at 16°, the entire stacked spectrometer system (detectors A, B and V) were moved from their positions at 0° to 16°, such that the distance from the centre of the target to the centre of detector A was 6.000 m (see figure 2.2).

Table 2.4: Runs completed with the use of the stacked scintillator spectrometer.

Run label	Target (mm)	Angle	Time (s)	Events
G	Li (3)	0°	1889	4471363
H_1	Li (5)	0°	258	1428398
H_2	Graphite (10)	0°	1418	5709064
H_3	Li (3)	16°	912	3183590
H_4	Li (5)	16°	538	2074094

3

Data reduction

3.1 Time of flight to energy calibration

Figure 3.1 shows the time-of-flight (T) spectrum measured by the stacked spectrometer for the beam produced by bombarding a 99.21 MeV pulsed proton beam onto a 3 mm thick natural lithium target. The distance from the centre of the target to the centre of detector A was 6.000 m. The three spectra shown, selected by pulse shape discrimination, are associated with the detection of neutrons (n) produced via the ^{7}Li(p,n)^{7}Be reaction, gamma-rays (γ) and the sum of the neutron and gamma ray spectra (n+γ).

The sharp peak in the neutron spectrum at ADC channel 1546 is associated mainly with neutrons produced via the unresolved ground state and first excited state (0.429 MeV) transitions in ^{7}Be. The maximum energy of the neutrons emerging from the reaction at 0° was calculated to be 97.1 MeV (see Tables 2.1 and 2.2). The lower energy continuum of the spectrum displays a broad Maxwellian-like tail. These neutrons arise from excitation of higher states in ^{7}Be or from breakup reactions leading to three or more particles in the final state.

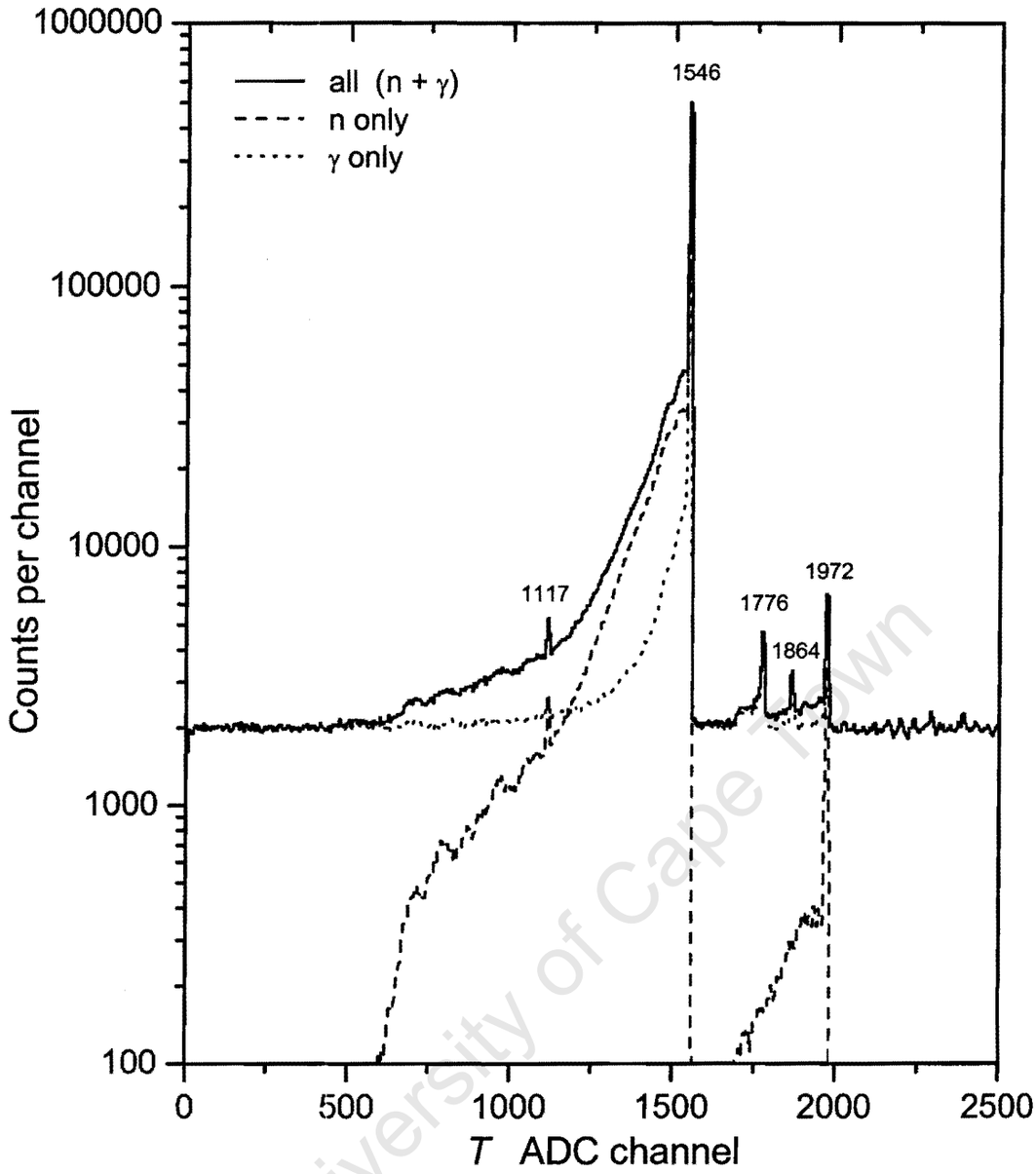

Figure 3.1. Time-of-flight spectrum measured by the stacked spectrometer for the beam produced by bombarding a 99.21 MeV pulsed proton beam onto a 3 mm thick natural lithium target. The distance from the centre of the target to the centre of detector A was 6.000 m. The three spectra shown, selected by pulse shape discrimination, are associated with the detection of neutrons (n) produced via the $^{7}Li(p,n)^{7}Be$ reaction, gamma-rays (γ) and the sum of the neutron and gamma ray spectra (n+γ).

The width of the main neutron peak may be attributed to energy losses of the incident protons in the lithium target prior to neutron production, and from the intrinsic time-of-flight resolution of the system. Two gamma peaks visible at channels 1776 and 1864 arise from the detection of gamma rays that were produced in, or around, the target and in the proton beam line. The inherent timing resolution of the system may be inferred from the width of these peaks. A flat, time independent gamma ray background continuum is also evident. Two smaller neutron peaks associated with pulse selector breakthrough appear at ADC channels 1117 and 1972. These provide an inherent calibration of the T scale.

In order to produce a proton beam of nominal energy 100 MeV, the cyclotron operates at a frequency value of 19.664 MHz. The period for each beam pulse is therefore 50.854 ns. A time calibration of 8.407 ± 0.042 channels/ns was then calculated using the positions of the two pulse selector breakthrough peaks identified at ADC channels 1117 and 1972. The 'time zero' T channel (T_0) was calculated using the well-known neutron time-of-flight equation:

$$T - T_0 = \left\{ \frac{72.3\, f\, d}{\sqrt{E_n}} \right\} \tag{3.1}$$

where:

T: neutron time-of-flight ADC channel;

d: distance from the centre of the ^{7}Li target to the centre of detector A (6.000 ± 0.021 m);

f: 8.407 ± 0.042 channels / ns;

E_n: neutron energy in MeV; and

72.3: scaling factor.

Using non-relativistic kinematics does not introduce more than 5% uncertainty to the calculation of E_n at these energies. Since the T ADC channel for the 97.1 MeV neutron peak was known (channel 1546), it could be used to calculate T_0 which was found to be at channel 1916. The neutron energy associated with any other T ADC channel could then be calculated using equation 3.1. Figure 3.2 shows the neutron time-of-flight spectrum (see figure 3.1) on which a neutron time-of-flight and corresponding energy scale are also now shown. The dashed lines show the T-window used to select the neutrons in the peak centred at energy of 97.1 MeV.

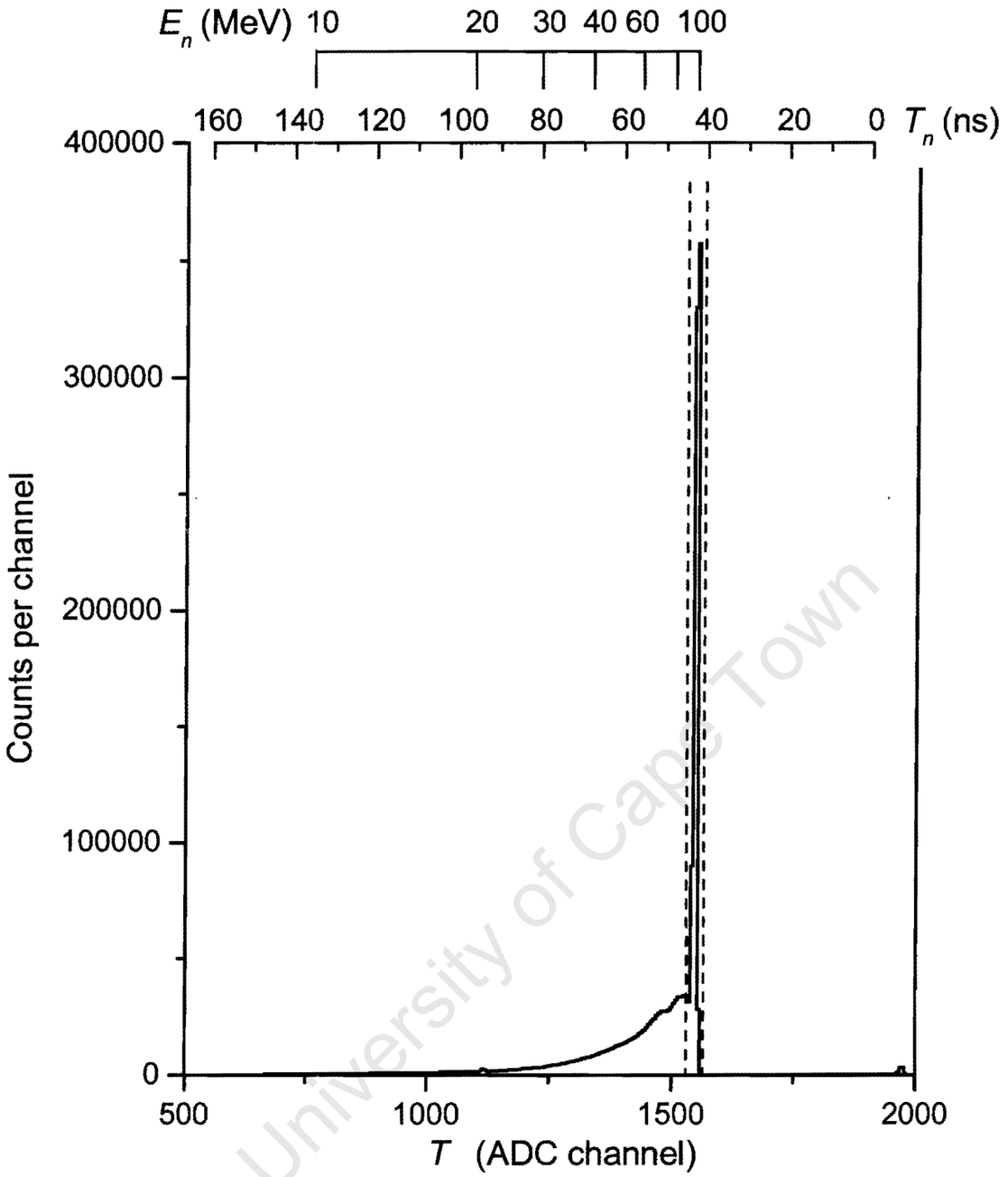

Figure 3.2. The neutron time-of-flight spectrum, shown in figure 3.1, on which energy (in MeV) and time (in nanoseconds) scales are shown (equation 3.1). The dashed lines indicate the T-window used to select neutrons of average energy 97.1 MeV.

The T ADC channel position of the peak associated with γ-rays produced in the target could be calculated using the equation:

$$T(gamma) = T_0 - \frac{d\,f}{c} \tag{3.2}$$

where:

c : the speed of light in a vacuum (0.3 m/ns)

d, f and T_0 : as for equation 3.1 above.

The T ADC channel for the gamma-rays produced in the target was then calculated to be 1748. The uncertainty associated with the selection of any particular neutron energy depends on the time-of-flight resolution of the system, the uncertainty in the neutron flight path, as well as on the spread in the mean proton energy in the lithium target. Figure 3.3 shows a Gaussian fit to the gamma peak in the spectrum measured at ADC channel 1864 (see figure 3.1). The FWHM of this peak (1.02 ns) is a measure of the intrinsic time of flight resolution of the system.

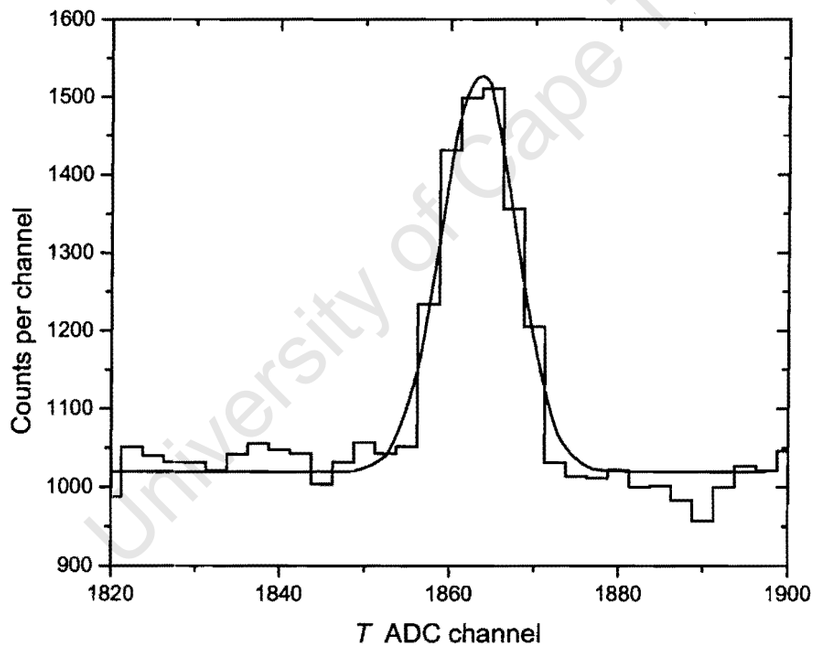

Figure 3.3. A Gaussian fit (solid curve) to the gamma-ray peak centred at T ADC channel 1864 (see figure 3.1). The FWHM of the peak is 8.54 channels, which corresponds to 1.02 ns.

3.2 Particle discrimination

A pulse shape parameter, S, was derived off-line for each event from the L and F parameters by combining them in the form:

$$S = L - kF + C \tag{3.4}$$

where k and C are arbitrary constants which are set in the off-line analysis of the data. The value of k determines the angle of the loci in the L-S distributions (see below) and the value of C sets the position of the data on the S-axis.

The analysis described and the data presented in this chapter are for measurements made by the stacked scintillator spectrometer at 0° for neutrons produced by the ^{7}Li(p,n)^{7}Be reaction for an incident proton beam of energy 99.21 MeV. Data from the other measurements are presented in Chapter 5.

As described earlier in section 1.5, two event types are of particular interest for measurements with the stacked spectrometer. "Single events" are identified by a "stop" from pulse shape discriminator A and no coincident signal in B. "Coincidence events" (A+B) are identified by a "stop" from pulse shape discriminator B and an "escape" from pulse shape discriminator A. Thus the singles events correspond to neutron interactions for which the resulting charged particle (or particles) come to rest in A and the coincidence events are predominantly neutron events in which one or more recoils or charged reaction products escape from A into B.

Figure 3.4 shows a perspective plot of counts (vertical) as a function of pulse shape, S_A, and pulse height, L_A for singles events (detector A only) produced by neutrons of energy 97.1 MeV, selected by the time-of-flight window shown by the dashed lines in figure 3.2. Well-defined ridges, or loci, are resolved on the L-S plane. These loci are attributed to different charged particles released by n–p elastic scattering or by n–^{12}C interactions in the scintillator and are identified in figure 3.4 as follows: protons (p); charged particles (mainly protons) which escape from A and are not vetoed by B (e); deuterons (d); and

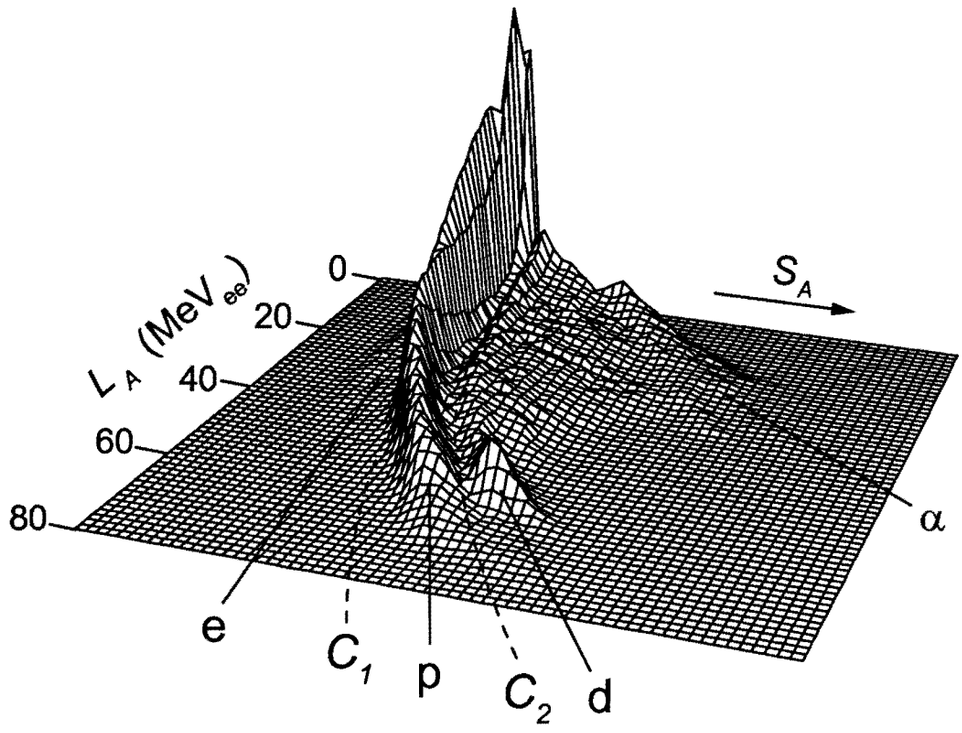

Figure 3.4. Counts (vertical) versus pulse shape S_A and pulse height L_A (in MeV$_{ee}$) for singles events in detector A when irradiated by neutron beam of energy 97.1 MeV. The labels show: loci attributed to escaping protons (e), protons (p), deuterons (d) and alphas (α); and pulse shape discrimination cuts (C_1 and C_2), see text.

α-particles (α). Events in the region between loci *d* and α can be attributed to heavier ions such as tritons, or to the simultaneous detection of two or more charged particles. Software selections of regions of interest were made using the program GNU [GNU]. An L_A-S_A window was set for singles events using cuts C_1 and C_2, as shown, to select events associated with detection of recoiling protons in detector A.

Figure 3.5 shows plots of counts (vertical) versus pulse height and pulse shape obtained (a) from detector A and (b) from detector B, for coincidence events produced by 97.1 MeV neutrons. These distributions show that the coincidence events correspond to protons originating in A which escape (locus *e* in (a)) and are brought to rest in B (locus p in (b)). The pulse shape discrimination cuts C_3 and C_4 shown in figure 3.5(a) were set to distinguish between the "escapes" (protons which escape from the scintillator) and "stops" (protons which come to rest in the scintillator). "Escapes" are identified by $C_3(L) < S(L) < C_4(L)$ and "stops" by $S(L) > C_4(L)$. The proton locus in (b) was selected by the window defined by the cuts C_5 and C_6, as shown.

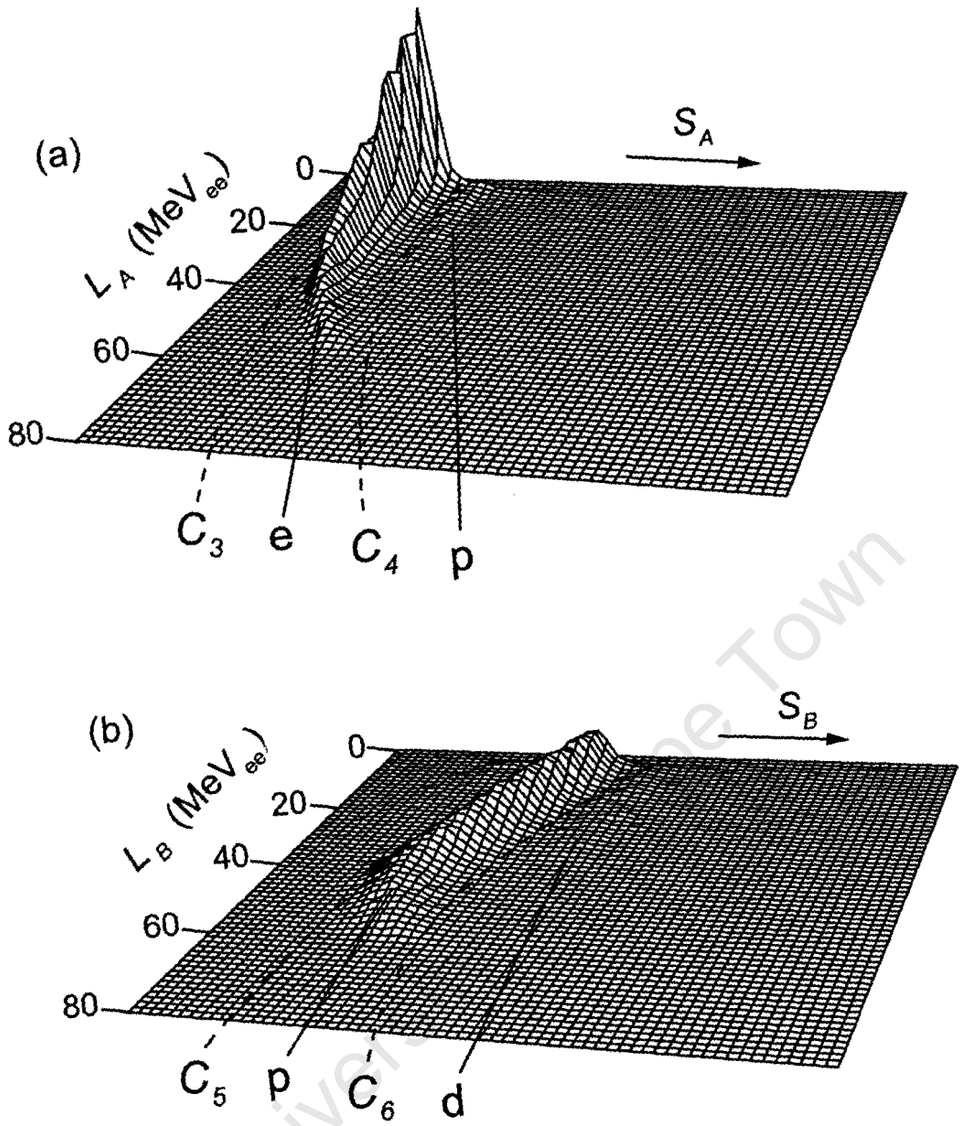

Figure 3.5. Counts (vertical) versus pulse shape S and pulse height L (in MeV_{ee}) from: (a) detector A; and (b) detector B, obtained from coincidences events (A + B) produced by incident neutrons of energy 97.1 MeV. Loci are labelled as in figure 3.4. Cuts C_3, C_4, C_5 and C_6 select protons which escape from detector A and come to rest in detector B.

3.3 Pulse height spectrum at E_n = 97.1 MeV

Two pulse height parameters were recorded for each event during the experiments (see Table 2.3). The L_A and L_B parameters were pulse height signals from the LINKs servicing detectors A and B respectively. These parameters were used for pulse shape discrimination purposes only (see figures 3.4 and 3.5). The other pulse height parameters (D_A and D_B) were derived from the 4th dynodes of the photomultipliers. Since the D pulses were less likely to be subject to non-linearities, such as those related to space charge saturation in the photomultipliers, the D parameters were used for all measurements of response functions.

Events associated with recoiling protons were selected by using cuts C_1 and C_2 for singles events (figure 3.4) and C_3, C_4, C_5 and C_6 for coincidence events (figures 3.5(a) and (b)). The spectrum of pulse heights D_A from detector A, called the "A-spectrum", is determined for singles events, and is shown for the measurement at E_n = 97.1 MeV in figure 3.6(a). It can be seen that the upper pulse height edge is not clearly defined due to the high proportion of protons which escape from the detector, since the range of a 97.1 MeV proton in NE213 is 8.4 cm.

The spectrum of the coincidence pulse heights, called the "AB-spectrum", is determined for coincidence events, and is shown in figure 3.6(b). This is a spectrum of proton events which start in detector A and stop in detector B. The "total spectrum", D shown in figure 3.6(c) is formed by summing the A- and AB-spectra and is the response function measured for 97.1 MeV neutrons, for all recoiling protons which start in detector A. This response function was selected with centre energy of 97.1 MeV (see Table 3.1). The spectrum in figure 3.6(c) is thus minimally affected by proton escape from the spectrometer.

The sharpness of the upper pulse height edge in the spectrum shown in figure 3.6(c) provides a measure of the energy resolution of the stacked spectrometer for neutrons of that particular energy (97.1 MeV). The edge is broadened by photoelectron statistics, the physical characteristics of the scintillator, the gain matching between the left and right photomultipliers of each detector, and by any non-uniformity in the efficiency for the transmission of scintillation light from different regions of the scintillators to the cathodes

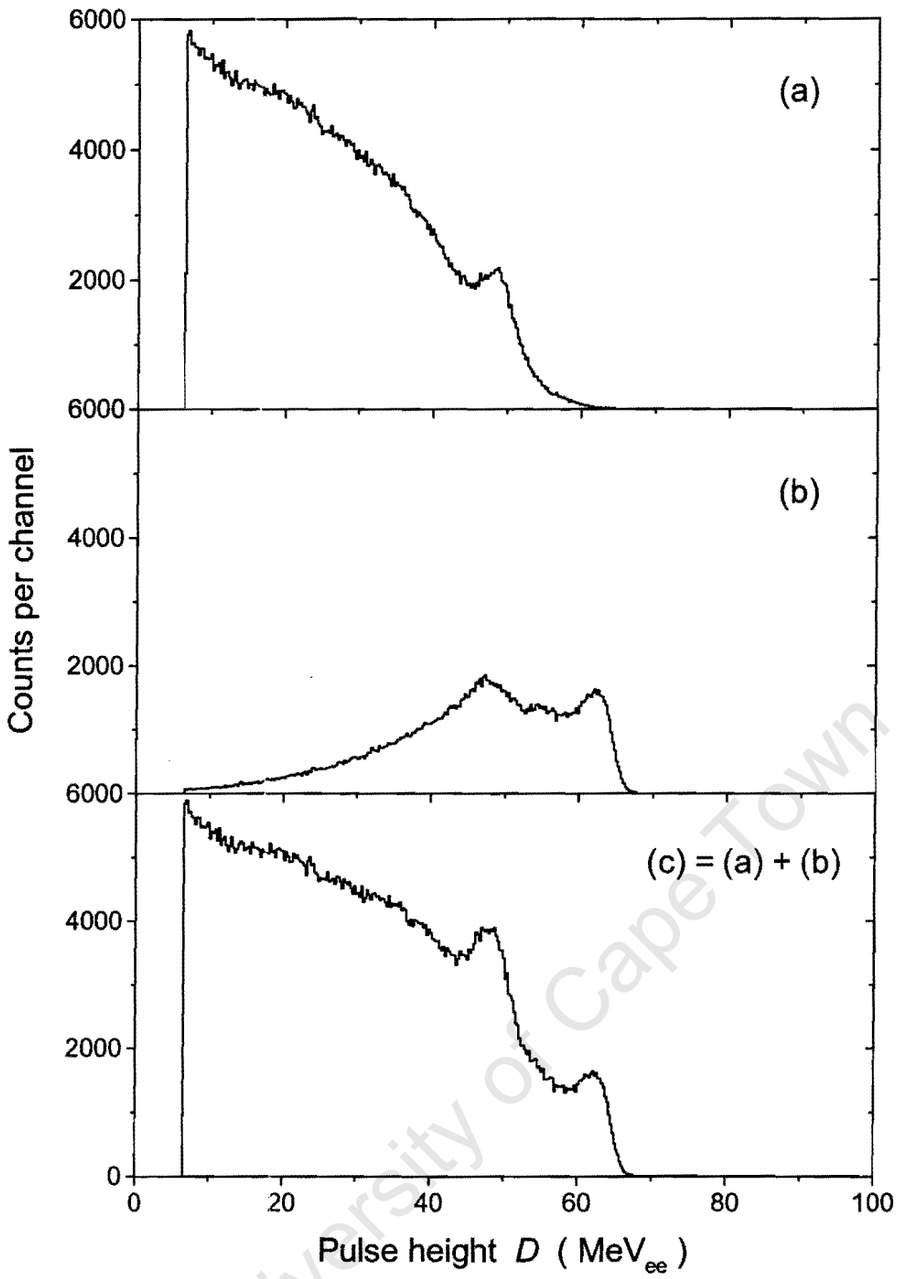

Figure 3.6. Pulse height spectra measured for the stacked scintillator spectrometer for measurements at E_n = 97.1 MeV. Panel (a) shows a spectrum for singles events whereas (b) is for the coincidences. Panel (c), obtained by summing the spectra shown in (a) and (b), shows the response of the spectrometer to incident neutrons of 97.1 MeV.

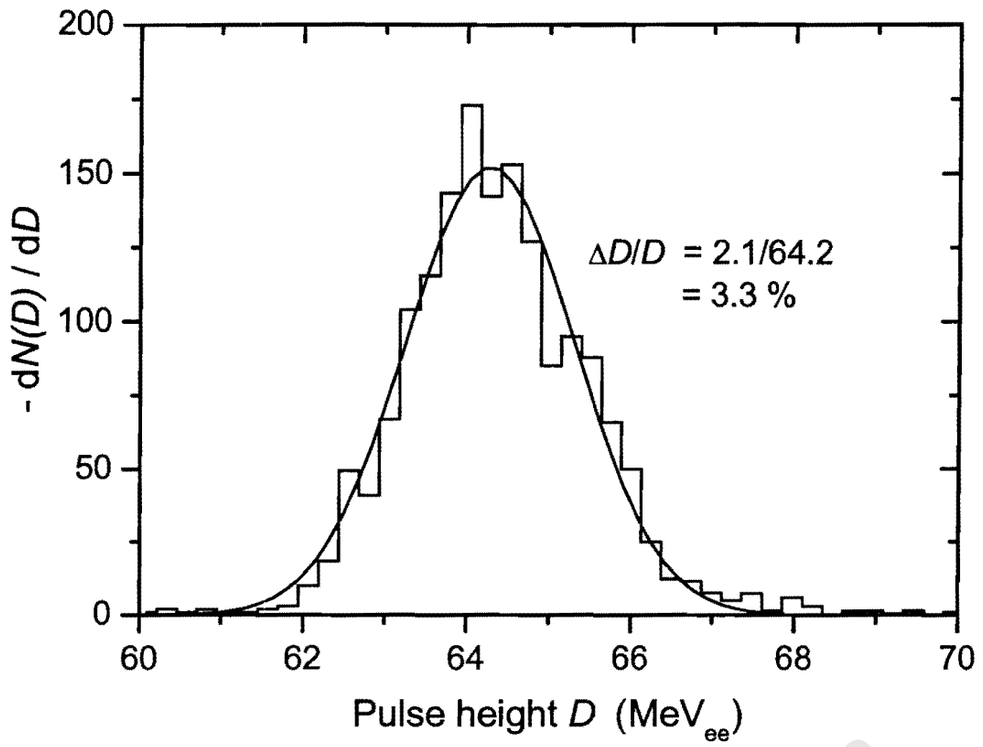

Figure 3.7. –dN(D)/dD obtained by differentiating the pulse height spectrum shown in figure 3.6 (c). The solid curve is a Gaussian fit to the data.

of the photomultipliers. A quantitative measure of the pulse height resolution was obtained by differentiating the spectrum $N(D)$ shown in figure 3.6(c) and plotting $-dN(D)/dD$ versus D (figure 3.7). The edge resolution width, defined as the FWHM of the corresponding peak, was determined to be 3.3% for the stacked spectrometer at this neutron energy.

3.4 Pulse height spectra at other neutron energies

Figure 3.8 shows a perspective plot of counts (vertical) as a function of neutron time of flight parameter, T (in nanoseconds) and pulse height, D_A, for singles events in detector A. The neutron time-of-flight, T, is associated with the energy of the incident neutron while the pulse height, D_A, is related to the energy of the recoiling charged particle in detector A. Sixteen time window numbers used to select the response functions for this work are also labelled. The intense locus within time window number 16 corresponds to neutrons of

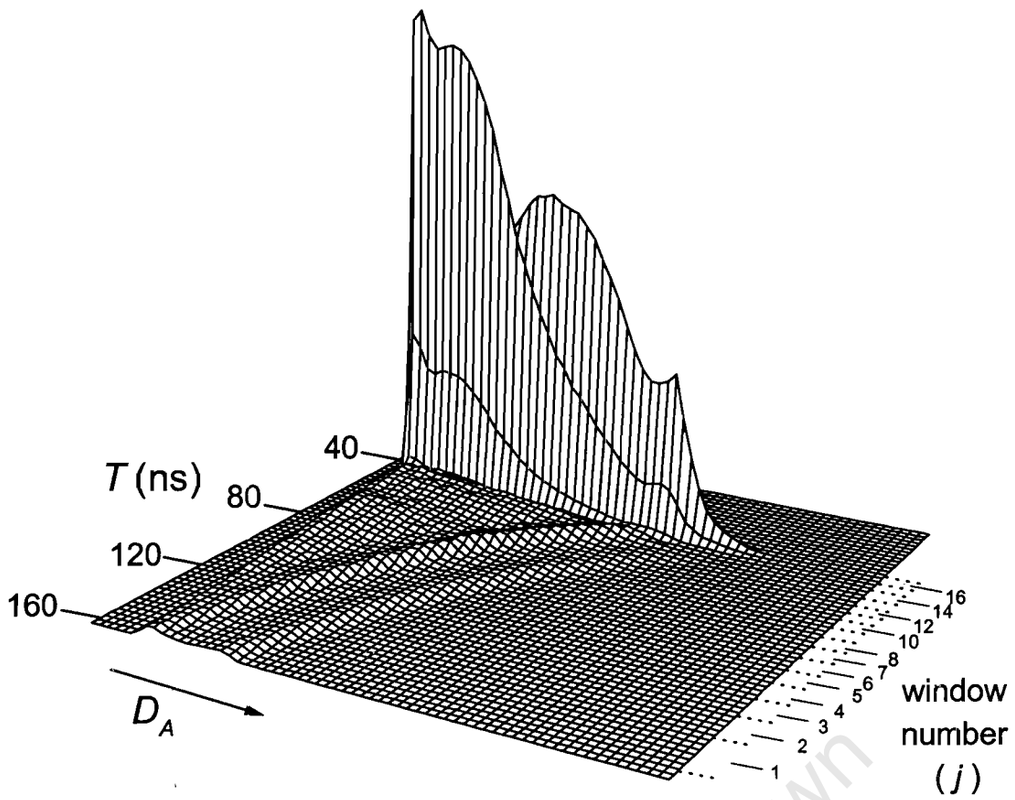

Figure 3.8. Counts (vertical) as a function of neutron time-of-flight (T) and pulse height in detector A (D_A) measured for the neutron beam produced by bombarding a 99.21 MeV pulsed proton beam onto a 3 mm thick natural lithium target. The sixteen time windows referred to in the text are indicated.

E_n = 97.1 MeV and is associated with neutrons produced in the unresolved ground state and 0.429 MeV transition in the ^{7}Li(p,n)^{7}Be reaction (see also figure 3.2). The other significant feature is the curved edge marking the upper pulse height limit for protons recoiling from ^{1}H(n,n)^{1}H events in the scintillator. The second ridge at lower pulse height is associated with the maximum pulse height for charged particles recoiling from n–^{12}C interactions in the scintillator. In order to cover the neutron energy range of 20 – 100 MeV for this work, a set of response functions was constructed similarly to the response function for neutrons of energy E_n = 97.1 MeV, described above. For this work, 16 response functions of equal energy bin width (5 MeV) were chosen (see Table 3.1), with the exception of the 97.1 MeV response function.

The T-channel edges of the bins were calculated using equation 3.1. Table 3.1 displays the lower and the upper time-of-flight channels for each energy bin, and the centre neutron energy values.

Table 3.1: Neutron energies used in the present work.

Bin number j	Centre energy E_n (MeV)	Energy of bin edges (MeV)		T channel of bin edges (ADC channel)	
		Lower	Upper	Lower	Upper
1	20	17.5	22.5	1045	1147
2	25	22.5	27.5	1148	1220
3	30	27.5	32.5	1221	1276
4	35	32.5	37.5	1277	1320
5	40	37.5	42.5	1321	1356
6	45	42.5	47.5	1357	1387
7	50	47.5	52.5	1388	1413
8	55	52.5	57.5	1414	1435
9	60	57.5	62.5	1436	1455
10	65	62.5	67.5	1456	1472
11	70	67.5	72.5	1473	1486
12	75	72.5	77.5	1487	1502
13	80	77.5	82.5	1503	1514
14	85	82.5	87.5	1515	1526
15	90	87.5	92.5	1527	1537
16	97.1 [α]	92.5	102.5	1538	1556

[α] For bin 16, $E_n = 97.1$ MeV corresponds to the peak energy.

The events selected by each *T*-cut were analysed in the same way as described above for the 97.1 MeV response function. The 16 response functions obtained, each of 400 pulse height channels, are shown in figure 3.9. These are plots of counts per bin as a function of pulse height *D*. For the response functions measured for neutron energies above 60 MeV (figure 3.9(b)), two spectra are presented. The dotted lines indicate the spectra for single events and the solid histograms show the full response functions (singles and coincidences). For the summed spectra, the effect of escaping protons has been efficiently dealt with and the upper pulse height edges are well defined. The positions of upper edges of the pulse height spectra in figure 3.9 for the summed spectra (broadened by the detector resolution) increase with neutron energy, as expected. The ADC channel positions of the half-heights of these edges therefore provide an inherent pulse height to proton energy calibration for the spectrometer.

3.5 Proton energy calibration

The position of the upper pulse height edge of each response function in figure 3.9 corresponds to the maximum energy which can be transferred by a neutron to a proton at each energy. The positions of the upper pulse height edges were determined for each response function (see figure 3.9). Figure 3.10 shows a plot of proton energy, E_p (in MeV), as a function of pulse height ADC channel *D* (in ADC channels and MeV_{ee}) obtained from the 16 response functions used in this work. Also shown is a least square linear fit (solid line) to the data which resulted in the following relationship

$$E_p = 0.367\,D + 1.743 \text{ MeV}. \tag{3.5}$$

Although the response of NE213 to protons and other charged particles is not linear and may be described, for example, by the Birks relation (equation 1.1), a straight line is appropriate to use if the lower energy region (less than about 20 MeV) is not included in the fit. Equation 3.5 provides a pulse height calibration for protons in the stacked scintillator spectrometer. It should be noted that the calibration described by equation 3.5 does not include any correction for the energy loss of the protons in the thin walls (0.3 mm tinplate) of detectors A and B, which is calculated [Ji84] to be 1.8 MeV for 100 MeV protons.

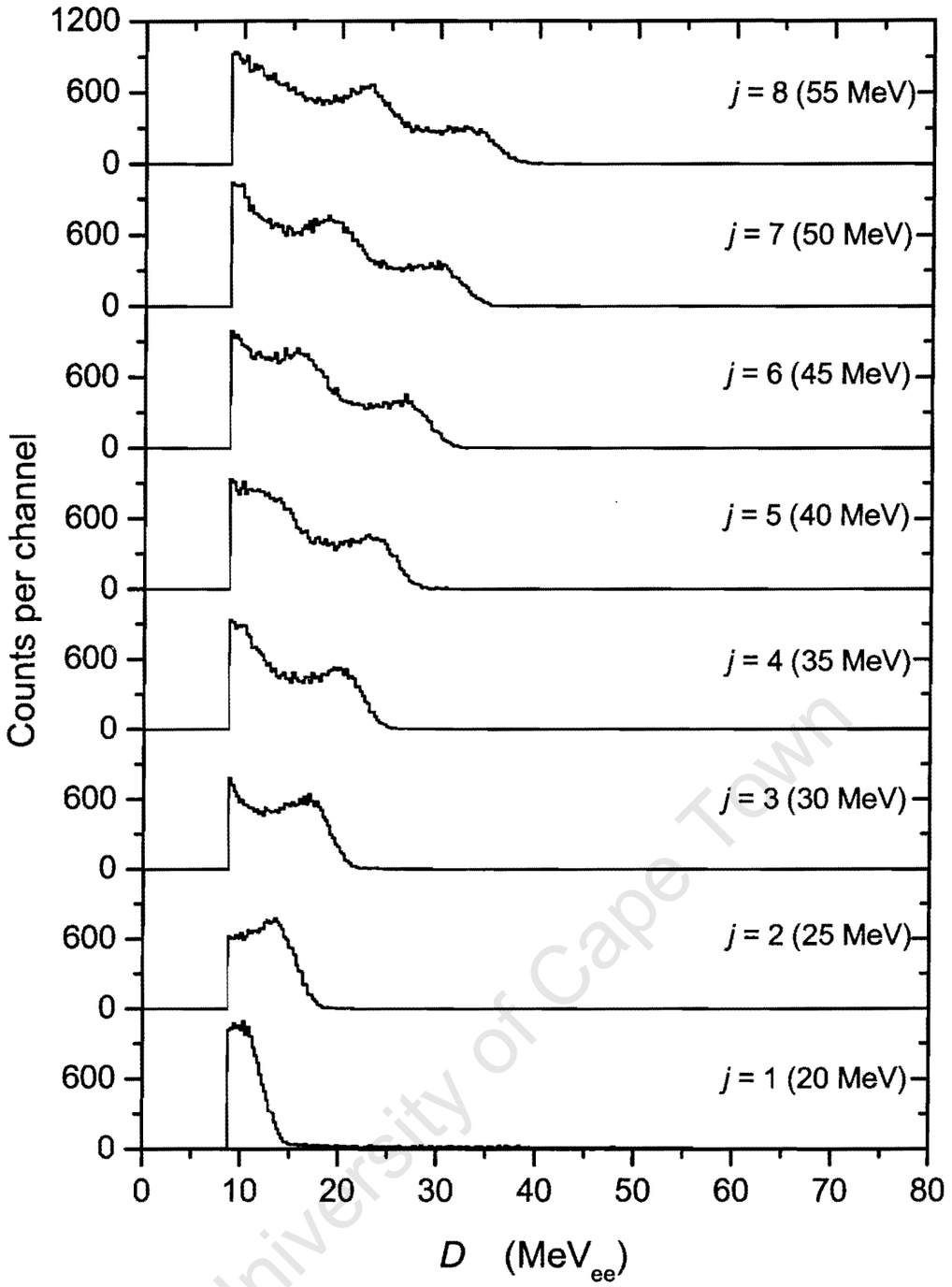

Figure 3.9 (a). Eight of the response functions measured by the stacked spectrometer, for quasi-monoenergetic neutrons of energy 20 MeV, 25 MeV, 30 MeV, 35 MeV, 40 MeV, 45 MeV, 50 MeV and 55 MeV.

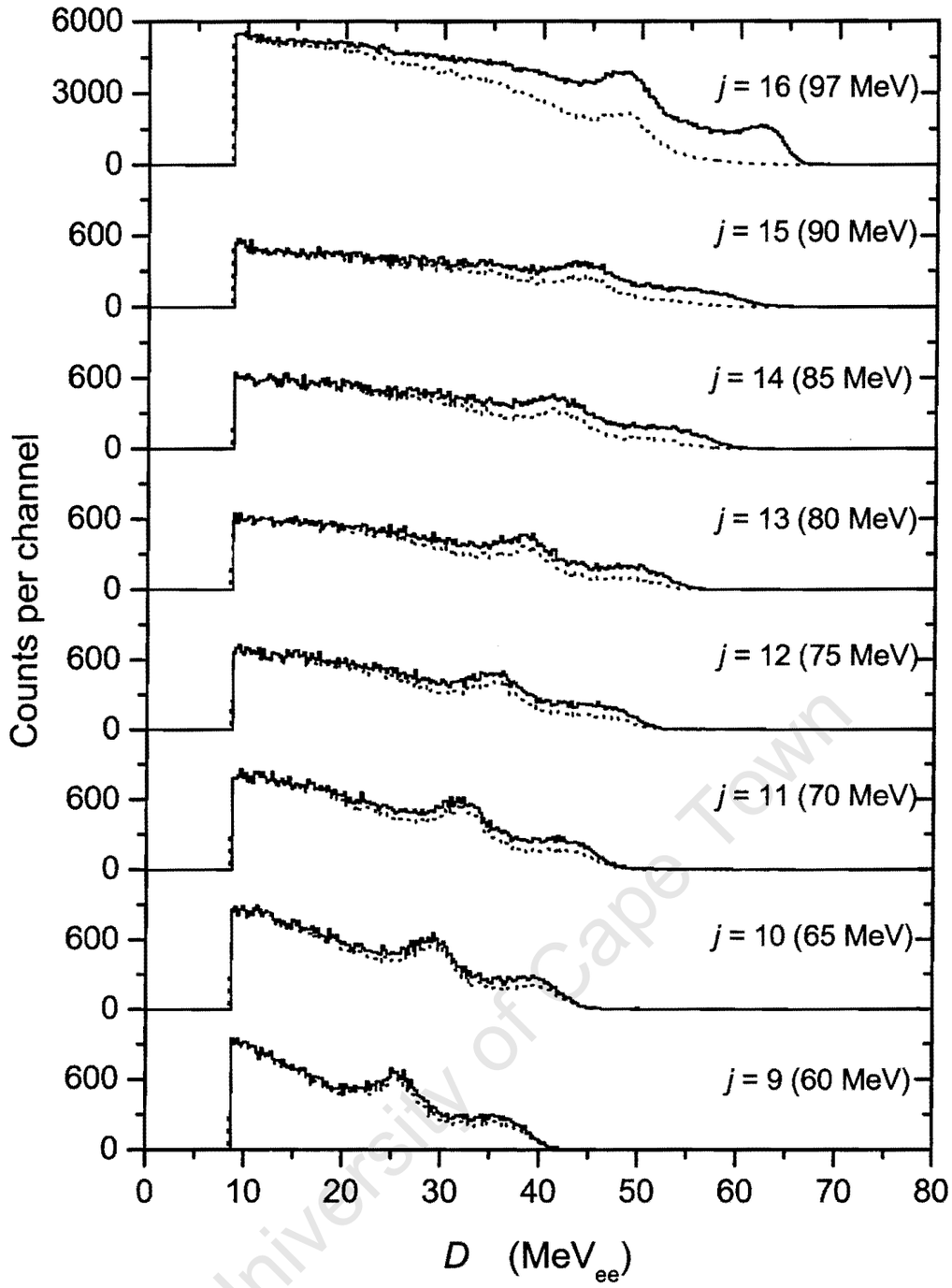

Figure 3.9 (b). Eight of the response functions measured by the stacked spectrometer, for quasi-monoenergetic neutrons of energy 60 MeV, 65 MeV, 70 MeV, 75 MeV, 80 MeV, 85 MeV, 90 MeV and 97.1 MeV. The dashed histograms are the response functions measured by detector A only (singles spectra).

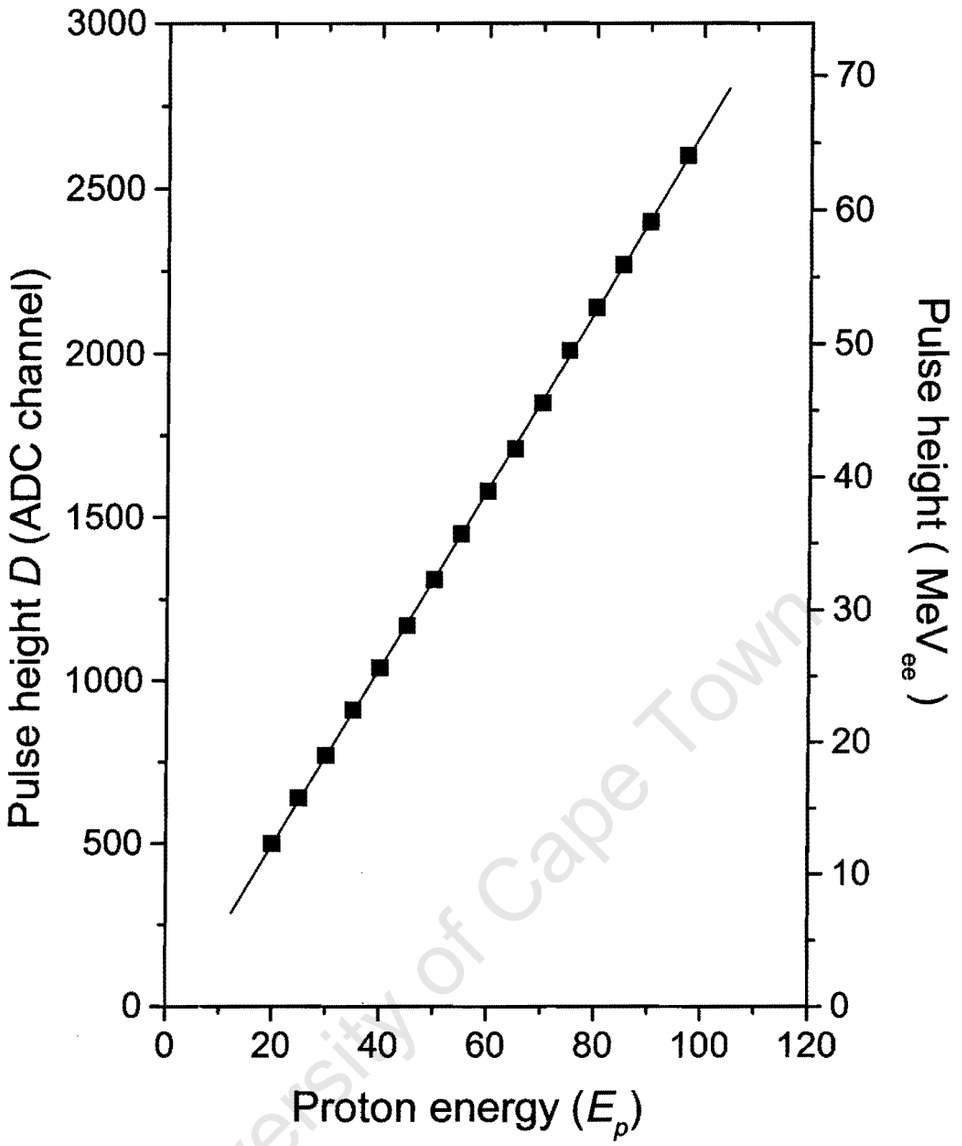

Figure 3.10. Pulse height D (in ADC channel and MeV_{ee}) versus proton energy E_p for the stacked scintillator spectrometer. The solid line is a least square linear fit to the data.

4

Calculation of neutron fluence

4.1 Neutron detection efficiency

The primary component of NE213 liquid scintillator is xylene ($C_6H_4(CH_3)_2$) to which naphthalene ($C_{10}H_8$) is added to reduce quenching effects and to enhance the slow component of the light output. Table 4.1 shows the specifications of NE213 liquid scintillator [NE].

Table 4.1: Some physical characteristics of NE213 [NE].

Density	0.874 g cm^{-3}
Light output	78% to anthracene
H/C atomic ratio	1.211
No. of H atoms per cm^3	4.82×10^{22}
No. of C atoms per cm^3	3.98×10^{22}
Electron density (electrons per cm^3)	2.87×10^{23}
Refractive index at 425 nm	1.530
Wavelength of maximum emission	425 nm

The number of hydrogen atoms per cm^2, n_H, presented to the beam by the scintillator is given by

$$n_H = \frac{N_A \rho d \eta_H}{M} \tag{4.1}$$

where:

N_A : Avogadro's number (= 6.022×10^{23} mol^{-1}) ;

ρ : density of NE213 liquid scintillator (= 0.874 g cm^{-3} [NE]) ;

d : thickness of the detector ;

η_H : number of hydrogen atoms per molecule of NE213 (= 10) ; and

M : molar mass of NE213 (= 106 g mol^{-1}).

Taking the thickness d of the first segment of the stacked spectrometer (detector A) to be 7.0 cm, then from equation 4.1, $n_H = 3.46 \times 10^{23}$ cm^{-2} = 0.346 $barn^{-1}$. Similarly, the number of carbon atoms per cm^2, n_C, presented to the beam by detector A is calculated to be 0.278 $barn^{-1}$.

The neutron detection efficiency of the spectrometer may be determined relative to the well-known n–p elastic scattering cross section. For an NE213 scintillator, the efficiency

for detecting neutrons of a particular energy via n–p elastic scattering only ε_H is given by [Lo76]:

$$\varepsilon_H = \phi_T \frac{n_H \sigma_H}{n_H \sigma_H + n_C \sigma_C} \{1 - e^{-(n_H \sigma_H + n_C \sigma_C)}\} \tag{4.2}$$

where:

n_H: number of hydrogen atoms per unit cross sectional area presented to the beam by the scintillator ;

n_C: number of carbon atoms per unit cross sectional area presented to the beam by the scintillator ;

σ_H: total cross section for n–p elastic scattering ;

σ_C: total cross section for all neutron-induced interactions with ^{12}C in the scintillator

ϕ_T: fraction of neutrons detected above pulse height threshold D_T, where D_T is set so as to select events associated with n–p elastic scattering only (see figure 4.1).

Table 4.2 shows the total cross sections σ_H for n–p elastic scattering and σ_C for n–^{12}C interactions [Ro91] for a range of neutron energies, together with the products $n_H\sigma_H$ and $n_C\sigma_C$ calculated for detector A.

Table 4.2: Total cross sections σ_H for n–p elastic scattering and σ_C for n–C interactions for a range of neutron energies, together with the products $n_H\sigma_H$ and $n_C\sigma_C$ for detector A.

Incident neutron energy (MeV)	σ_H (barn)	$n_H\sigma_H$ for NE213	σ_C (barn)	$n_C\sigma_C$ for NE213
20	0.427	0.149	1.50	0.417
25	0.375	0.131	1.43	0.398
30	0.322	0.112	1.32	0.367
35	0.260	0.090	1.17	0.325
40	0.215	0.075	1.03	0.286
45	0.187	0.065	0.98	0.272
50	0.160	0.056	0.91	0.253
55	0.141	0.049	0.85	0.236
60	0.125	0.044	0.78	0.217
65	0.113	0.039	0.71	0.197
70	0.104	0.036	0.67	0.186
75	0.097	0.034	0.63	0.175
80	0.092	0.032	0.60	0.167
85	0.086	0.030	0.57	0.158
90	0.082	0.029	0.55	0.153
97.1	0.078	0.026	0.51	0.142

It can be seen from Table 4.2 that with increasing incident neutron energy, $(n_H\sigma_H + n_C\sigma_C) << 1$ with the result that equation 4.2 reduces to:

$$\varepsilon_H = \phi_T \frac{n_H\sigma_H}{n_H\sigma_H + n_C\sigma_C}\{1-(1-n_H\sigma_H - n_C\sigma_C)\} \tag{4.3}$$

or

$$\varepsilon_H = \phi_T\, n_H\, \sigma_H . \tag{4.4}$$

4.2 Neutron fluence

Figure 4.1 shows the pulse height spectrum measured for quasi-monoenergetic neutrons of mean energy 97.1 MeV, selected by time-of-flight window, as described in Chapter 3. A pulse height threshold D_T is set in such a way that only events from n–p elastic scattering are selected (shaded region). This threshold, D_T is set at *approximately* 12.6 MeV below the upper pulse height edge, which corresponds to the threshold of the $^{12}C(n,p)^{12}B$ reaction.

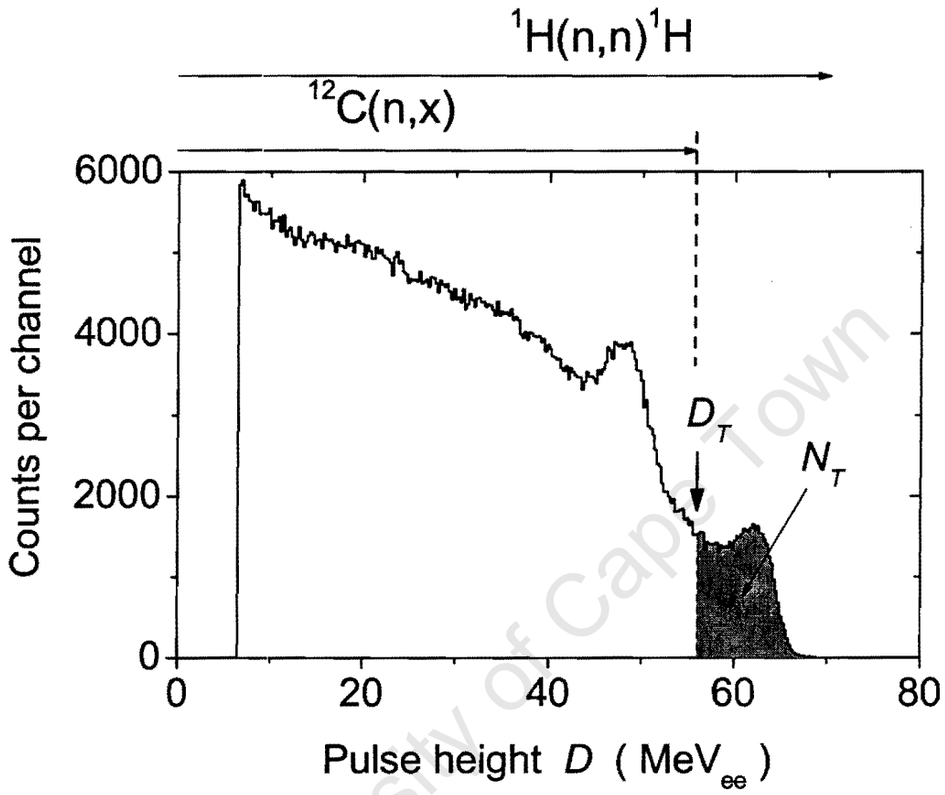

Figure 4.1. Pulse height spectrum measured for quasi-monoenergetic neutrons of energy 97.1 MeV.

The total number of neutrons N_T detected above pulse height threshold D_T is then given by:

$$N_T = N_0 \phi_E \varepsilon_H = N_0 \phi_E \phi_T n_H \sigma_H \tag{4.5}$$

where N_0 is the number of neutrons incident on the detector.

A fraction of recoiling protons which would have had pulse heights above D_T escape from the detector before depositing all of their energy. This causes their pulse heights to fall below D_T, hence the need for an "escape" factor ϕ_E, which is given by

$$\phi_E = (1 - \text{fraction of protons above } D_T \text{ which escape}). \tag{4.6}$$

If the cross-sectional area of the beam is A, then the neutron fluence Φ is given (from equation 4.5) by

$$\Phi = \frac{N_0}{A} = \frac{N_T}{A\phi_E\phi_T n_H \sigma_H} . \tag{4.7}$$

Equation 4.7 may be regarded as the model equation for the fluence measurement. Each input quantity in the equation 4.7 is considered separately below.

(a) N_T: the counts measured above D_T.

The pulse height ADC channel used for D_T in the case of the 97.1 MeV spectrum was 227. When this value was substituted in equation 3.5, the corresponding value for proton energy, E_T, was then found to be 84.9 MeV. The shaded area in figure 4.1 was found to have integral $N_T = 69975$ counts.

(b) ϕ_T : the fraction of n–p elastic scattering events detected above pulse height threshold D_T.

Protons recoiling from n–p elastic scattering events producing pulses in the range $D > D_T$, have energies $E_p > E_T$ and lie within a cone with internal angle ξ in the laboratory frame. This angle is related to the incident neutron energy E_n, and the recoiling proton energy E_p, by:

$$E_p = E_n \cos^2 \xi . \tag{4.8}$$

The angle of the scattered neutron θ in the centre-of-mass frame is given by:

$$\cos\theta = 1 - 2\cos^2 \xi \tag{4.9}$$

or

$$\cos\theta = 1 - 2\frac{E_p}{E_n}. \tag{4.10}$$

Therefore E_T is related to an associated neutron angle θ_T in the centre-of-mass frame by:

$$\cos\theta_T = 1 - 2\frac{E_T}{E_n}. \tag{4.11}$$

The fraction of recoiling protons ϕ_T having energy $E_p > E_T$ (and pulse height $D > D_T$), may then be calculated by:

$$\phi_T = \frac{\int_{\theta_T}^{\pi} \sigma_H(\theta) d\theta}{\int_{0}^{\pi} \sigma_H(\theta) d\theta} \tag{4.12}$$

where $\sigma_H(\theta)$ is the differential cross section for n–p elastic scattering.

Figure 4.2 shows differential cross sections for n–p elastic scattering obtained from the ENDF data sets [Ro91]. Shown are the recommended evaluations as a function of neutron angle of scattering in the centre-of-mass system (cosine theta), and incident neutron energy in the range 10 to 100 MeV.

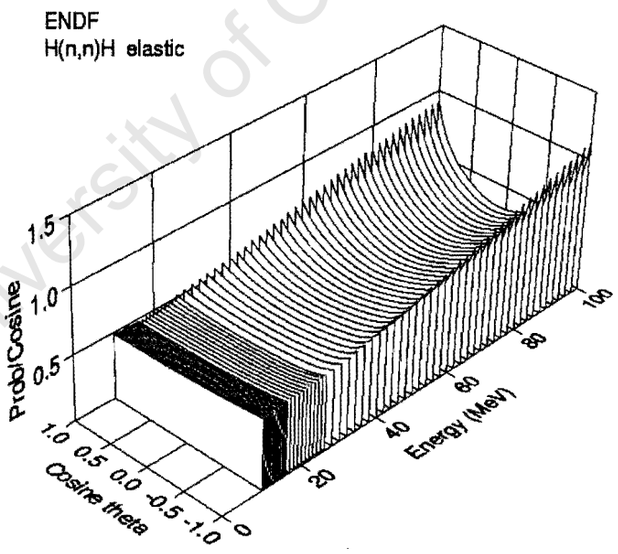

Figure 4.2. Differential cross sections for n-p elastic scattering obtained from the ENDF data [Ro91].

When substituting the value of E_T = 84.9 MeV for the E_n = 97.1 MeV response function in equation 4.11, $\cos\theta_T$ is calculated to be –0.742 and θ_T = 137.9°. Using θ_T = 137.9° and the ENDF data (figure 4.2), the value of ϕ_T is found to be 0.214 from equation 4.12.

(c) ϕ_E : the escaping protons factor.

Figure 4.3 shows the range of protons, deuterons and alpha particles in NE213 scintillator as a function of energy, calculated using the program ELOSS [Ji84]. For a stacked spectrometer having two segments, each of thickness 7.0 cm, the escape correction factor ϕ_E can be calculated as a function of energy. From figure 4.3, the range of 97.1 MeV protons in NE213 is 7.29 cm. The fraction of 97.1 MeV protons which start in the first segment and escape from the second (and are vetoed by detector V, see figure 1.9) is then calculated to be 0.184. Then, from equation 4.6, the value of ϕ_E for this energy is found to be 0.816.

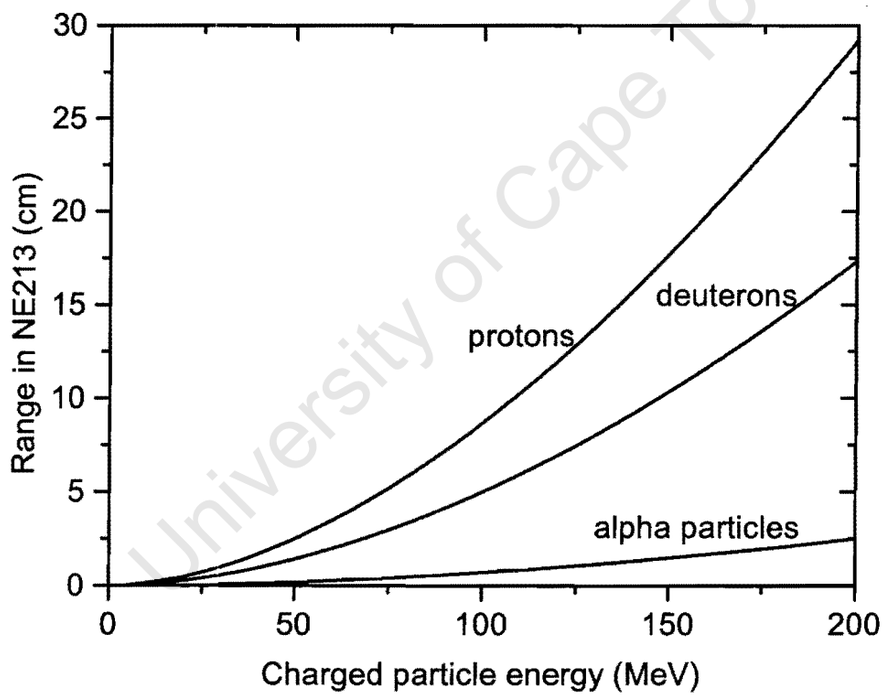

Figure 4.3. Ranges in NE213 liquid scintillator for different charged particles [Ji84].

(d) σ_H : the total cross section for n–p elastic scattering.

From [Mc88], the value of the total cross section, σ_H for elastic scattering at a neutron energy of $E_n = 97.1$ MeV, is 0.078 barns.

(e) n_H : the number of hydrogen atoms per cross sectional area presented to the beam by the scintillator.

From equation 4.1, it has already been shown that $n_H = 0.346$ barn^{-1}.

(f) A : the cross sectional area of the beam.

The beam profile of the beam at position 6.000 m from the target (the position of the centre of detector A) had been previously measured [Bu91]. Figure 4.4 shows the horizontal beam component of the beam profile. The curve in figure 4.4 is a least squares fit to the data of the form

$$y = a + b\exp\left\{-0.5\left(\frac{x-c}{d}\right)^e\right\}. \qquad (4.13)$$

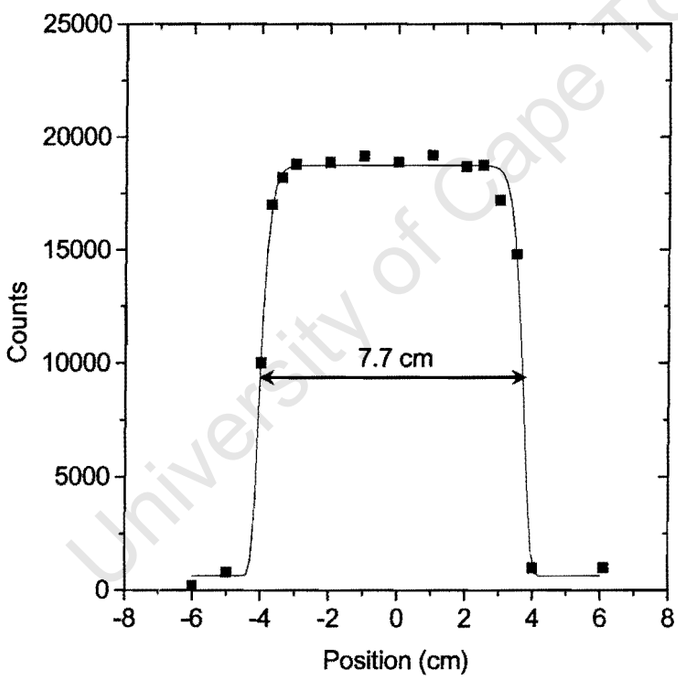

Figure 4.4. Beam profile of the neutron beam measured at a position of a NE213 cylindrical organic crystal of dimensions 1.0 cm (diameter) by 2.1 cm (length) from a horizontal scan in cm [Bu91].

The full width at half maximum of this curve was found to be 7.7 cm and hence the cross section of the beam was taken to be 7.7 × 7.7 cm^2, or 59.29 cm^2. More recent beam profile measurements have been made, although not at 6.00 m from the target. These measurements, however, have been found to be consistent with the profile shown in figure 4.4.

When all the values calculated above are substituted in the model equation 4.7, the neutron fluence Φ at E_n = 97.1 MeV is calculated to be 2.5816 × 10^5 neutrons per cm^2.

4.3 Uncertainty budget for Φ

The uncertainty in Φ arises from the uncertainties of each of the input quantities in equation 4.7. The uncertainty in each of these components may be categorised according to the method used to evaluate them [Le89, Ta94, GUM]. A Type A evaluation of uncertainty is completed by a statistical analysis of values for a repeated series of observations of the same measurand. In this case the standard uncertainty for the measured counts may be taken as the square root of the counts recorded. A Type B evaluation of uncertainty is evaluated by scientific judgement based on all available knowledge about the measurement procedure. If a rectangular probability density function (pdf) is used to model the available knowledge about the measurand, then the standard uncertainty *u(x)* is given by

$$u(x) = \frac{\frac{1}{2}(x_{right} - x_{left})}{\sqrt{3}}, \tag{4.14}$$

and if a triangular probability density function is used, then the standard uncertainty is given by

$$u(x) = \frac{\frac{1}{2}(x_{right} - x_{left})}{\sqrt{6}} \tag{4.15}$$

where x_{left} and x_{right} are the limits of the pdf.

The combined standard uncertainty for Φ is then given by:

$$\left(\frac{u(\Phi)}{\Phi}\right)^2 = \sum_i \left(\frac{u(x_i)}{x_i}\right)^2 \tag{4.16}$$

where x_i and $u(x_i)$ are the best estimates and standard uncertainties respectively for each of the six components in equation 4.7. Table 4.3 presents each factor in equation 4.7, with their best estimates, as calculated above, for incident neutron energy 97.1 MeV. The standard uncertainties are also shown together with the assumed probability density function (pdf) used to estimate them [Le89, Ta94, GUM], with the left (x_{left}) and right (x_{right}) hand values used for each pdf, where appropriate.

Table 4.3: Factors in equation 4.7 and their associated uncertainties for the assumed probability density function (pdf) and uncertainty evaluation used to calculate the neutron fluence and its standard uncertainty for E_n = 97.1 MeV.

Quantity	Best estimate x_i	Standard uncertainty $u(x_i)$	Uncertainty evaluation	pdf used	x_{left}	x_{right}
N_T (counts)	69975	265	Type A	Gaussian	–	–
ϕ_T	0.214	0.009	Type B	Rectangular	0.20	0.23
ϕ_E	0.816	0.033	Type B	Rectangular	0.76	0.87
σ_H (barn)	0.078	0.003	Type B	Rectangular	0.073	0.083
n_H (barn^{-1})	0.346	0.010	Type B	Rectangular	0.329	0.363
A (cm^2)	59.3	2.0	Type B	Triangular	54.39	64.19

It was possible for a fraction of protons that recoiled from detector A into detector B not to be detected since they started too close to the back face of detector A to deposit enough energy and produce a pulse above the threshold of detector A, and therefore not be recorded in N_T. Since each detector (A and B) has a threshold of about 7 MeV_{ee}, this effect was estimated to be of the order of 5-7%.

Table 4.4: Factors used to calculate the neutron fluence for the pulse height spectra shown in figure 3.9.

E_n (MeV)	D_T (channel)	E_T (MeV)	θ_T (°)	ϕ_T	N_T (counts)	ϕ_E	N_0 (counts)
20	15.5	7.4	74.989	0.644	19573	1.000	205536
25	29.1	12.4	89.599	0.524	20336	1.000	298846
30	42.7	17.4	99.265	0.427	20120	1.000	422561
35	56.3	22.4	106.320	0.381	17291	1.000	504042
40	70.0	27.4	111.777	0.336	15091	1.000	603233
45	83.6	32.4	116.168	0.312	13420	1.000	664204
50	97.2	37.4	119.802	0.288	12112	1.000	759012
55	110.8	42.4	122.802	0.274	10213	1.000	763359
60	124.5	47.4	125.820	0.260	9804	1.000	871094
65	138.1	52.4	127.807	0.246	9468	1.000	983535
70	151.7	57.4	129.792	0.240	9108	1.000	1053716
75	165.3	62.4	131.606	0.236	8049	1.000	1015321
80	179.0	67.4	133.236	0.230	7062	1.000	963734
85	192.6	72.4	134.749	0.226	6957	1.000	1033618
90	206.2	77.4	136.054	0.218	6234	0.976	1031791
97.1	226.6	84.9	137.902	0.214	69975	0.816	15306022

From equation 4.16, $u(\Phi)$ is found to be 18.779×10^3 neutrons per cm^2 with the result that the neutron fluence for 97.1 MeV was found to be $(2.58 \pm 0.19) \times 10^5$ neutrons per cm^2. Similar calculations were completed for all the pulse height spectra shown in figure 3.9. Table 4.4 shows the results of the calculated values for the parameters in equation 4.7 in order to calculate the detection efficiency and neutron fluence. The detection efficiency and neutron fluence calculations using these parameters are shown in Table 4.5 with their standard uncertainties for each energy bin.

Table 4.5: Values calculated (equations 4.4 and 4.7) for the detection efficiency and neutron fluence with their associated uncertainties for each energy bin number.

Energy bin number j	ε_H ($\times 10^{-3}$)	$u(\varepsilon_H)$ ($\times 10^{-3}$)	Φ ($\times 10^3$ neutrons / cm^2)	$u(\Phi)$ ($\times 10^3$ neutrons / cm^2)
1	95.2	6.0	3.45	0.25
2	68.1	4.3	5.04	0.36
3	47.6	3.3	7.13	0.55
4	34.3	2.2	8.50	0.63
5	25.0	1.6	10.17	0.75
6	20.2	1.4	11.20	0.85
7	16.0	1.0	12.80	0.95
8	13.4	0.8	12.88	0.92
9	11.3	0.7	14.69	1.06
10	9.6	0.6	16.59	1.22
11	8.6	0.6	17.77	1.32
12	7.9	0.5	17.13	1.26
13	7.3	0.5	16.26	1.20
14	6.8	0.4	17.43	1.28
15	6.2	0.4	17.40	1.28
16	5.6	0.4	258	19

The neutron fluence measurements from Table 4.5 are plotted with their uncertainties as a function of energy bin number in figure 4.5. The neutron fluence measurement and its uncertainty for energy bin 16 were reduced by a factor of 10 for presentation purposes only as indicated in the diagram. It can be seen that this plot resembles the neutron time-of-flight spectrum shown in figure 3.2.

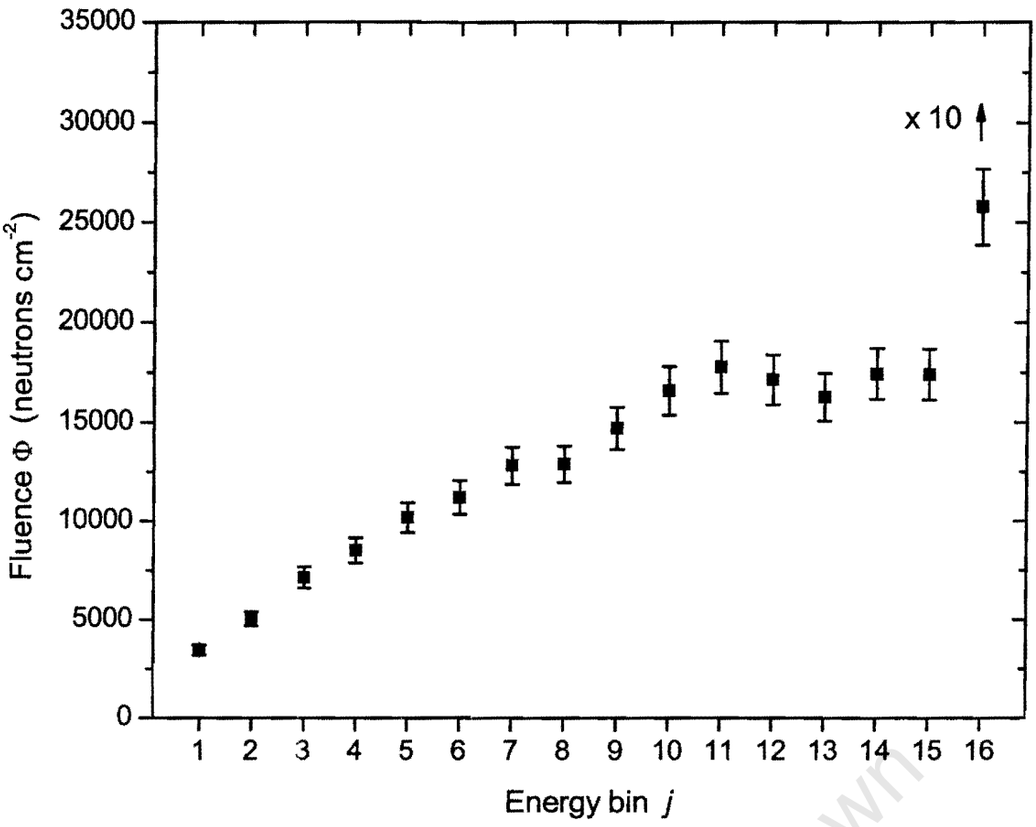

Figure 4.5. Neutron fluence measurements, with their uncertainties, as a function of energy bin number for the stacked scintillator spectrometer. The measurement for bin 16 (97.1 MeV) has been reduced by a factor of 10.

It should be noted that there was no dead time monitoring included in the electronics set-up in this run. This was unusual, since all of the set-up for other run series for this project include a set of two scalers which monitor the live time of the electronics and acquisition system. The dead time of the electronics and acquisition system results in a smaller fluence being measured. In other runs series, the correction for the dead time of the system was typically between 10% to 20%, which means that the scale in figure 4.5 cannot be regarded as an absolute fluence measurement since the correction for dead time was not included.

5

Measurements of neutron spectral fluence

5.1 Particle spectrum unfolding

The unfolding or deconvolution of measured multichannel distributions mainly developed in two application areas: the determination of the energy spectra recorded by recoil detectors with fast neutrons, and the selection of the peaks present in spectra recorded by γ-ray spectrometers. The pulse height spectrum that is recorded from any radiation detector is the convolution of its inherent response function and the energy distribution of the incident radiation. If the purpose of making the pulse height measurements is to obtain information about the energy spectrum of the incident radiation, as is the present case, then this process involves solving the basic system of linear integral equations [We89]

$$z_i = \int_0^\infty R_i(E)\,\phi(E)\,dE \qquad \text{for } i = 1 \text{ to } m \tag{5.1}$$

which represent a model of the measurement. The z_i denote the input measurands which are the data given in terms of the recorded pulse height spectrum. The $R_i(E)$ are the response functions of the measuring system which include the effects of limited energy resolution of the spectrometer. The spectrum parameters $\phi(E)$ are the average fluence values in the intervals between the energies E_i and E_{i+1}. The subscript i is related to the channel number of the measuring system having m channels in total.

Equation 5.1 may be transformed in a variety of ways [Pu93, We89, We95] into the discretised matrix equation

$$z = R\,\Phi. \tag{5.2}$$

Equation 5.2 represents a system of linear equations which must be solved for the column matrix $\Phi = (\phi_1 \ldots \phi_n)^T$ where the superscript T indicates transposition. Data values are assumed to be given for both the column matrix $z = (z_1 \ldots z_m)^T$ of the measured pulse height spectrum and the response matrix $R = R_{ij}$ ($i = 1 \ldots m$; $j = 1 \ldots n$). The matrix elements z_i , ϕ_j and R_{ij} are always non-negative otherwise they would not have any physical meaning. The response matrix R is assumed to be known with negligible uncertainty, however, the column matrix z usually possesses a statistical uncertainty that is expressed by the covariance matrix S_z. If z is a measured pulse height (multichannel) spectrum, then S_z is diagonal, with elements assuming independent Poisson distributions of the event frequencies. The statistical uncertainties in the measured pulse height spectra will propagate through the unfolding calculation and give rise to corresponding variances in the calculated energy spectrum.

There are a number of ways of finding the solution to equation 5.2. Direct inversion [Pr96] may be used, either by derivative methods [Cr87], but physically consistent solutions are not always possible and usually smoothing of the measurement is necessary. Least squares adjustment [Ro80, Ro85] provides an alternative method by seeking a minimum in the weighted sum of residuals χ^2 where [Be69]

$$\chi^2 = \sum_i W_i \left(z_i - \sum_j R_{ij} \phi_j \right)^2 \tag{5.3}$$

and the weighting factors W_i are often chosen to be inversely proportional to statistical variance of each data point. There exist many unfolding algorithms based on the least squares method which have been realized in codes such as LOUHI [Ro80], STAY'SL [Pe77], SAND-II [Mc67] and FERDOR [Bu65]. Although the least squares approach is very powerful, there are a number of inherent difficulties [Ma97]. For example, in order to produce consistent solution spectra, many of these codes require some prior, or *a priori*, information, for example in the form of a pre-calculated fluence vector Φ_0 with an uncertainty matrix $S_{\Phi 0}$. However, if $S_{\Phi 0}$ contains large uncertainty components, non-physical results such as negative elements of the solution vector may result. Furthermore, many established least squares codes have evolved from algorithms which were written before the availability of cheap, fast computers, with the result that uncertainties are often handled in a cumbersome or non-transparent way.

With the advent of modern computing, alternatives to least squares deconvolution have become a viable option. These include Monte Carlo methods [Ma85, We95, Ma97], Maximum Entropy methods [Vo95, Re99, Re02] and approaches based on the use of neural networks [Ko93] and genetic algorithms [Fr99]. In this work, an unfolding code based on a Monte Carlo method was used.

5.2 The MIEKE Monte Carlo code

Bayesian probability theory [Ja90, Sk89] provides a general and consistent framework for logical inference and has been applied successfully in various data analysis problems that are statistical in nature, for example the deconvolution of PIXE and RBS spectra [Fi98, Pr98]. Although the Bayesian formalism is well-grounded theoretically [Sk91], the generality of the technique causes relatively simple problems to become mathematically demanding to solve analytically. This difficulty can be overcome in the context of spectrum unfolding by making realistic approximations and assumptions and applying a Monte Carlo method in which not the most probable fluence (minimum χ^2), but its expectation value from a certain probability distribution is evaluated. It is then possible to

construct an *a posteriori* probability density of the fluence using Bayes' theorem [Je67, Ja90]. The solution spectrum is then defined as the expectation value of Φ which can be calculated from this probability density. Here the term "a posteriori" characterizes the knowledge level after each step or cycle of the unfolding calculation.

The MIEKE Monte Carlo code [Ma85, We95], part of the HEPRO spectrum unfolding package † [Ma94, Ma97], was chosen for the present studies. The algorithm in the MIEKE code is based on simple probability arguments [Ti88, Ti93] and requires a probability distribution [We89] for randomly selecting spectra. The code averages over a large number of possible non-negative solution spectra for $\Phi(E)$. A probability density for $\Phi(E)$ is constructed [We87, We89] of the form

$$P(\Phi) = C_0 \exp\left(-\frac{\beta}{2}\chi^2(\Phi)\right) \quad \text{for all } \Phi_i \geq 0$$

$$P(\Phi) = 0 \qquad \text{for } \Phi_i = 0 \tag{5.4}$$

where C_0 is a normalization constant to be determined from the constraint that

$$\int P(\Phi)\mathrm{d}\phi_1 \ldots \mathrm{d}\phi_n \;=\; 1. \tag{5.5}$$

The MIEKE code makes use of the probability density of equation 5.4 and a Monte Carlo importance sampling algorithm is used to calculate expectation values. The basic idea used to approximate the expectation values is to average over a set of Φ vectors taken from near the region of maximum probability [Wo68]. The computing algorithm consists of performing a sampling random walk in the n-dimensional space spanned by the n axes of Φ, and then certain Markov-chain probabilities [Wo68] are used to produce successive sets of fluence vectors in each iteration. Uncertainties estimated by the code are associated with the statistics of the measured pulse height spectrum only (Type A evaluation) [Ma02].

† Available from Physikalisch-Technische Bundesanstalt (PTB), Bundesallee 100, Braunschweig, Germany. The package includes unfolding codes based on a variety of algorithms as well as tools for spectrum adjustment such as Gaussian broadening and spectrum refolding.

5.3 The response matrix

The neutron fluence was calculated, as described in chapter 4, for each response function shown in figure 3.9, using the total cross section for n–p elastic scattering as an absolute reference. This allows each response function to be normalized to the same number of neutrons incident on the detector. For this purpose, a fluence value of 1 neutron cm^{-2} was chosen. For each neutron energy bin j, since N_T (see figure 4.1) is directly proportional to the neutron fluence Φ, then

$$\frac{N_T(meas)}{N_T(norm)} = \frac{\Phi(meas)}{\Phi(norm)} \tag{5.6}$$

where:

$N_T(meas)$:	integral measured above threshold L_T
$\Phi(meas)$:	measured neutron fluence
$N_T(norm)$:	normalized value of N_T
$\Phi(norm)$:	1 neutron cm^{-2} .

The normalization factor φ for each pulse height spectrum j is then given by

$$\varphi = \frac{1 \ neutron \ cm^{-2}}{\Phi \ (meas)}. \tag{5.7}$$

Table 5.1 lists the measured fluences, Φ (*meas*) and the normalization factors φ for each of the $j = 1$ to 16 energy bins.

The normalized response functions (histograms) using the stacked scintillator spectrometer for quasi-monoenergetic neutrons, selected by time-of-flight are shown in figure 5.1, which together form the response matrix R_{ij} (i = 1 ... 400 ; j = 1 ... 16) for the subsequent unfolding analyses. These were then smoothed (smooth lines) using a moving point polynomial method [Sa64]. Each response function has been normalized to a fluence of 1 neutron cm^{-2}.

Table 5.1: Measured fluences Φ (meas) and normalization factors φ for each of the j = 1 to 16 energy bins.

Energy bin number j	Φ (*meas*) (neutrons cm^{-2})	φ
1	3467	2.884×10^{-4}
2	5040	1.984×10^{-4}
3	7127	1.403×10^{-4}
4	8501	1.176×10^{-4}
5	10174	9.829×10^{-5}
6	11203	8.926×10^{-5}
7	12802	7.811×10^{-5}
8	12875	7.767×10^{-5}
9	14692	6.806×10^{-5}
10	16589	6.028×10^{-5}
11	17772	5.627×10^{-5}
12	17125	5.839×10^{-5}
13	16255	6.152×10^{-5}
14	17433	5.736×10^{-5}
15	17402	5.746×10^{-5}
16	258155	3.868×10^{-6}

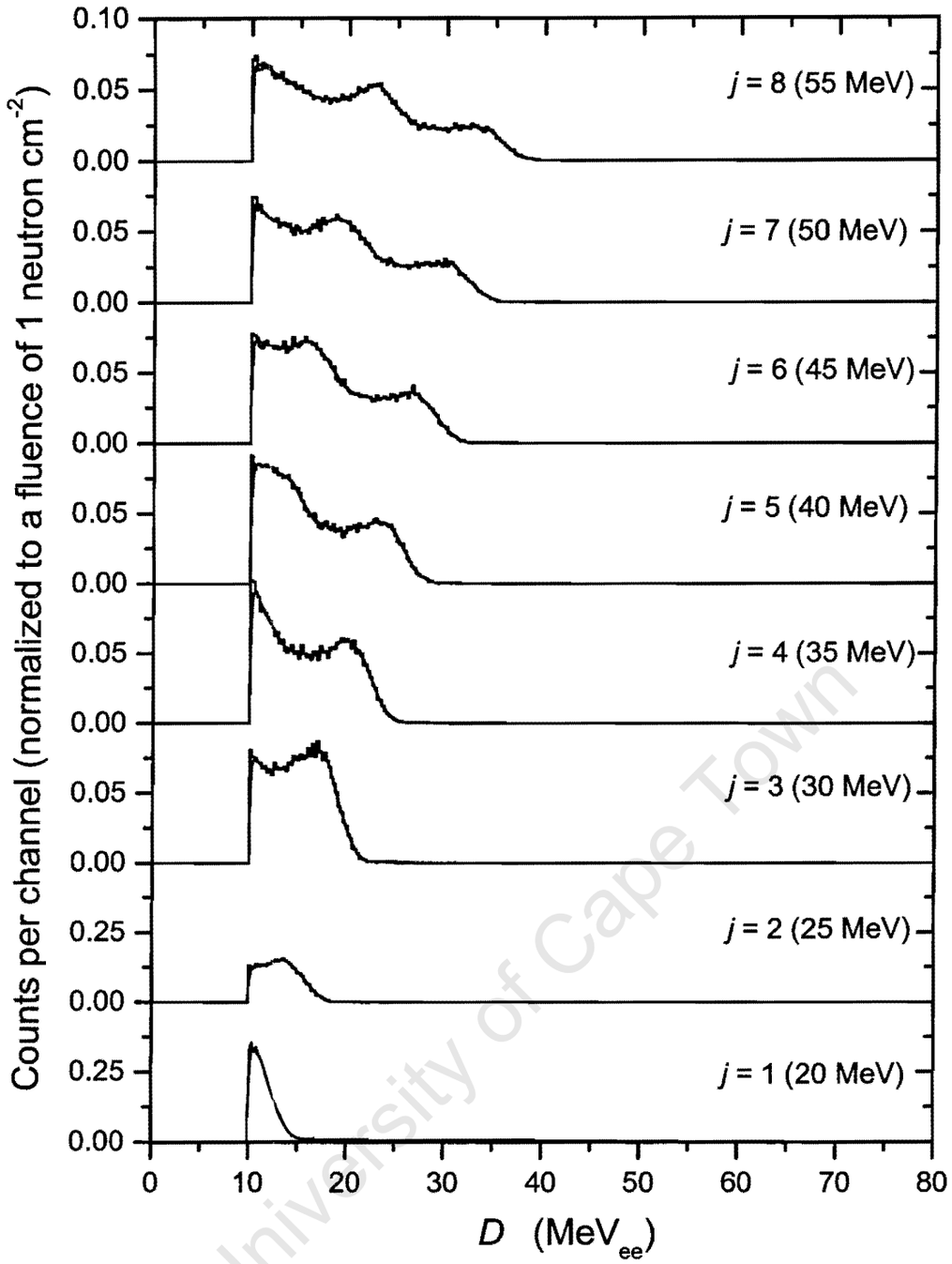

Figure 5.1. (This page and the next) Response functions (j = 1 to 16) measured (histograms) using the stacked scintillator spectrometer for quasi-monoenergetic neutrons selected by time-of-flight. Each response function has been normalized to a fluence of 1 neutron cm^{-2}. Also shown are the spectra after smoothing using a Savitzky-Golay algorithm [Sa64].

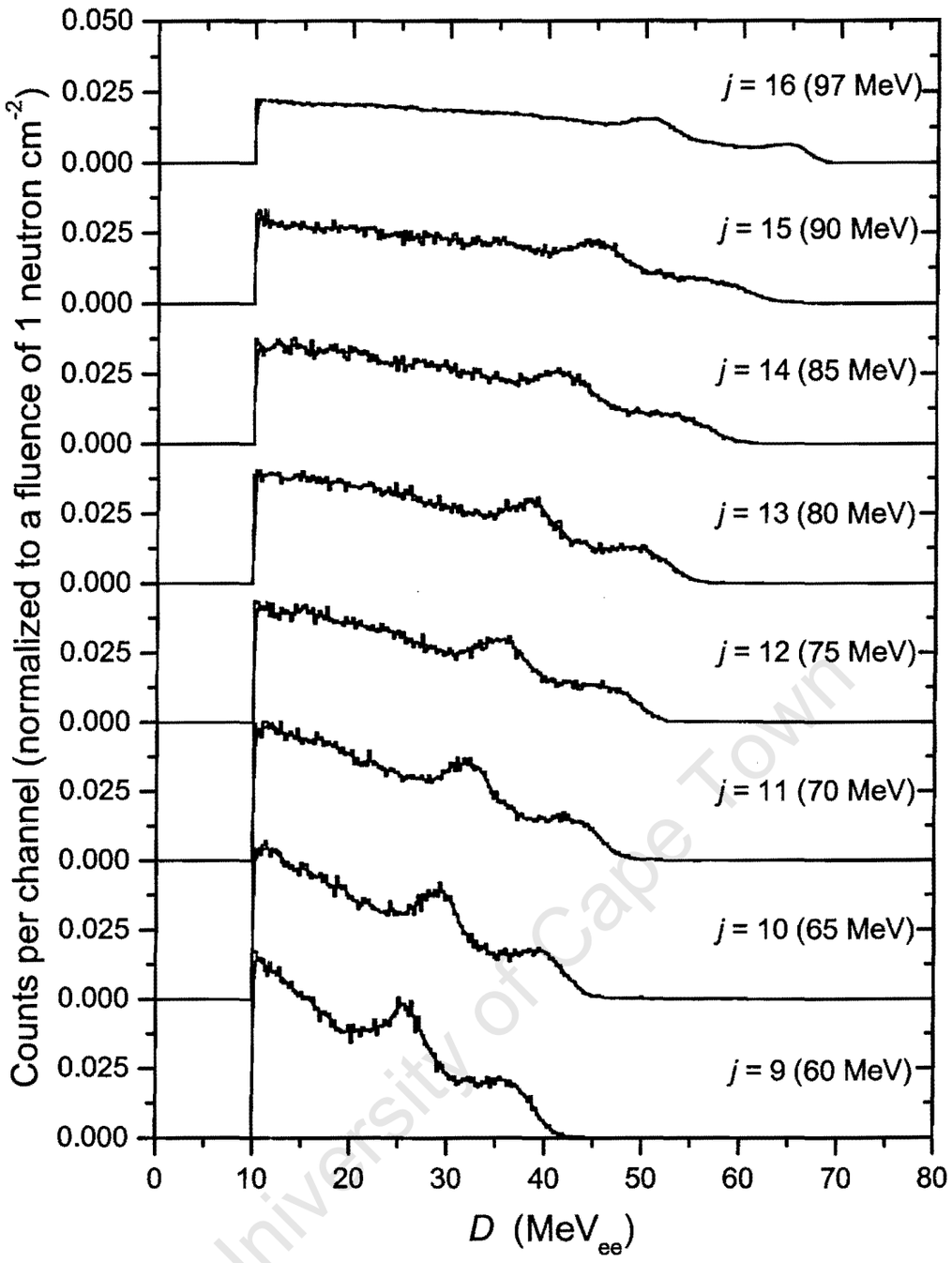

Figure 5.1. (continued).

5.4 Tests of the unfolding procedure

In order to test the reliability of the unfolding process, "known" pulse height spectra were analysed. Four pulse height spectra, namely G_1, G_2, G_3 and G_4 were constructed by summing different subsets of the measured response functions $j = 1–16$. Table 5.2 lists the energy bin combinations for each pulse height combination G_1, G_2, G_3 and G_4.

Table 5.2: Combinations of pulse height groups used to construct pulse height spectra G_1, G_2, G_3 and G_4.

Pulse height spectrum	Energy bin combination j
G_1	1 – 3, 14 – 16
G_2	4 – 13
G_3	4 – 9, 14 – 16
G_4	1 – 13

Each of the four pulse height spectra G_1, G_2, G_3 and G_4 were unfolded using the MIEKE code and the smoothed response functions (figure 5.1), and the results are shown in figures 5.2 and 5.3. Figure 5.2(a)-(d) shows the measured pulse height spectra (histograms) and the refolded MIEKE fits (smooth lines), which appear to be in good agreement. Table 5.3 lists the chi-squared per degrees of freedom values, χ^2/dof, for each of the four unfolding analyses. Figure 5.3(a)-(d) shows the corresponding spectral fluence $\Phi(E)$ measured by the MIEKE analyses. The dashed lines indicate the expected values for the fluence of either zero or unity, whereas the values measured by the unfolding analyses are shown by the solid squares with their standard uncertainties.

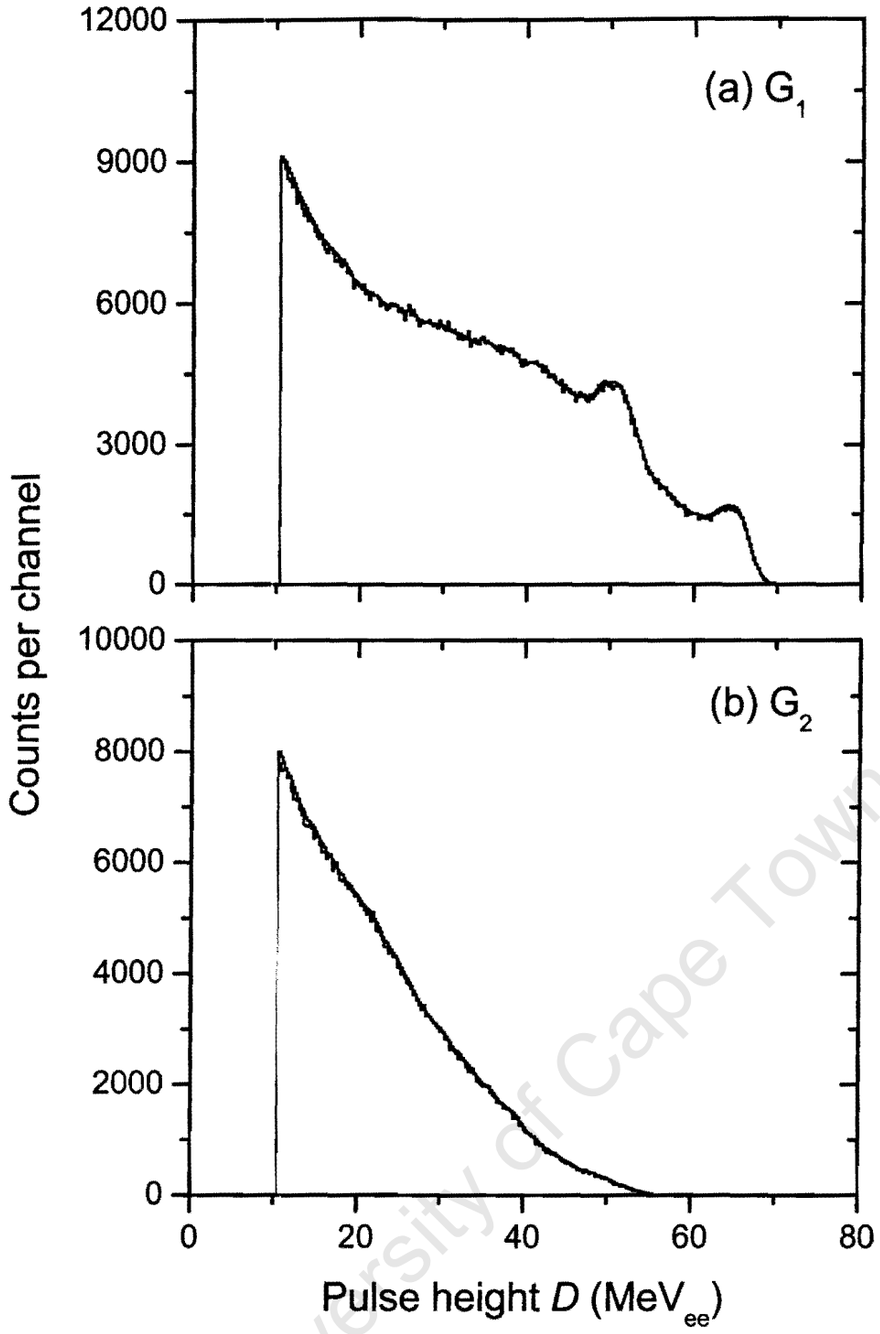

Figure 5.2. (This page and the next) Measured pulse height spectra, (a) G_1, (b) G_2, (c) G_3 and (d) G_4 (histograms) derived from combinations of the energy groups j = 1 to 16 (see Table 3.1) together with the refolded fits (solid lines) resulting from the MIEKE analyses.

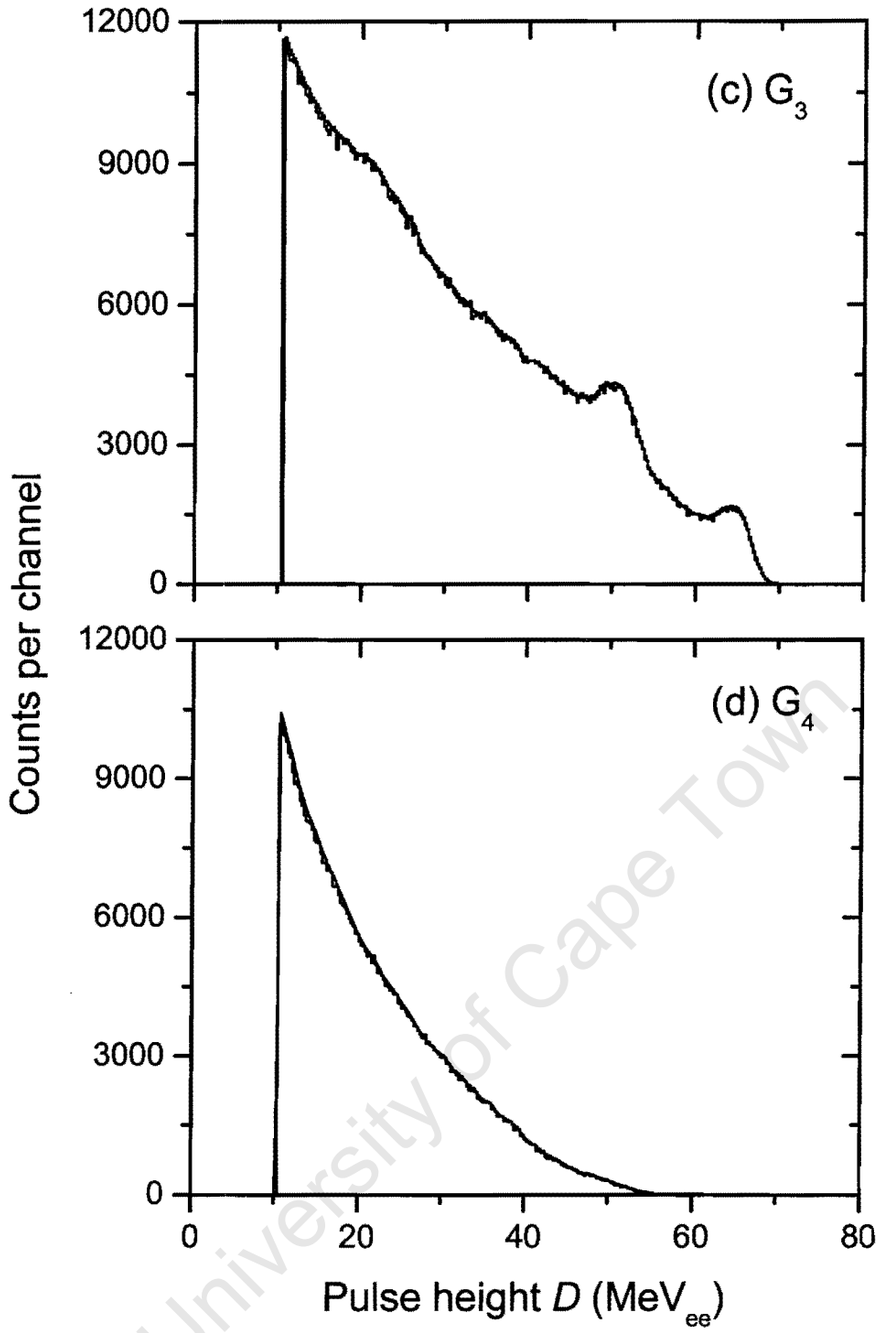

Figure 5.2. (continued).

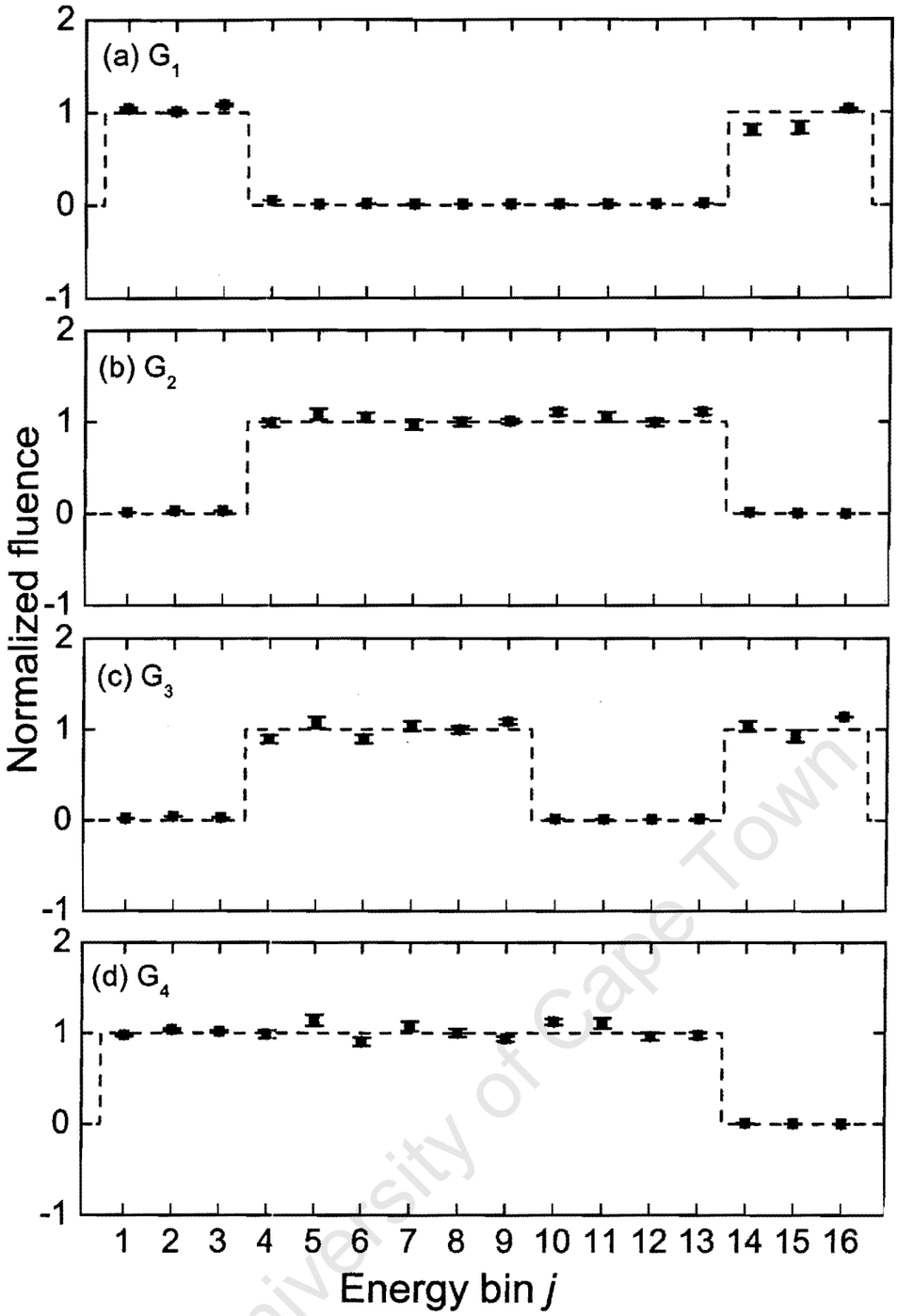

Figure 5.3. Fluence expected (dotted lines) and measured by MIEKE analyses (solid squares) for the pulse height spectra (a) G_1, (b) G_2, (c) G_3 and (d) G_4.

Although the measured and expected values are in good agreement, the results in figure 5.3 show some fluctuations. These are particularly evident in panel (a) for j = 14 and 15 and for panel (b) at j = 10 and 13 as an overestimation, for panel (c) at j = 4 and 6 as an underestimation, and at j = 16 as an overestimation. In panel (d), overestimations are evident at j = 5, 10 and 11 and an underestimation at j = 6. These fluctuations might be a result of uncertainties in the fluence calculations used to normalize the response functions (figure 5.1) or from imperfect smoothing of the response functions. The chi-squared per degrees of freedom values in Table 5.3 suggest good agreement between the measured data with the best fits. From the results in Table 5.3 and figure 5.3 for these tests performed above, it was concluded that with the use of the normalized and smoothed response matrix, the MIEKE code would be reliable for unfolding "unknown" pulse height spectra.

Table 5.3: The chi-squared per degrees of freedom values from the MIEKE unfolding analyses for the spectra $G_1 - G_4$.

Pulse height spectrum	χ^2/dof
G_1	0.821
G_2	0.586
G_3	0.602
G_4	1.776

5.5 Measurements with other targets and other angles

Measurements were also made with the stacked spectrometer using different targets and at different angles (see Section 2.6 and Table 5.4). These runs were analysed in exactly the same way as described for the measurements made using the 3 mm lithium target at 0°. Figure 5.4 shows the neutron time-of-flight spectra measured for (a) the 3 mm Li target at 0°, (b) the 5 mm Li target at 0°, (c) the 10 mm C target at 0°, (d) the 3 mm Li at 16° and (e) the 5 mm Li target at 16°. The dashed lines show the time-of-flight window used to select the same energy range covered by the response matrix, which was based on spectrum (a).

Table 5.4: Details of other pulse height spectra.

Pulse height spectrum	Target and thickness	Angle (°)	*T* window edges (ADC channel)	
			Lower	Higher
H_1	Li (5 mm)	0	1045	1556
H_2	Graphite (10 mm)	0	1045	1556
H_3	Li (3 mm)	16	1045	1556
H_4	Li (5 mm)	16	1045	1556

It is of interest to note that measurements made at both 0° and 16° will result in a "difference" spectrum which is characterised by quasi-monoenergetic peak at 0° and very little contribution in the low energy tail [No02]. Figure 5.5 shows the measurements made with the 3 mm and 5 mm lithium targets at 0° (solid histograms) and 16° (dashed histograms) where the 16° measurements have been normalized to the 0° measurements at *T*-channel 1520. This feature of the time-of-flight spectra is presently being exploited in experiments [Si01, Si02] aimed at measuring cross sections for neutron-induced reactions on nuclides which have importance in cosmic ray physics.

The four pulse height spectra H_1 – H_4 (see Table 5.4) were unfolded using the MIEKE code and the smoothed response matrix (figure 5.1). Figure 5.6 shows the measured pulse height spectra H_1, H_2, H_3 and H_4 (histograms) and the refolded fits from the MIEKE analyses (solid lines). The agreement between the measured spectra and refolded fits appears to be good. Table 5.5 shows the chi-squared per degrees of freedom values for each MIEKE analysis which suggest that the pulse height spectra derived from the MIEKE analyses are compatible with the measured spectra [Ma94].

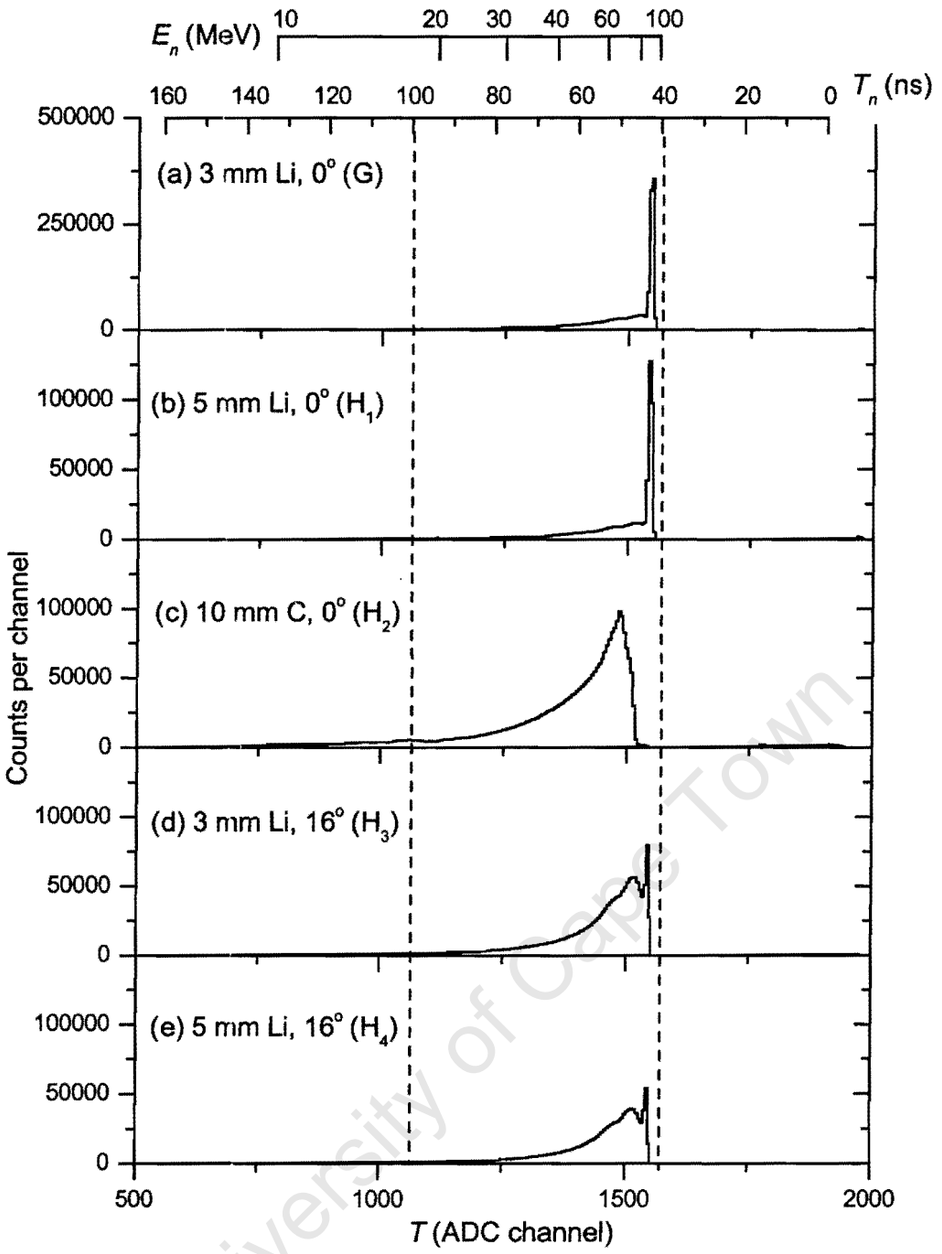

Figure 5.4. Neutron time-of-flight spectra measured for the runs listed in Table 2.4. The dashed lines indicate the time-of-flight window used to select the same energy range covered by the response matrix (see figure 5.1) which was based on spectrum (a).

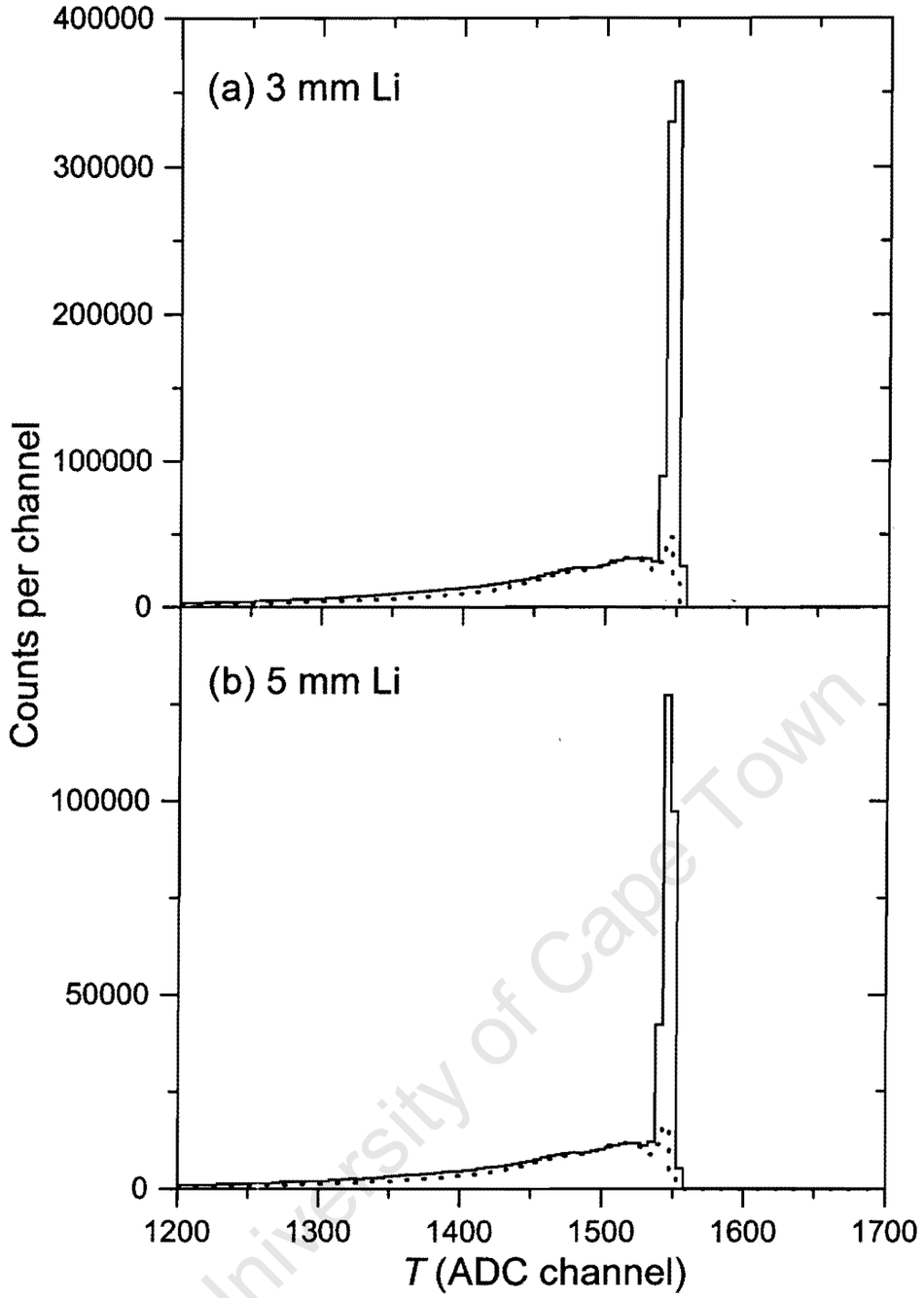

Figure 5.5. Neutron time-of-flight spectra measured for the (a) 3 mm and (b) 5 mm lithium targets at 0° (solid histograms) and 16° (dashed histograms), where the 16° measurements have been normalized to the 0° measurements at T-channel 1520.

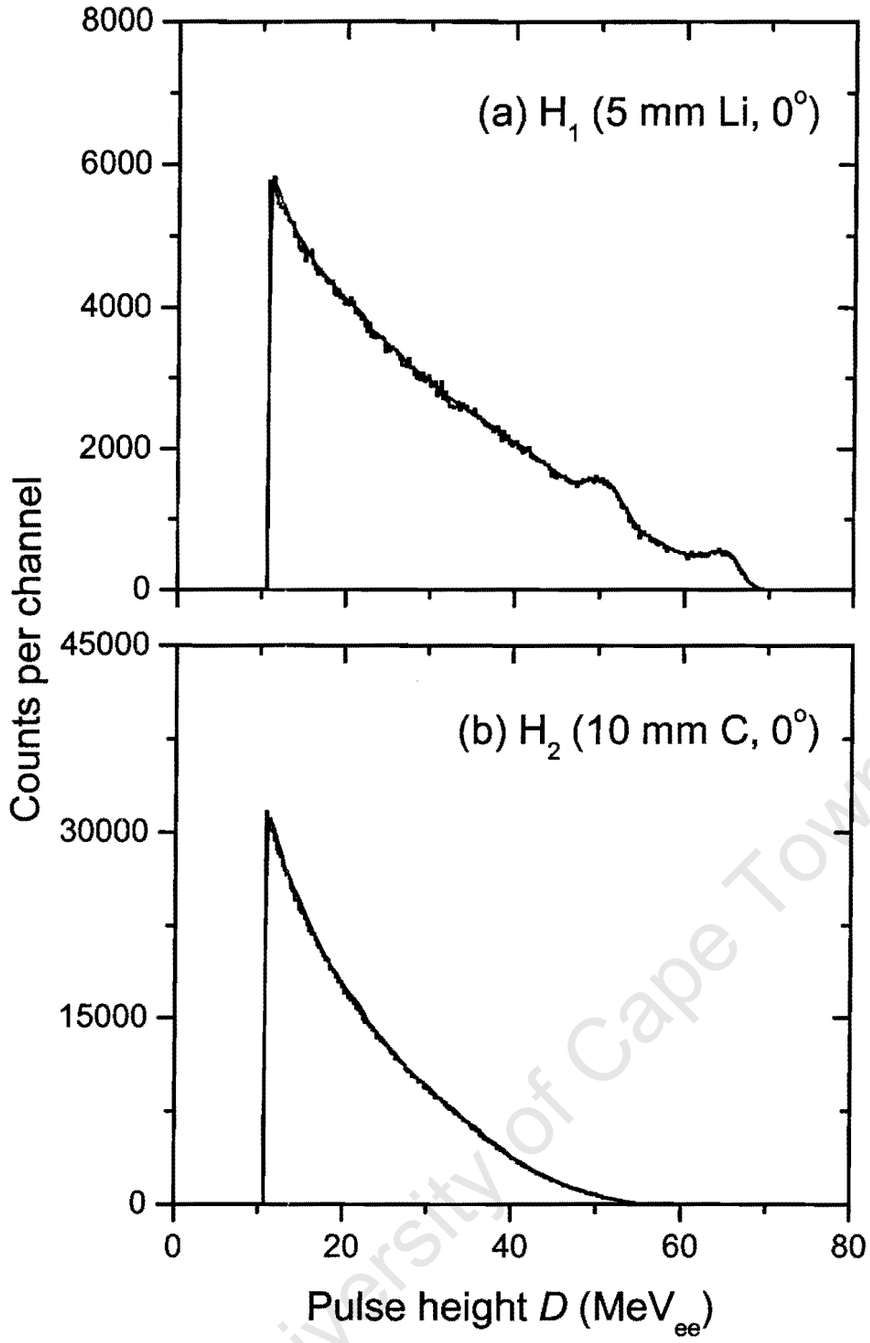

Figure 5.6. (This page and the next) Measured pulse height spectra (a) H_1, (b) H_2, (c) H_3 and (d) H_4 (see Table 5.4) measured using the stacked scintillator spectrometer (histograms) and the refolded fits (solid lines) resulting from the MIEKE analyses.

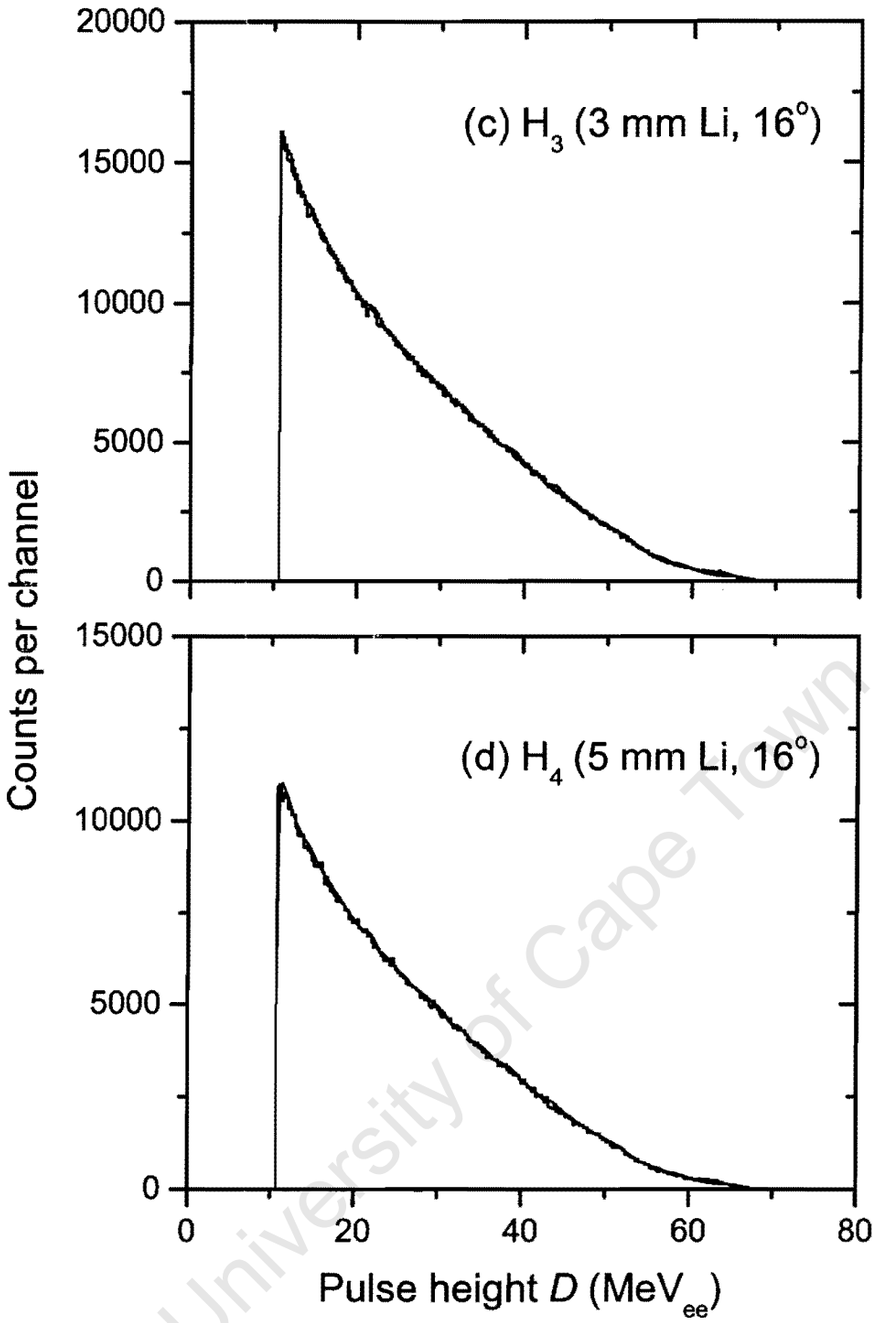

Figure 5.6. (continued).

Table 5.5: The chi-squared per degrees of freedom values from the MIEKE unfolding analyses for the pulse height spectra $H_1 - H_4$.

Pulse height spectrum	χ^2/dof
H_1	1.181
H_2	2.198
H_3	5.586
H_4	3.504

Figure 5.7(a) – (d) shows the neutron fluences (solid squares) with their uncertainties, obtained from the unfolding analyses, as a function of energy bin j for the pulse height spectra H_1, H_2, H_3 and H_4. The histograms in figure 5.7 show the measured time-of-flight spectra (see figure 5.4) binned using the same T-cuts used to select the energy bins j. These data are subject to the same pulse shape discrimination and threshold cuts used to produce and adjust each measured response function forming part of the response matrix used. Although some fluctuations are evident for the fluence measurements obtained from the unfolding analyses, the agreement between the expected and measured values is very good. It should be noted that the uncertainties shown in figure 5.7 result from the MIEKE unfolding only, and do not include the uncertainties associated with the fluence calculation for each response function in the response matrix (Table 4.5). It should be noted that the lack of deadtime monitoring in the experiments does not affect the shape of the energy spectra, although the fluence cannot be regarded as being on an absolute scale.

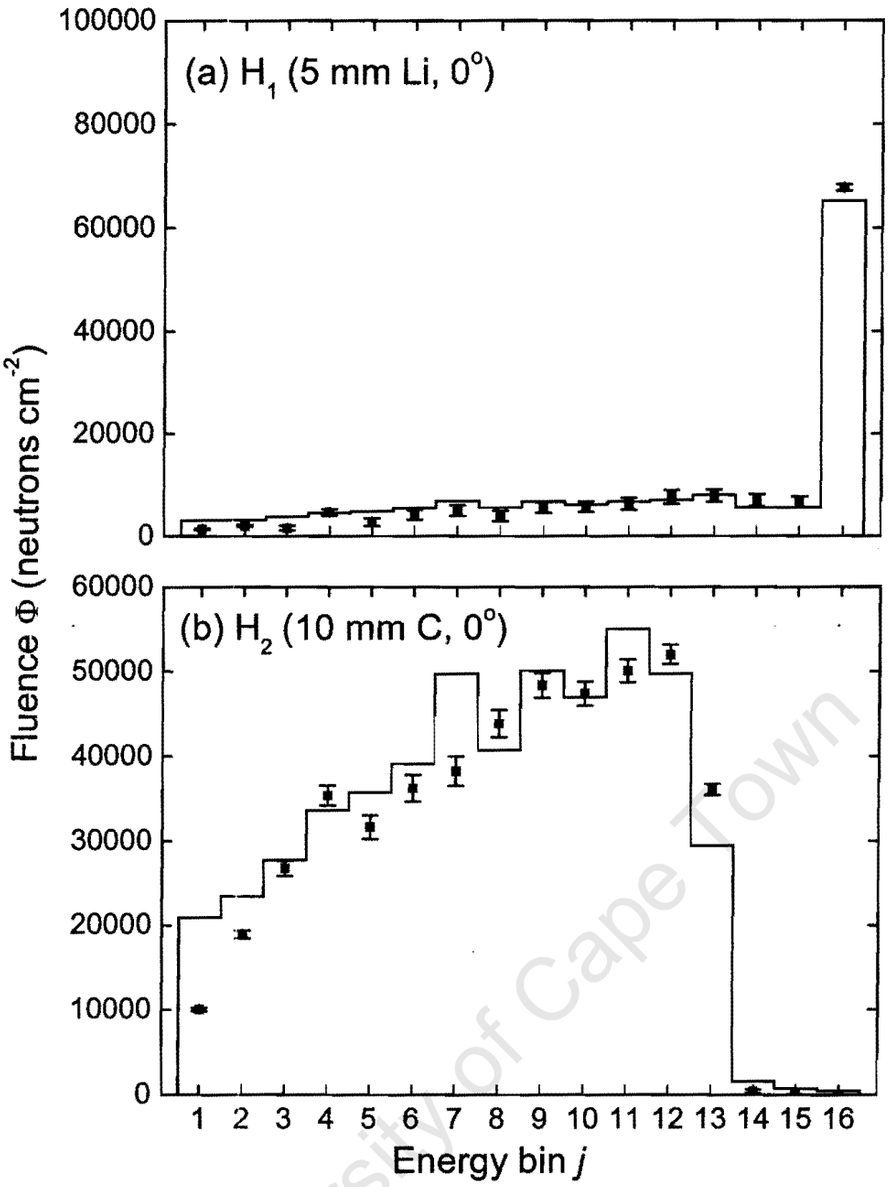

Figure 5.7. (This page and the next) Neutron fluence Φ calculated by MIEKE analyses (solid squares) for the pulse height spectra (a) H_1, (b) H_2, (c) H_3 and (d) H_4. The histograms show the fluences expected from the measured time-of-flight spectra, rebinned according to the same neutron time-of-flight cuts used to select the energy bins j for the response matrix.

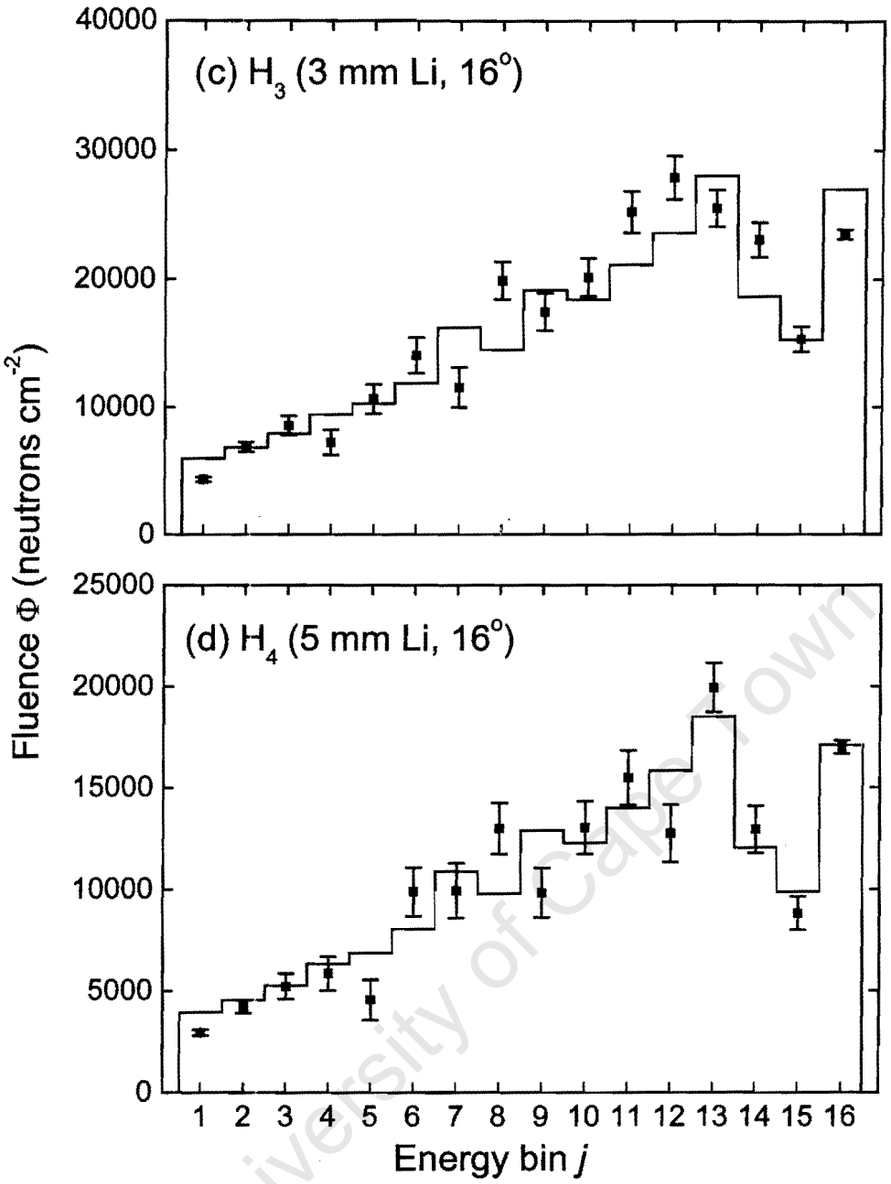

Figure 5.7. (continued).

6

Conclusion

6.1 Summary

A stacked scintillator neutron spectrometer, which has been developed in the Physics Department at the University of Cape Town, has been described which allows measurements of response functions in high energy-neutron beams. The stacked spectrometer used in the present work includes two modules of NE213 liquid scintillator and enables proton recoils from n–p scattering in the upstream scintillator to deposit their full energy in the spectrometer. The spectrum of the summed pulse heights from all detector segments results in a response function which is minimally affected by charged particle escape. The detection efficiency of the system, and hence the fluence of quasi-monoenergetic neutron beams, can be determined by relating the upper limit of the measured response functions (which can be attributed exclusively to proton recoils from n–p scattering) to the well-known differential cross sections for n–p elastic scattering.

The present work has illustrated the use of the stacked spectrometer system for measuring neutron fluence between neutron energies of 20 to 100 MeV. Data measured using

continuous neutron spectra obtained from 99.21 MeV proton bombardment of lithium and graphite targets were analysed. Using data from one such reaction (^{7}Li(p,n)^{7}Be), a series of discrete neutron energies were selected by means of time-of-flight windows, in order to produce quasi-monoenergetic pulse height spectra over the energy range 20 to 100 MeV. This facilitated the construction of a pulse-height response matrix for this neutron energy range. Measurements of spectral neutron fluence could then be obtained for a variety of beams from the application of unfolding procedures, thereby illustrating the use of the spectrometer in situations where pulsed neutron beams are not available. As it can be observed from figure 5.3, the agreement between the measured pulse height spectra and the "best fits" obtained from using the MIEKE code appears to be very good, even at the lower pulse heights. The neutron spectral fluence calculated by the MIEKE analyses also appear to be in good agreement with the expected values (figure 5.7).

6.2 Future work

A practical advantage associated with the modular design of the stacked spectrometer is that it is flexible insofar that the number of modules used can be tailored to match the energy range of the incident neutrons. Furthermore, the uniform design simplifies the task of matching pulse height and pulse shape discrimination responses of the different modules, as required for operation of the spectrometer. Further measurements have been made, although not fully analysed, employing the same technique as used at 97.1 MeV, to determine response functions of the stacked scintillator spectrometer for neutrons of energy 118 and 148 MeV. The thickness of the spectrometer was increased for these measurements, by adding a third scintillator module, identical to detectors A and B, between detectors B and V (see figure 1.9).

The unfolding procedure for this present work was based on response functions produced using energy bins of width 5 MeV. For better energy resolution in the spectral fluence measurements, a greater number of time cuts could be used, where the time-of-flight resolution of the system allows. Longer experimental runs would be needed in this case in order to collect sufficient data for statistical accuracy in the measured response functions. Furthermore, the present results strongly reinforce the need for stable beams during the collection of data collection required for response matrices, with very little, or no, pulse

selector breakthrough. This can seriously affect particular pulse height spectra in the measured response matrix which will in turn affect the shape of the energy spectra resulting from unfolding analyses.

There are a number of Monte Carlo codes (e.g. SCINFUL [Di88], MCNPX [Wa02] and CECIL [Ce79]) which can be used to simulate response functions of NE213. Although the inclusion of simulations might enhance the present work, there are difficulties in using such codes due to the lack of sufficient n–^{12}C cross section data at the higher energies, as has been discussed previously. However, a measurement of the fluence is possible if the simulated and measured spectra are matched in the upper pulse height region only, as was illustrated in figure 1.7. It is also possible to adjust the cross sections used in the code until a satisfactory fit is obtained over the entire pulse height range. If satisfactory agreement between calculation and measurement is obtained for a wide range of neutron energies, then the code might be useful to produce a response matrix with good energy resolution. This approach is illustrated in figure 6.1 [Na02] which shows a measured response function of NE213 scintillator, with and without escaping protons, for neutrons of energy 74 to 78 MeV. Also shown in the figure are calculations made using a modified CECIL code which match the measurements quite well over the whole spectrum.

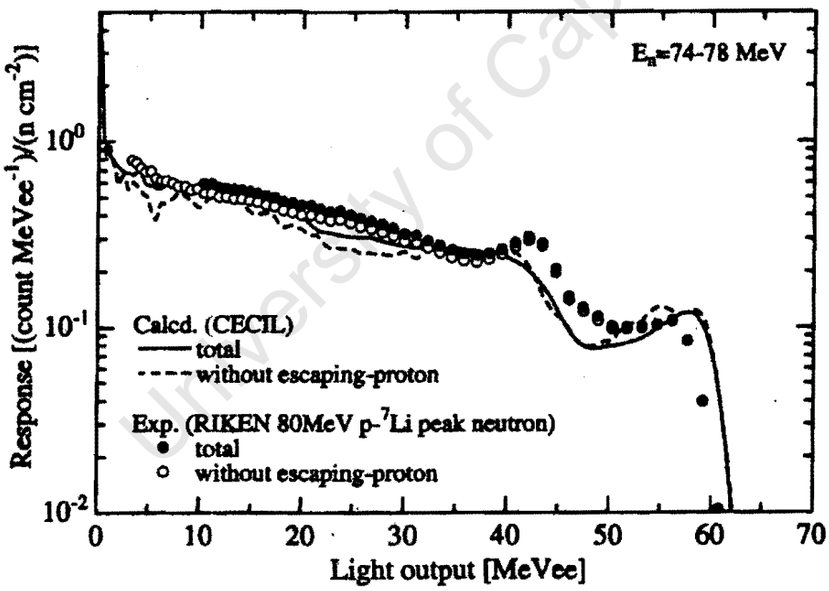

Figure 6.1. Response function measured (dots) and calculated (lines) using a modified CECIL code using a 12.7 × 12.7 (diam) cylindrical NE213 detector for incident neutrons of energy 74-78 MeV [Na02].

In summary, it may be concluded that the stacked liquid scintillator system employing two scintillator modules is a useful neutron spectrometer for neutron energies up to 100 MeV. The unfolding analyses presented in this work has advanced the development of the spectrometer by demonstrating measurement of spectral fluence for a variety of neutron beams. It would be useful to compare the measurements made for the present work with measurements made using other detectors during the same run series, particularly those produced by the overseas collaborators associated with this project.

References

Ad78 J.M. Adams and G. White, *Nucl. Instr. and Meth.*, **156** (1978) 459.

An79 M. Anghinolfi, G. Ricco, P. Corvisiero and F. Masulli, *Nucl. Instr. and Meth.* **165** (1979) 217.

Ba61 A.M. Baldin, V.I. Gol'danskii and I.L. Rozenthal, in *Kinematics of Nuclear Reactions*, (Pergamon Press, London, 1961).

Be69 P.R. Bevington, in *Data reduction and error analysis for the physical sciences* (McGraw-Hill, New York, 1969).

BIC http://www.bcrn.com

Bi64 J.B. Birks, in *Theory and practice of scintillation counting*, (Pergamon Press, 1964).

Br79 F.D. Brooks, *Nucl. Instr. and Meth.* **162** (1979) 477.

Br91 H.J. Brede, G. Dietze, H. Klein and H. Schölermann, *Nucl. Sci. and Eng.*, **107** (1992) 22 .

Br02 F.D. Brooks and H. Klein, *Nucl. Instr. and Meth.*, **A476** (2002) 1.

Bu65 W.R. Burrus and J.D. Drischler, *Oak Ridge National Laboratory*, *Report* **ORNL-4154** (1965).

Bu91 A. Buffler, *MSc. Thesis* (unpublished), University of Cape Town, 1991.

Bu02 A. Buffler, F.D. Brooks, M.S.Allie, P.J. Binns, V. Dangendorf, K.M. Langen, R. Nolte and H. Schuhmacher, *Nucl. Instr. and Meth.*, **A476** (2002) 181.

Ce79 R.A. Cecil, B.D. Anderson and R. Madey, *Nucl. Instr. and Meth.*, **161** (1979) 439.

Cr87 W.G. Cross and H. Ing, *"Neutron spectroscopy"*, in *The dosimetry of ionising radiation*, (K.R. Kase, B.E. Bjarngard and F. H. Attix, eds.), Academic Press, Inc., New York (1987).

Di82 G. Dietze and H. Klein, NRESP4 and NEFF4: *Monte Carlo Codes for the Calculation of Neutron Response Functions and Detector Efficiencies for NE213 Scintillation Detectors*, *Report* **PTB-ND-22**, PTB Brauschweig, 1982.

Di84 M.S. Dias, R.G. Johnson and O.A. Wasson, *Nucl. Instr. and Meth.*, **224** (1984) 532.

Di88 J.K. Dickens, *Oak Ridge National Laboratory*, *Report* **ORNL- 6462** (1988).

Di92 M.S. Dias, *Nucl. Instr. and Meth.*, **A321** (1992) 317.

ET http://www.eljentechnology.com

Fi98 R. Fischer, M. Mayer, W. von der Linden and V. Dose, *Nucl. Instr. and Meth.*, **B136-138** (1998) 1140.

Fr99 D.W. Freeman, D.R. Edwards and A.E. Bolon, *Nucl. Instr. and Meth.*, **A425** (1999) 549.

GNU Data reduction software available in the Physics Department, University of Cape Town.

GUM International Organization for Standardization, *Guide to the expression of uncertainty in measurement (GUM)*, Geneva, Switzerland (1995).

ITH iThemba Laboratory for Accelerator Based Sciences, P.O. Box 72, Faure, Cape Town, South Africa, 7131 (http://www.tlabs.ac.za).

IUCF http://www.iucf.indiana.edu/~yoder/datacq/vmedoc.html

Ja57 E.T. Jaynes, *Phys. Rev.*, **106** (1957) 620.

Ja90 E.T. Jaynes, in *Maximum Entropy and Bayesian Methods*, Ed: P.F. Fougére, (Kluwer Academic Publishers, Dordrecht, 1990).

Je67 H. Jeffreys, in *Theory of Probability* (Clarendon Press, Oxford, 1967).

Ji84 P. Jipsen and J. Maritz, Program ELOSS 2.0, based on data from H. H. Andersen and J. F. Ziegler, in *The Stopping and Ranges of Ions in Matter , Volumes 3, 4 and 5*, (Pergamon Press, New York, 1977).

Ke53 D.A. Kellog, *Phys. Rev.*, **90** (1953) 2 224.

Kl79 H. Klein and H. Schölermann, *IEEE Transactions on Nucl. Sc.*, **NS-26** No. 1 1979.

Kl02 H. Klein and S. Neumann, *Nucl. Instr. and Meth.*, **A476** (2002) 132.

Kn89 G.F. Knoll, in *Radiation Detection and Measurement*, 2nd edition, (Wiley, New York, 1989).

Ko93 R. Koohi-Fayegh, S. Green, N.M.J. Crout, G.C. Taylor and M.C. Scott, *Nucl. Instr. and Meth.*, **A329** (1993) 269.

Le89 M.L. Lee, in *Bayesian statistics: an introduction*, (Oxford University Press, New York, 1989).

Lo76 J.A. Lockwood, C. Chen, L.A. Friling, D. Swartz, R.N. St. Onge, A. Galonsky and R.R. Doering, *Nucl. Instr. and Meth.*, **138** (1976) 353.

Ly75 F.J. Lynch, IEEE *Transactions on Nucl. Sc.*, **NS-22** (1975) 58.

Ma85 M. Matzke and K. Weise, *Nucl. Instr. and Meth.*, **A234** (1985) 324.

Ma88 M. Matzke, *Rad. Prot. Dosim.*, **23** (1988) 297.

Ma94 M. Matzke, "*Unfolding of Pulse Height Spectra: The HEPRO Program System*", *Report* **PTB-N-19**, (Physikalisch-Technische Bundesanstalt, Braunschweig, 1994).

Ma97 M. Matzke, *Proc. Int. Soc. Opt. Eng.*, **2867** (1997) 598.

Ma02 M. Matzke, *Nucl. Instr. and Meth.*, **A476** (2002) 230.

Mc67 W.N. McElroy, S. Berg, T. Crockett and R.G. Hawkins, *A computer-automated iterative method for neutron flux spectra determination by foil activation, SAND-II*, *Report* **AFWL – TR – 67 – 41**, U.S. Air Force Weapons Laboratory, 1967.

Mc88 V. McLane, C.L. Dunford and P.F. Rose (eds.), *Neutron Cross Sections, Volume 2*, (Academic Press, New York, 1988).

Mi67 A. Michalowitz, in *Kinematics of Nuclear Reactions*, (Iliffe Books, London, 1967).

Mo94 M. Moszynski, G.J. Costa, G. Guillaume, B. Heusch, A. Huck, and S. Mouatassim, *Nucl. Instr. and Meth.* **A350** (1994) 226.

Na01 N. Nakao, T. Kurosawa, T. Nakamura and Y. Uwamino, *Nucl. Instr. and Meth.*, **A463** (2001) 275.

Na02 N. Nakao, T. Kurosawa, T. Nakamura and Y. Uwamino, *Nucl. Instr. and Meth.*, **A476** (2002) 176.

NE Scintillator specification sheet, Nuclear Enterprises Technology Limited, previously of Sighthill, Edinburgh, Scotland.

No97 T. Novotny, "*Photon spectrometry in mixed neutron-proton fields using NE213 liquid scintillator detectors*", *Report* **PTB-N-28**, (Physikalisch-Technische Bundesanstalt, Braunschweig, 1997).

No02 R. Nolte, M.S. Allie, P.J. Binns, F. Brooks, A. Buffler, V. Dangendorf, J.P. Meulders, F. Roos, H. Schuhmacher and B. Wiegel, *Nucl. Instr. and Meth.*, **A476** (2002) 369.

Ol92 M.J. Oliver, *MSc. Thesis* (unpublished), University of Cape Town, 1992.

Pe77 F.G. Perey, *Report* **ORNL/TM-6062 ENDF-254k**, (Oak Ridge National Laboratory, 1977).

Pe00 A.J. Peurrung, *Nucl. Instr. and Meth.*, **A443** (2000) 400.

Po72 W.P. Poenitz, "*The black neutron detector*", *Report* **ANL-7915**, (Argonne National Laboratory, 1972).

Pr96 W.H. Press, B.P. Flannery, S.A. Teukolsky and W.T. Vetterling, in *Numerical recipes: the art of scientific computing*, (Cambridge University Press, Cambridge, 1996).

Pr98 V.M. Prozesky, J. Padayachee, R. Fischer, W. von der Linden, V. Dose and R.A. Weller, *Nucl. Instr. and Meth.*, **B136-138** (1998) 1146.

Pu93 J. Pulpán and M. Králík, *Nucl. Instr. and Meth.*, **A325** (1993) 314.

RCA RCA Specification Sheet **6-72**, available from RCA Electronics, Harrison, New Jersey, United States, 07029.

Re99 M. Reginatto and P. Goldhagen, *Health Physics*, **77** (1999) 579.

Re02 M. Reginatto, P. Goldhagen and S. Neumann, *Nucl. Instr. and Meth.*, **A476** (2002) 242.

Ro80 J.T. Routti and J.V. Sandberg, *Comput. Phys. Comm.*, **21** (1980) 119.

Ro85. J.T. Routti and J.V. Sandberg, *Rad. Prot. Dosim.*, **10** (1985) 103.

Ro91 P.F. Rose, "*ENDF-201: ENDF/B-VI Summary Documentation*", *Report* **BNL-NCS-17541**, (Brookhaven National Laboratory, 1991).

Sa64 A. Savitsky and M.J.E. Golay, *Analytical Chemistry*, **36** 8 (1964) 1627.

Sc97 D. Schmidt and Z. Chenwei, *Report* **PTB-6.42-97-1**, (Physikalisch-Technische Bundesanstalt, Braunschweig, 1997).

Sc98 H. Schuhmacher, H.J. Brede, V. Dangendorf, M. Kuhfus, J.P. Meulders, W.D. Newhauser, R. Nolte and U. Shrewe, *Nucl. Instr. and Meth.*, **A421** (1998) 284.

Sd98 D. Schmidt and H. Klein, *Report* **PTB-N-35**, (Physikalisch-Technische Bundesanstalt, Braunschweig, 1998).

Si01 J.M. Sisterson, D.T.L. Jones, P.J. Binns, K. Langen, I. Schroeder, Z. Buthelezi, E. Latti, F.D. Brooks, A. Buffler, M.S. Allie, M.S. Herbert, M.R. Nchodu, S. Makupula, J. Ullmann and R.C. Reedy, *Lunar and Planetary Science XXXII*, Abstract #1302, Lunar and Planetary Institute, Houston (CD-ROM), 2001.

Si02 J.M. Sisterson, D.T.L. Jones, F.D. Brooks, A. Buffler, M.S. Allie, M.S. Herbert, M.R. Nchodu, S. Makupula, J. Ullmann and R.C. Reedy, *Lunar and Planetary Science XXXIII*, Abstract #1541, Lunar and Planetary Institute, Houston (CD-ROM), 2002.

Sk89 J. Skilling, in *Maximum Entropy and Bayesian Methods*, Ed: J. Skilling (Kluwer Academic Publishers, Dordrecht, 1989).

Sk91 J. Skilling, in *Maximum Entropy in Action*, Eds: B. Buck and V. Macaulay, (Clarenden Press, Oxford, 1991).

Sm87 F.D. Smit and F.D. Brooks, *Nuclear Physics*, **A465** (1987) 429.

Ta94 B.N. Taylor and C.E. Kuyatt, *Guidelines for Evaluating and Expressing the Uncertainty of NIST Measurement Results*, National Institute of Standards and Technology (NIST), Technical Note 1297 (1994) (http://physics.nist.gov/Pubs/guidelines/contents.html).

Ta01 M. Takada, S. Taniguchi, N. Nakao, Y. Uwamino, T. Shibata and K. Fujitaka, *Nucl. Instr. and Meth.*, **A465** (2001) 498.

Ti88 M. Tichy, *Nucl. Instr. and Meth.*, **A267** (1988) 502.

Ti93 M. Tichy, *Report* **PTB-7.2-93-1**, (Physikalisch-Technische Bundesanstalt, Braunschweig, 1993).

Uw82 Y. Uwamino, K. Kazuo, M. Fujii and T. Nakamura, *Nucl. Instr. and Meth.*, **204** (1982) 179.

Ve68 V.V. Verbinski, W.R. Burrus, T.A. Love, W. Zobe, N.W. Hill and R. Textor, *Nucl. Instr. and Meth.*, **65** (1968) 8.

Vo68 R. Voltz, H. du Pont and G. Laustralt, *J. Physique*, **29** (1968) 297.

Vo95 W. von der Linden, *Applied Physics*, **A60** (1995) 155.

Wa74 J.W. Watson and R.G. Graves, *Nucl. Instr. and Meth.*, **117** (1974) 541.

Wa02 L. Waters, *MCNPX User's Manual, version* **2.4.0**, LA-CP-02-408, (2002) Los Alamos National Laboratory, (http://mcnpx.lanl.gov).

We87 K. Weise, *IEEE Transactions on Instr. Meas.*, **IM-36** (1987) 642.

We89 K. Weise and M. Matzke, *Nucl. Instr. and Meth.*, **A280** (1989) 103.

We95 K. Weise, *Report* **PTB-N-24**, (Physikalisch-Technische Bundesanstalt, Braunschweig, 1995).

Wo68 W.W. Wood, in *Physics of Simple Liquids*, North Holland Pub. Comp., Amsterdam, New York, 1968, 115.